Isogeometric Modeling, Simulation and Optimization of Rotating Electric Machines

Isogeometrische Modellierung, Simulation und Optimierung Rotierender Elektrischer Maschinen

Zur Erlangung des akademischen Grades Doktor-Ingenieur (Dr.-Ing.)
genehmigte Dissertation von Anna Melina Merkel aus Frankfurt a.M., Deutschland
Elektrotechnik und Informationstechnik, Technische Universität Darmstadt, Darmstadt
Tag der Einreichung: 1. Juli 2023, Tag der Prüfung: 2. November 2023

1. Gutachten: Prof. Dr. Sebastian Schöps
2. Gutachten: Prof. Dr. Rafael Vázquez Hernández
3. Gutachten: Prof. Dr. Manfred Kaltenbacher
Darmstadt – D 17

TECHNISCHE UNIVERSITÄT DARMSTADT

CEM

Fachbereich 18
Computational Electromagnetics Group

Isogeometric Modeling, Simulation and Optimization of Rotating Electric Machines
Isogeometrische Modellierung, Simulation und Optimierung Rotierender Elektrischer Maschinen

genehmigte Dissertation von Anna Melina Merkel aus Frankfurt a.M., Deutschland
Elektrotechnik und Informationstechnik, Technische Universität Darmstadt, Darmstadt

1. Gutachten: Prof. Dr. Sebastian Schöps
2. Gutachten: Prof. Dr. Rafael Vázquez Hernández
3. Gutachten: Prof. Dr. Manfred Kaltenbacher

Tag der Einreichung: 1. Juli 2023
Tag der Prüfung: 2. November 2023

Darmstadt – D 17

Erklärungen laut Promotionsordnung

§8 Abs. 1 lit. c PromO

Ich versichere hiermit, dass die elektronische Version meiner Dissertation mit der schriftlichen Version übereinstimmt.

§8 Abs. 1 lit. d PromO

Ich versichere hiermit, dass zu einem vorherigen Zeitpunkt noch keine Promotion versucht wurde. In diesem Fall sind nähere Angaben über Zeitpunkt, Hochschule, Dissertationsthema und Ergebnis dieses Versuchs mitzuteilen.

§9 Abs. 1 PromO

Ich versichere hiermit, dass die vorliegende Dissertation selbstständig und nur unter Verwendung der angegebenen Quellen verfasst wurde.

§9 Abs. 2 PromO

Die Arbeit hat bisher noch nicht zu Prüfungszwecken gedient.

Darmstadt, 1. Juli 2023

Melina Merkel

Zusammenfassung

Im Zuge der angestrebten Energiewende und des damit einhergehenden Anstiegs der Elektromobilität erweist sich die effiziente und robuste Auslegung und Optimierung elektrischer Maschinen als immer bedeutsamer. Simulationen sind ein wichtiges Werkzeug, um verbesserte Designs zu erhalten. Diese Arbeit konzentriert sich auf die Entwicklung geeigneter Simulations- und Optimierungsmethoden für elektrische Maschinen, basierend auf Isogeometischer Analyse (IGA). IGA ermöglicht eine direkte Verwendung der Modelle aus dem Computer Aided Design (CAD), erlaubt eine exakte Geometriedarstellung und einfache Formoptimierung durch unkomplizierte Geometriemodifikation mittels Verschiebung der Kontrollpunkte. Außerdem bietet IGA eine höhere Genauigkeit pro Freiheitsgrad im Vergleich zur klassischen Finite Elemente Methode (FEM). Darüber hinaus ist bei der Verwendung von IGA für Multiphysik-Simulationen eine Neuvernetzung oder ein Austausch des Rechengitters zwischen mehreren physikalischen Systemen nicht erforderlich. Bei der Anwendung von IGA ergeben sich jedoch mehrere Herausforderungen, wie zum Beispiel die Integration der Rotation und die damit zusammenhängende Nichtkonformität der Diskretisierung. Diese Arbeit befasst sich mit den genannten Schwierigkeiten und schlägt Ansätze zur Erleichterung der Simulation vor, darunter die Berücksichtigung der Rotation der Simulation, die Gewährleistung der Stabilität und die Regularisierung der Formulierung, und eine Freiform-Formoptimierung der Maschine.

Bei Anwendung von IGA auf Maschinenprobleme werden Multi-Patch Spline-Räume mit nicht-konformen Diskretisierungen zwischen Rotor und Stator genutzt, insbesondere im Falle der Rotation. Zur Lösung dieses Problems werden verschiedene Kopplungsmethoden für nicht-konforme Diskretisierungen verwendet. Im zweidimensionalen Fall stellt die harmonische Stator-Rotor-Kopplung einen vielversprechenden Ansatz für die Verbindung nicht-konformer Teilbereiche dar. Diese Methode führt jedoch zu einem Sattelpunktsystem, dessen Stabilität von der Wahl des Lagrange-Multiplikator-Raums abhängt. In dieser Arbeit wird ein allgemeines Kriterium für die Wahl des diskreten Multiplikator-Raums hergeleitet, das die Inf-Sup-Stabilität des Problems gewährleistet. Dieses Kriterium gilt für eine Vielzahl von Diskretisierungsansätzen, einschließlich FEM und IGA. Durch Anwendung eines Schur-Komplements wird das System auf ein niedrigdimensionales Schnittstellenproblem reduziert, wodurch die Rechenkosten während der Simulation der Rotation erheblich gesenkt werden. Für dreidimensionale Probleme werden die Nitsche-Kopplungsmethode und die Mortarmethode zur Realisierung der Rotation in Verbindung mit IGA untersucht. Die bekannte Theorie zur Wahl des Lagrange-Multiplikator-Raums in isogeometrischem Mortaring wird dahingehend erweitert, dass das Verfahren auch für Multi-Patch Geometrien anwendbar ist. Die Konvergenzanalyse zeigt, dass beide Methoden mit dem Grad der IGA-Basisfunktionen konvergieren.

Die Formulierung magneto(quasi)statischer Probleme unter Verwendung des Vektorpotential-Ansatzes besitzt keine eindeutige Lösung. Eine Methode zur Eliminierung des diskreten Nullraums des System stellt die Baum-Kobaum-Zerlegung dar. In dieser Arbeit wird die Anwendung dieser Methode auf IGA übertragen, wobei das Kontrollnetz die Basis der Baum-Kobaum-Zerlegung darstellt. Die Methode funktioniert für nicht-zusammenziehbare Gebiete und lässt sich unabhängig vom Grad der B-Spline-Basisfunktionen

anwenden. Um die Eichung gekoppelter Gebiete zu ermöglichen, wird eine modifizierte Baum-Kobaum-Zerlegung vorgeschlagen und auf das Modell einer dreidimensionalen Permanentmagnet-Synchronmaschine (PMSM) angewendet.

Das Drehmoment ist ein wichtiger Faktor bei der Auslegung elektrischer Maschinen. Die klassische FEM neigt zu Ungenauigkeiten bei der Berechnung des Drehmoments. In dieser Arbeit werden effiziente Ansätze zur Drehmomentberechnung vorgeschlagen, die die Lagrange-Multiplikatoren der harmonischen Kopplung und der Mortar-Methode ausnutzen. Für die harmonische Kopplung werden – basierend auf dem Energiegleichgewicht – explizite Formeln zur Drehmomentberechnung hergeleitet. Die harmonische Eigenschaft der Lagrange-Multiplikatoren ermöglicht eine elegante Behandlung der Rotation, wodurch die Notwendigkeit zusätzlicher numerischer Integration entfällt. Die vorgeschlagenen Methoden werden mit der Arkkio-Methode verglichen, wobei sie sich als ähnlich genau und deutlich Rechenkosten-effizienter erweisen.

Abschließend wird eine auf Formableitungen basierende Optimierungsmethode vorgestellt. Die Form-Sensitivitätsanalyse wird verwendet, um die Formableitung der Zielfunktion der Optimierung zu bestimmen. Hierbei wird die Minimierung von Oberschwingungen (Total Harmonic Distortion, THD) der Elektromotorischen Kraft (Electromotive Force, EMF) als Zielfunktion gewählt. Diese vorgestellte Methode ermöglicht eine Freiform-Optimierung, die nicht durch die Wahl bestimmter Optimierungsparameter eingeschränkt ist. Diese Freiform-Optimierung wird erstmals auf ein isogeometrisches Modell einer rotierenden PMSM zur Reduktion der THD der EMF angewandt, wobei eine Reduktion von $75\,\%$ erreicht wird.

Die in dieser Arbeit vorgeschlagenen Methoden werden erfolgreich auf zwei- und dreidimensionale Modelle einer PMSM angewendet. Sie können im Entwurfsprozess elektrischer Maschinen eingesetzt werden und erleichtern den Arbeitsablauf durch direktes Arbeiten auf CAD-Geometrien – wodurch Gittergenerierung nicht erforderlich ist – und ebnen damit den Weg für multiphysikalische Simulationen. Obwohl der Fokus dieser Arbeit auf der Simulation elektrischer Maschinen liegt, sind die vorgeschlagenen Methoden auf verschiedene Anwendungsfelder wie zum Beispiel Wirbelstrombremsen oder magnetokalorische Kühlsysteme übertragbar und besonders vorteilhaft, wenn nicht-konforme oder bewegliche Teilgebiete berücksichtigt werden müssen.

Abstract

Given the ongoing transition to renewable energy and the concurrent rise in e-mobility, the efficient and robust design and optimization of electric machines has become increasingly important. Simulations are a crucial tool to obtain improved designs. This thesis focuses on the development of suitable simulation and optimization methodologies for electric machines, based on isogeometric analysis (IGA). IGA allows for a direct use of computer aided design (CAD) data, offering an exact geometry representation and easy shape optimization through straightforward geometry modification via shifting the control points. Furthermore, when compared to the conventional finite element method (FEM), IGA provides a higher accuracy per degree of freedom (DoF). Moreover, when employing IGA for multiphysics simulations, a remeshing or mesh exchange between multiple physics is not necessary. However, several challenges arise when using IGA, e.g., the incorporation of rotation and the resulting non-conformity of the discretization. This thesis addresses these difficulties, proposing approaches to facilitate the simulation, including the integration of rotation in the simulation, ensuring stability of the formulation, regularization of the formulation, and freeform shape optimization of the machine.

When applying IGA to machine problems, one encounters multi-patch spline spaces that have incompatible discretizations between rotor and stator, particularly in the case of rotation. We utilize a variety of methods to couple non-conforming discretizations to address these challenges. In the two-dimensional case, harmonic stator-rotor coupling offers a promising approach to interconnect these non-conforming subdomains. However, this method results in a saddle-point system, which is stable only with an appropriate choice of the Lagrange multiplier space. In this work, we derive a general criterion to ensure the inf-sup stability of this problem. The criterion applies to a variety of discretization approaches, including FEM and IGA. A Schur complement is used to reduce the system to a low-dimensional interface problem, significantly decreasing the computational cost during the simulation of rotation. For the three-dimensional problem, the Nitsche-type coupling method and the mortar method are examined in the context of IGA for the realization of rotation. The established theory for the choice of the Lagrange multiplier space for isogeometric mortaring is extended to be applicable for multi-patch domains. Convergence analysis shows that both methods converge with the degree of the IGA basis functions.

The simulation of three-dimensional magneto(quasi)static problems using the vector potential formulation poses the problem of a non-uniqueness of the solution. A method which can be employed to remove the discrete kernel from the system is the tree-cotree decomposition. The application of this gauging to IGA is proposed, where the tree-cotree decomposition is performed based on the control mesh. The method works for non-contractible domains and can be straightforwardly applied independently of the degree of the B-spline bases. To allow for the gauging of mortared domains, a modified tree-cotree decomposition is derived and applied to the model of a three-dimensional permanent magnet synchronous machine (PMSM).

One important quantity of interest in electric machines is the torque. The classical FEM, often suffers from inaccuracies in torque computation. This work proposes methods for efficient torque computations

based on the Lagrange multipliers of the harmonic coupling and the mortar method. In the harmonic coupling method, we derive explicit formulas for torque computation using energy considerations. The harmonic nature of the Lagrange multiplier allows for an elegant treatment of rotation, eliminating the need for additional numerical evaluations of integrals. These proposed methods are compared to the Arkkio method and are found to be similarly accurate and significantly more efficient in terms of computational cost.

Finally, an optimization method is introduced, based on shape calculus. Shape sensitivity analysis is used to determine the shape derivative of the objective functional, i.e., the total harmonic distortion (THD) of the electromotive force (EMF). This method allows for a freeform shape optimization which is not restricted by the choice of a set of optimization parameters. This freeform shape optimization is applied for the first time to an isogeometric model of a rotating PMSM, minimizing the THD of the EMF, where a reduction of $75\,\%$ is achieved.

The proposed methods are successfully applied to two- and three-dimensional models of a PMSM. They are ready to be employed in the design process of electric machines, facilitating the workflow by operating directly on CAD geometries, alleviating the need to generate a computational mesh, and therefore pave the way for multiphysical simulations. While this thesis focuses on the simulation of electric machines, the proposed methods can be applied to different applications, e.g., eddy current brakes or magnetocaloric cooling devices, and are particularly beneficial when considering non-conforming or moving subdomains.

Contents

List of figures

List of tables

1 Introduction and Motivation

One of the main contributors of energy consumption is the transportation sector. In 2022, around $28\,\%$ of the total energy consumption stems from the transportation sector [153, Table 2.1b]. In the energy transition, electrification of transportation will play a crucial role in the shift towards renewable energies. The rise of e-mobility, including electric bicycles, scooters, motorcycles and cars, but also public transportation, trucks, ferries and aircraft has already increased the demand for electric energy by about $33\,\%$ between 2010 and 2021. This demand is expected to grow by another $120\,\%$ until 2050 according to the Announced Pledges Scenario [90, Table 6.2]. As industrial electro-mechanical energy conversion makes up around $70\,\%$ of electric energy consumption, there is a huge potential to decrease the future energy demand by developing more energy-efficient electric machines [2]. Next to maximizing the energy efficiency, other important objectives in developing new machine designs include the reduction of the machine size, thus increasing the energy density, and the reduction of the machine cost. According to a projection by the U.S. Department of Energy in [152], there is a considerable potential for the improvement of electric machines between 2020 and 2025. Their motor targets include a cost reduction of $30\,\%$, lowering from $4.7\,\$/\mathrm{kW}$ to $3.3\,\$/\mathrm{kW}$, and a volume reduction of $89\,\%$, which would correspondingly increase the power density from $5.7\,\mathrm{kW/L}$ to $50\,\mathrm{kW/L}$. Permanent magnet machines possess a high energy density, but the use of rare earth materials in the permanent magnets, such as neodymium, faces challenges, including their limited availability and both environmental and ethical concerns [101]. This makes for example the reduction of the permanent magnet volume another interesting design goal.

In the design process of electric machines, as illustrated in Fig. 1.1, closed-form analytic considerations are mainly employed in the initial design stages, where fundamental decisions regarding the machine's type, topology, materials, and sizing are made. The machine configuration is chosen during this stage, such that the design requirements are adequately met. Optimizing the machine, considering various key performance indicators (KPIs), and obtaining improved and robust designs requires the use of numerical simulation tools. The workflow usually includes designing the machine using computer aided design (CAD) software, discretizing the model, and then employing numerical simulation and optimization. Often, simulation and optimization are performed using two-dimensional models, as these are computationally efficient and provide an adequate approximation for many types of machines, including permanent magnet synchronous machines (PMSMs). The conventional approach uses the finite element method (FEM) with polynomial basis functions of low order p, i.e., $p \leq 3$. Geometry and mesh handling difficulties, along with the need for error-prone interpolation, e.g., when considering mechanical deformation, often complicate more comprehensive multiphysical simulations. According to Sandia National Laboratories, approximately $75\,\%$ of the simulation time in research facilities and industry is spent on modeling, parametrization, mesh generation and pre- and post-processing [20]. Therefore, important KPIs like NVH (noise, vibration, harshness, see, e.g. [77, 142]) are often evaluated later in the design process. In this work, we propose innovative approaches to address these geometry-related issues. We use a simulation platform based on isogeometric analysis (IGA) [23, 35, 58, 88] in both two and three dimensions. IGA, which uses B-splines and non-uniform rational B-splines (NURBS) as basis functions for geometry and

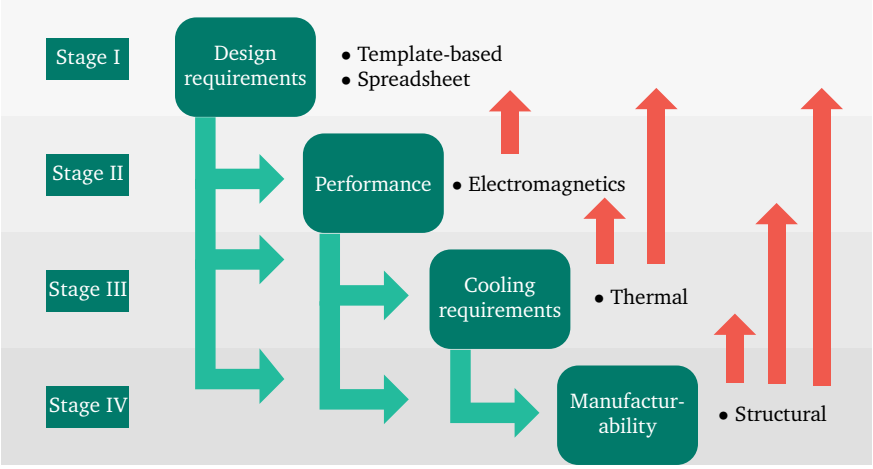

Figure 1.1: Multiphysical design workflow of electric machines. Based on [137, Figure 1].

solution, instead of polynomials, allows for direct and approximation-free use of CAD geometry data, thereby simplifying the implementation of freeform optimization. The discretization of an electric machine model is visualized in Fig. 1.2b, where Fig. 1.2a shows a traditional triangular mesh approximating the geometry, whereas Fig. 1.2b shows the exact CAD geometry employed in IGA and the control points defining it. Furthermore, IGA offers the potential for direct 3D printing [160]. The spline-based representation of geometry and solution allows for interpolation-free coupling of geometries but also coupling different physics, e.g., the interaction between electromagnetic, thermal and mechanical phenomena and NVH calculations. Moreover, for smooth solutions, IGA provides a higher accuracy per degree of freedom. This is particularly relevant in the air gap of an electric machine, where the smoothness of the solution can be exploited. IGA for machine simulation has recently been investigated for axial flux permanent magnet machines in [68]. For considering rotation, the stator and rotor are typically coupled via sliding surface or moving band methods [48]. We will employ and investigate coupling methods, including the harmonic coupling [24] and the mortar method [130] for IGA in terms of stability and correctness.

The nominal geometry of the machine, i.e., not considering operation variations or uncertainties introduced by the manufacturing process, is often optimized in two dimensions via swarm algorithms using empirical parameters, constant temperature and constant angular speed. In conventional geometry optimization, typically only a set of user-defined parameters are allowed as degrees of freedom. In a true freeform optimization however, also topology changes are allowed in the design, e.g., the magnet configuration or the type of the machine can be optimized algorithmically. The application of IGA enables geometric freeform optimization of the machine with a fixed topology. This method allows us to transform the geometry smoothly and effortlessly by moving the control points of the splines, alleviating the necessity for remeshing when modifying the geometry [114]. While the same effect can be achieved using the classical FEM, it requires significantly more effort. This makes IGA an excellent choice for shape optimization [72, 114]. Significant improvements in technical designs, such as those in permanent magnet synchronous machines, have been made possible by numerical optimization based on magnetic equivalent circuits or finite element (FE) models. Over the past three decades, a lot of research has been conducted on optimization methods based on FE (see, e.g., [53, 60] and the references therein). Initially, mainly gradient-based optimization methods were employed (see, e.g., [139, 151, 159]). However, in the last two decades there has been a shift towards the popularity of stochastic and population-based optimization algorithms [80,

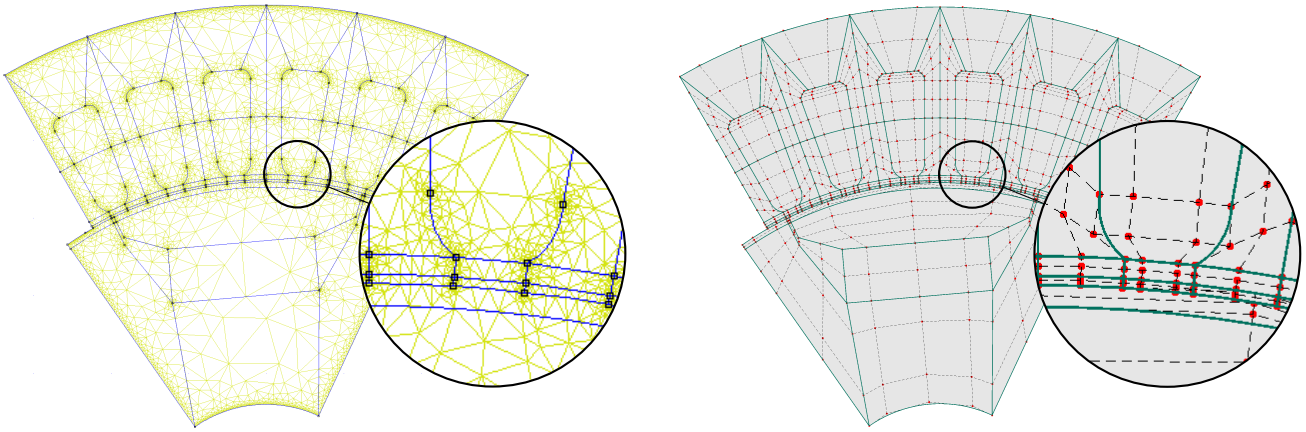

(a) Approximated geometry given by a triangle mesh. **(b)** Exact CAD geometry given by control points.

Figure 1.2: Geometry representation in the classical FEM and in IGA.

103], like genetic algorithms and particle swarm optimization (see, e.g., [105]). These methods have further been extended to address multi-objective optimization problems (see, e.g., [12, 86]). For permanent magnet synchronous machines, stochastic optimization methods are typically employed (see, e.g.,[11, 38, 149]). However, most design optimization approaches have the limitation that they primarily focus on optimizing pre-determined geometry parameters and do not allow for freeform optimization. In this work, we use shape calculus to obtain shape derivatives, thus enabling the possibility of gradient-based freeform shape optimization. This process allows us to exploit the advantages of IGA, particularly its capacity for straightforward geometry modifications [114].

The focus of this thesis lies on developing methods that are very well suited for the simulation of the electromagnetic phenomena in electric machines, corresponding to the second stage in Fig. 1.1. We focus on providing formulations which can use exact CAD geometries and can efficiently deal with rotation. Furthermore, we establish formulations and conditions to guarantee the stability and uniqueness of the solution. Employing these methods, we conduct an efficient freeform shape optimization of the machine, using shape calculus for gradient-based optimization. These approaches pave the way for comprehensive, multiphysical, and multi-objective optimization according to stages II-IV in the machine design process Fig. 1.1.

1.1 Research Goals

The goal of this work will be fundamental research in modeling and development of robust methodologies for designing electric machines. We will focus on *application-based objectives*, including accelerating the design workflow by using CAD data, i.e., splines instead of the traditional manual mesh generation, reducing computational cost by the use of high regularity basis functions, and improving the predictive accuracy of secondary phenomena in electric machines, e.g., deformation and NVH (noise, vibration, harshness) by using splines.

In addition to these practical objectives, this work aims to address more *theoretical aspects*. The focus will be on extending the theory of isogeometric domain decomposition and its practical applications. Here, an essential aspect that will be investigated is the choice of appropriate function spaces for the domain decomposition approaches and the regularization of the obtained formulations. Furthermore, we aim to use shape calculus in the context of IGA and electromagnetic problems to analyze the sensitivity of the machine with respect to its shape.

These goals will be achieved using a novel combination of mathematical building blocks including IGA in $H(\mathrm{curl};\Omega)$ and the corresponding trace spaces, adapted domain decomposition using Lagrange multipliers and freeform optimization. The combination of these functions has neither been investigated theoretically, nor been tested in practice.

1.2 Contributions

In this work efficient methods for the simulation and optimization of rotating electric machines are discussed. The theory for existing methods is extended and new methods are proposed to allow for a facilitated design process of electric machines. The main contributions can be summarized as follows:

1. Formal analysis of the stability of the harmonic mortar formulation and introduction of a stability condition for the choice of Lagrange multiplier space. Numerical investigation of the inf-sup constant confirms that the proven condition leads to a stable saddlepoint formulation. The harmonic mortar method is used for the efficient simulation of rotating electric machines [64] and cooling devices [162].

2. Development of a method for torque computation in three-dimensional isogeometric electric machine models, exploiting the Lagrange multipliers of the mortar method similarly to [50], where smooth and higher order basis functions can straightforwardly be employed. This renders the numerical differentiation to obtain the tangential component of the magnetic field unnecessary. Numerical investigation shows that the method is similarly accurate as the Arkkio method and significantly more efficient [116].

3. Development of a formulation for torque computation in two-dimensional electric machine models for the case of harmonic mortaring, based on the energy balance. This approach exploits the harmonic nature of Lagrange multipliers and their straightforward differentiation, enabling the reuse of the coupling matrices similarly to [50], thus bypassing additional numerical integrations. This method has been verified to converge to a reference solution for a PMSM model [63].

4. Reduction of the harmonic mortar formulation to a low-dimensional interface problem using a Schur complement, similar to the subdomain reduction using Dirichlet-to-Neumann mappings in [131]. The coupling matrix of the rotated rotor is decomposed into that of the unrotated rotor and a low-dimensional rotation matrix. Assembly of the matrices for different rotation angles becomes unnecessary and inverses of high-dimensional matrices can be precomputed [63].

5. Application of the Nitsche coupling method to isogeometric Maxwell problems. Numerical investigation shows the convergence of the solution with the degree of the basis function for both conforming and non-conforming discretizations [115].

6. Extension of the theory of three-dimensional isogeometric mortaring, such that the discrete kernel of the system coincides with the gradients of a suitable discrete space. A modified Lagrange multiplier space is proposed resulting in spurious-free solutions. The modified space solves problems caused by interior nodes at the mortar interface when applying gauging. Numerical investigation shows the stability of the saddlepoint problem by evaluation of the inf-sup constant. Furthermore, it is shown that the solution of the eigenvalue problem using the proposed space removes all spurious modes [95].
7. Extension of the concept of tree-cotree gauging to isogeometric analysis. Thanks to the existence of an isomorphism to the lowest order spline spaces, tree-cotree gauging can be straightforwardly applied to higher-order B-spline basis functions, with the tree being constructed directly on the hexahedral control mesh [95].
8. Development of a tree-cotree decomposition that works in combination with (isogeometric) mortaring. Application of the proposed tree-cotree gauging to the mortared electric machine model. Numerical analysis shows that the method converges with the degree of the basis functions for both conforming and non-conforming discretizations [95].
9. Development of a shape derivative of the total harmonic distortion (THD) of the electromotive force (EMF) in rotating machines using shape calculus. Development of a gradient-based shape optimization algorithm for the minimization of the THD of the EMF using the introduced shape derivative. Application of the developed shape optimization method to the PMSM achieving a reduction of the THD of $75\,\%$. The results are verified using commercial software [114].

1.3 Structure of this Treatise

This thesis is structured as follows: Chapter 2 focuses on the mathematical modeling. The basic concepts of electric machines are introduced, with a particular focus on PMSMs. However, the methods proposed in this thesis should be applicable to any other machine type. For the mathematical description of the relevant phenomena in electric machines, Maxwell's equations are introduced. Formulations capturing the relevant phenomena are derived, including in particular the magneto(quasi)static magnetic vector potential formulation.

Chapter 3 introduces the basics necessary for the numerical analysis conducted in this thesis. The weak formulation of the magnetostatic problem is derived for the three-dimensional setting and the reduction to the two-dimensional setting is discussed. The chapter also introduces the basic concepts of IGA, including the definition of B-splines and NURBS for both, the geometry representation and the solution, for which suitable B-spline spaces are presented. Furthermore, domain decomposition methods for non-conforming meshes are discussed, including harmonic coupling, mortaring and the Nitsche coupling method. Finally, tree-cotree gauging is introduced as a method to regularize the discrete three-dimensional formulation of the magnetostatic problem with a brief discussion on the application in IGA and difficulties concerning topology.

In Chapter 4, the numerical methods of Chapter 3 are investigated and their theory is extended for the simulation of electric machines. This chapter discusses the known B-spline function spaces for isogeometric mortaring and extends these spaces to obtain a new multiplier space, which ensures that the discrete kernel of the system exactly corresponds to the gradients of an appropriate discrete space, also in the multi-patch case. The application of tree-cotree gauging to IGA is discussed for the first time and an

adapted tree-cotree algorithm is proposed enabling the correct gauging of mortared problems for both IGA and FEM. The chapter explores different methods for the computation of the machine's torque, including the classical computation using the Maxwell stress tensor and the Arkkio method. Additionally, new strategies exploiting the Lagrange multipliers of the coupling are discussed in the context of IGA. These approaches utilize the exact radial and tangential components of the magnetic flux derived from the degrees of freedom, which is made possible due to the exact geometry mapping. Particularly, when it comes to harmonic mortaring, the inherent harmonic nature enables an efficient computation of the torque. The stability of the harmonic coupling method is analyzed and a condition to ensure the stability of the formulation is derived. Finally, a methodology for the simulation of full electric machine models is presented which alleviates the necessity of manually constructing a conforming spline discretization for the winding heads.

Chapter 5 discusses shape optimization using IGA. Shape sensitivity analysis is used to derive a shape derivative of the THD of the EMF for the first time. The shape derivative is used in a gradient-based algorithm for freeform shape optimization that is presented in this chapter. This derivative enables us to identify a shape gradient, i.e., a descent direction represented as a geometric vector field, which is then used to move the control points of the geometry, straightforwardly modifying the machine shape minimizing the objective function. This method offers a new promising approach to optimizing the shapes of rotating electric machines. By deriving the shape derivative of the respective objective function, the method can be adapted for other objectives. The incorporation of the proposed freeform shape optimization into the machine design workflow is presented.

In Chapter 6 numerical tests for all methods are conducted to corroborate the theoretical findings of the previous sections. The model problems used for the numerical tests are introduced, i.e., a simple unit cube model with a known analytical solution and the two- and three-dimensional models of the electric machine. The harmonic coupling method is investigated in terms of stability and performance of the Schur complement formulation.The convergence of the Nitsche method is investigated. Furthermore, different methods for torque computation in two and three dimensions are investigated and compared in terms of accuracy and computational effort. The proposed tree-cotree decomposition for mortaring, in combination with the adapted Lagrange multiplier space, is analyzed numerically in terms of stability, the absence of spurious modes and convergence and is then successfully applied to the electric machine model. Finally, the isogeometric freeform shape optimization algorithm of the previous chapter is applied to the PMSM model and the results are verified using commercial software.

The thesis concludes with a summary and provides an outlook for future research in Chapter 7.

2 Modeling

For the efficient design of electric machines, it is necessary to have an understanding of electromagnetic fields and their behavior. After sizing, (multiphysical) computer simulation and optimization are commonly used in industry [137]. The first step is the construction of a mathematical model capturing the relevant physical phenomena in the machine. The behavior of machines is primarily governed by electromagnetic fields. These can be mathematically described by Maxwell's equations. In this chapter, we introduce electromagnetic machines, the equations governing their behavior and some key performance indicators (KPIs).

2.1 Electromagnetics

The first rotating device which can be regarded as the ancestor of modern electric motors was built by Michael Faraday as early as 1821 [96]. Many observations and experiments of electromagnetic phenomena have been conducted in the early 19th century, among others, by Charles-Augustin de Coulomb, Alessandro Volta, Hans Christian Ørsted, André-Marie Ampère and Michael Faraday. However, the correlation between these phenomena had not been understood in a systematic way [132]. James Clerk Maxwell attempted to mathematically combine the observed phenomena in various papers, e.g., [109, 111], between 1855 and 1873 when he published his *A Treatise on Electricity and Magnetism* [110] which is the basis of the electromagnetic theory we use today. However, Maxwell did not write the equations in the form we know them nowadays. The equations were brought to their current, more elegant form by Oliver Heaviside [82], reducing the original number of equations and unknowns from twenty to four. These four equations which are still used today to describe electromagnetic fields are known as *Maxwell's equations*.

2.1.1 Maxwell's Equations

The behavior of electromagnetic fields can be described by Maxwell's equations [78, 91]. They can be written in integral form as

$$\int_{\partial A} \mathbf{E}(\mathbf{x},t)\cdot \mathrm{d}\,\mathbf{s} = -\int_{A} \frac{\partial \mathbf{B}(\mathbf{x},t)}{\partial t}\cdot \mathrm{d}\,\mathbf{A}, \tag{2.1}$$

$$\int_{\partial A} \mathbf{H}(\mathbf{x},t)\cdot \mathrm{d}\,\mathbf{s} = \int_{A} \left(\frac{\partial \mathbf{D}(\mathbf{x},t)}{\partial t} + \mathbf{J}(\mathbf{x},t)\right)\cdot \mathrm{d}\,\mathbf{A}, \tag{2.2}$$

$$\int_{\partial V} \mathbf{D}(\mathbf{x},t)\cdot \mathrm{d}\,\mathbf{A} = \int_{V} \rho(\mathbf{x},t)\,\mathrm{d}\,V, \tag{2.3}$$

$$\int_{\partial V} \mathbf{B}(\mathbf{x}, t) \cdot \mathrm{d}\,\mathbf{A} = 0, \tag{2.4}$$

where $A, V \in \mathbb{R}^3$ are simply connected, bounded surfaces and volumes with sufficiently smooth boundaries ∂A and ∂V, respectively, and $\mathbf{s}$ and $\mathbf{A}$ include the orientation of the line and surface normal. Here, the electric field density $\mathbf{E}$, the electric flux density $\mathbf{D}$, the electric current density $\mathbf{J}$, the magnetic field density $\mathbf{H}$ and the magnetic flux density $\mathbf{B}$ are vector functions of position $\mathbf{x} \in \mathbb{R}^3$ and time $t \in \mathbb{R}^+$. The electric charge density ρ is a scalar function with the same dependencies. Using Stokes' and Gauss's theorem for sufficiently smooth fields $\mathbf{F}$

$$\int_A (\nabla \times \mathbf{F}) \cdot \mathrm{d}\,\mathbf{A} = \int_{\partial A} \mathbf{F} \cdot \mathrm{d}\,\mathbf{s}, \tag{2.5}$$

$$\int_V \nabla \cdot \mathbf{F}\,\mathrm{d}\,V = \int_{\partial V} \mathbf{F} \cdot \mathrm{d}\,\mathbf{A}, \tag{2.6}$$

Maxwell's equations (2.1)–(2.4) in integral form can be rewritten in their differential formulation as

$$\nabla \times \mathbf{E}(\mathbf{x}, t) = -\frac{\partial \mathbf{B}(\mathbf{x}, t)}{\partial t}, \tag{2.1a}$$

$$\nabla \times \mathbf{H}(\mathbf{x}, t) = \frac{\partial \mathbf{D}(\mathbf{x}, t)}{\partial t} + \mathbf{J}(\mathbf{x}, t), \tag{2.2a}$$

$$\nabla \cdot \mathbf{D}(\mathbf{x}, t) = \rho(\mathbf{x}, t), \tag{2.3a}$$

$$\nabla \cdot \mathbf{B}(\mathbf{x}, t) = 0. \tag{2.4a}$$

Faraday's law (2.1) and (2.1a) describes the electric field that is induced by a time-varying magnetic flux. Ampère's law, stated in (2.2) and (2.2a), establishes that a time varying electric flux and an electric current can create a magnetic field. Gauss's law (2.3) and (2.3a) describes the electric flux that is created by an electric charge, whereas Gauss's law for magnetism (2.4) and (2.4a) states that there exist no magnetic charges or monopoles that create magnetic fields and thus, $\mathbf{B}$ is solenoidal.

In this work, we will only consider Maxwell's equations in simply connected finite domains $\Omega \in \mathbb{R}^3$ with sufficiently smooth boundary $\partial\Omega$, where we assume Ω to be open, bounded and simply connected. We will also discuss the case of domains that are not simply connected in Section 3.4.

Potentials There are different potential formulations that can be employed to solve Maxwell's equations, e.g., the $\mathbf{A}$-Φ, $\mathbf{A}^*$, $\mathbf{H}$-Φ or $\mathbf{T}$-Ω formulations [17, 26, 67, 94, 158]. Here, we will present the potentials of the $\mathbf{A}$-Φ formulation, namely the magnetic vector potential $\mathbf{A}$ and the electric scalar potential Φ, which are introduced such that

$$\mathbf{B}(\mathbf{x}, t) = \nabla \times \mathbf{A}(\mathbf{x}, t), \tag{2.7}$$

$$\mathbf{E}(\mathbf{x}, t) = -\frac{\partial \mathbf{A}(\mathbf{x}, t)}{\partial t} - \nabla \Phi(\mathbf{x}, t). \tag{2.8}$$

Using this, (2.4a) is automatically fulfilled due to the vector identity

$$\nabla \cdot (\nabla \times \mathbf{F}) = 0, \tag{2.9}$$

which is true for any sufficiently smooth vector field $\mathbf{F}$.

2.1.2 Material Laws

To complete Maxwell's equations we need constitutive laws which describe the relations between the electric and magnetic field and flux quantities depending on the material. These material relations are given by

$$\mathbf{D}(\mathbf{x},t) = \varepsilon_0 \varepsilon_\mathrm{r}(\mathbf{x},\mathbf{E})\mathbf{E}(\mathbf{x},t), \tag{2.10}$$
$$\mathbf{J}(\mathbf{x},t) = \sigma(\mathbf{x},\mathbf{E})\mathbf{E}(\mathbf{x},t) + \mathbf{J}_\mathrm{src}(\mathbf{x},t), \tag{2.11}$$
$$\mathbf{B}(\mathbf{x},t) = \mu_0 \mu_\mathrm{r}(\mathbf{x},\mathbf{H})\left(\mathbf{H}(\mathbf{x},t) + \mathbf{M}(\mathbf{x})\right), \tag{2.12}$$

where $\mathbf{J}_\mathrm{s}(\mathbf{x},t)$ is the source current density and $\mathbf{M}(\mathbf{x})$ is the magnetization of a permanent magnet [91]. Furthermore, ε_0 and μ_0 are the permittivity and permeability in vacuum, respectively and $\varepsilon_\mathrm{r}(\mathbf{x},\mathbf{E})$ denotes the relative permittivity, $\sigma(\mathbf{x},\mathbf{E})$ denotes the electrical conductivity and $\mu_\mathrm{r}(\mathbf{x},\mathbf{H})$ denotes the relative permeability, which are space-dependent and may also depend on field quantities. If they do not depend on the electromagnetic fields the dependencies on $\mathbf{E}$ and $\mathbf{H}$ will be dropped. Otherwise, to obtain linear constitutive laws, the material relations can be approximated by the chord or differential material properties [49] which do not depend on the fields. In the following, the absolute permittivity and permeability will be denoted by $\varepsilon = \varepsilon_0\varepsilon_\mathrm{r}$ and $\mu = \mu_0\mu_\mathrm{r}$, and the inverse permeability $\nu = \mu^{-1}$ is called the reluctivity. In the following, we will omit the spatial and temporal dependencies for the sake of readability.

2.1.3 Interface and Boundary Conditions

From Maxwell's equations in integral form (2.1)–(2.4), one can derive the continuity conditions that have to hold at the interface of different materials [91, Chapter I.5]. For the electric and magnetic field, the continuity conditions of the tangential components at an interface Γ are given by

$$\mathbf{n} \times (\mathbf{E}_1 - \mathbf{E}_2) = \mathbf{0} \qquad \text{on } \Gamma, \tag{2.13}$$
$$\mathbf{n} \times (\mathbf{H}_1 - \mathbf{H}_2) = \mathbf{J}_A \qquad \text{on } \Gamma, \tag{2.14}$$

where $\mathbf{n}$ is the normal vector of Γ and the subscripts in $\mathbf{E}_1$ and $\mathbf{E}_2$ denote the electric fields on both sides of the interface Γ, and $\mathbf{H}_1$ and $\mathbf{H}_2$ correspondingly. This means that the electric field has continuous tangential components across the interface, while the tangential components of the magnetic field can jump by the magnitude of a surface current density $\mathbf{J}_A$, e.g., if the interface models a thin conductive layer. However, it vanishes in all cases relevant for this thesis, i.e., $\mathbf{J}_A = \mathbf{0}$. This means that the tangential components of the magnetic field are continuous.

The normal components of the electric and magnetic flux density are continuous across an interface, unless there are surface charge densities, i.e.,

$$\mathbf{n} \cdot (\mathbf{D}_1 - \mathbf{D}_2) = \rho_A, \qquad \text{on } \Gamma, \tag{2.15}$$
$$\mathbf{n} \cdot (\mathbf{B}_1 - \mathbf{B}_2) = 0, \qquad \text{on } \Gamma. \tag{2.16}$$

where ρ_A is a surface charge density.

When solving partial differential equations (PDEs), in our case Maxwell's equations (2.1a)–(2.4a), we usually consider a domain $\Omega \subset \mathbb{R}^3$ with boundary $\partial\Omega$. In this case it is necessary to set boundary conditions

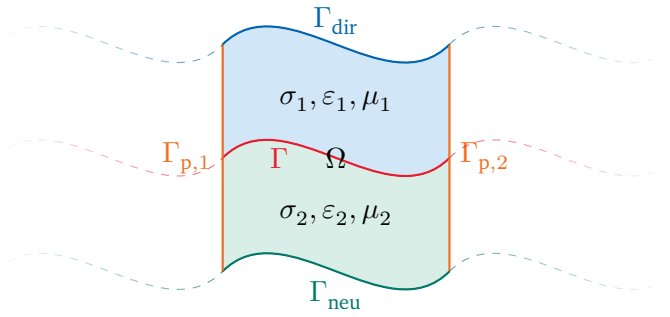

Figure 2.1: Periodic domain consisting of two materials with interface Γ, Dirichlet, Neumann and periodic boundaries Γ_{dir}, Γ_{neu}, $\Gamma_{\text{p,1}}$ and $\Gamma_{\text{p,2}}$, respectively.

(BCs) on $\partial\Omega$. If we model the boundary as a perfect electric conductor (PEC) or a perfect magnetic conductor (PMC), i.e., $\sigma \to \infty$ and $\varepsilon \to \infty$ or $\mu \to \infty$ on the outside domain, we obtain an *electric boundary condition* or a *magnetic boundary condition*, respectively. These can be derived using (2.13) and (2.14) together with the fact that the fields vanish inside perfect conductors as

$$\mathbf{n} \times \mathbf{E} = \mathbf{0} \qquad \text{and} \qquad \mathbf{n} \times \mathbf{H} = \mathbf{0}, \tag{2.17}$$

respectively, with the *outward* normal vector $\mathbf{n}$. In mathematical terms, a condition prescribing the value of a solution at a boundary is called Dirichlet boundary condition. For a vector field $\mathbf{F}$, for example the electric or magnetic field, it can be written as

$$\mathbf{n} \times \mathbf{F} = \mathbf{g} \qquad \text{on } \Gamma_{\text{dir}} \subset \partial\Omega, \tag{2.18}$$

where $\mathbf{g}$ is a prescribed function on Γ_{dir}. Therefore, a homogeneous Dirichlet BC, i.e., $\mathbf{g} = \mathbf{0}$, corresponds to an electric boundary condition for $\mathbf{F} = \mathbf{E}$. Prescribing the normal derivative of the solution is equivalent to setting a Neumann BC. For a vector field $\mathbf{F}$, e.g., the electric or magnetic field, the Neumann BC is given by

$$\mathbf{n} \times (\nabla \times \mathbf{F}) = \mathbf{h} \qquad \text{on } \Gamma_{\text{neu}} \subset \partial\Omega, \tag{2.19}$$

where $\mathbf{h}$ is a prescribed function on Γ_{neu}. In the case of a primal formulation as it is used in this thesis, a homogeneous Dirichlet BC, i.e., $\mathbf{g} = \mathbf{0}$, corresponds to an electric boundary condition, e.g., for $\mathbf{F} = \mathbf{E}$, acting as a magnetic flux barrier and a homogeneous Neumann BC, i.e., $\mathbf{h} = \mathbf{0}$, corresponds to a magnetic BC, e.g., for $\nabla \times \mathbf{F} = \mathbf{H}$. We will use the terms Dirichlet and Neumann BC in the following.

When solving a problem on a periodic domain, we can use periodic boundary conditions in order to reduce the problem domain to only one period of the domain. In this case we still have to ensure that the corresponding interface conditions are fulfilled between the two periodic boundary parts $\Gamma_{\text{p,1}}$ and $\Gamma_{\text{p,2}}$. There are other boundary conditions that might be used, however, we will only use Dirichlet, Neumann and periodic boundary conditions in this thesis, i.e., we assume that the whole boundary is given by

$$\partial\Omega = \Gamma_{\text{dir}} \cup \Gamma_{\text{neu}} \cup \Gamma_{\text{p,1}} \cup \Gamma_{\text{p,2}}. \tag{2.20}$$

A visualization of a domain with a material interface and Dirichlet, Neumann and periodic boundaries is shown in Fig. 2.1.

2.1.4 Maxwell Eigenvalue Problem

When considering resonating structures, e.g., electromagnetic cavities, we are usually interested in electromagnetic fields which can oscillate in the structure, see, e.g., [43]. These fields are given by the solution of the Maxwell eigenvalue problem in a simply connected, bounded domain Ω,

$$\begin{aligned} \nabla \times (\nu \nabla \times \mathbf{E}) &= \varepsilon \omega^2 \mathbf{E} && \text{in } \Omega \\ \nabla \cdot \varepsilon \mathbf{E} &= 0 && \text{in } \Omega \\ \mathbf{n} \times \mathbf{E} &= \mathbf{0} && \text{on } \partial\Omega \end{aligned} \tag{2.21}$$

which is obtained from (2.1a)–(2.4a) and (2.10)–(2.12) with homogeneous Dirichlet BC in the absence of currents, charges and conducting material. The solutions of (2.21) are the eigenpairs $(\mathbf{E}_i, \omega_i)$. In this work, we will use the Maxwell eigenvalue problem for the numerical investigation of the proposed methods regarding the correctness of the used (discrete) function spaces. This is possible because using non-suitable discrete function spaces leads to unphysical solutions, so called spurious modes [43, 150].

2.2 Harmonic Fields

According to the Helmholtz decomposition in contractible domains a vector field is uniquely described by its divergence and curl [78]. Therefore, there is a trivial solution for a vector field $\mathbf{F}$ fulfilling $\nabla \cdot \mathbf{F} = 0$ and $\nabla \times \mathbf{F} = \mathbf{0}$. Harmonic fields are nontrivial vector fields that are divergence- and curl-free. They only occur in domains which are not contractible [3, 7]. Let us consider for example a domain that is a hollow sphere. In this domain a vector field with only a radial component given by

$$\mathbf{F}(r, \theta, \varphi) = \frac{1}{r^2} \mathbf{e}_r, \tag{2.22}$$

in a spherical coordinate system where $\mathbf{e}_r$ is the unit vector in radial direction, as visualized in Fig. 2.2a, satisfies both conditions, despite not being the trivial solution. However, since this non-trivial field is curl-free and the domain is path-connected, it can be represented by a gradient field.

Another case where we can obtain harmonic fields is in the case of a domain that has the shape of a torus. It can easily be seen that, for example, a field that has only an angular component that is constant in angular direction and decreasing in radial direction with a factor $\frac{1}{r}$, with r being the radial coordinate in a cylindrical coordinate system, i.e.,

$$\mathbf{F}(r, \varphi, z) = \frac{1}{r} \mathbf{e}_\varphi, \tag{2.23}$$

with the unit vector $\mathbf{e}_\varphi$ in angular direction, also satisfies both conditions. Such a field is visualized in Fig. 2.2b. In this case, the harmonic field cannot be represented as a gradient field. It can easily be seen

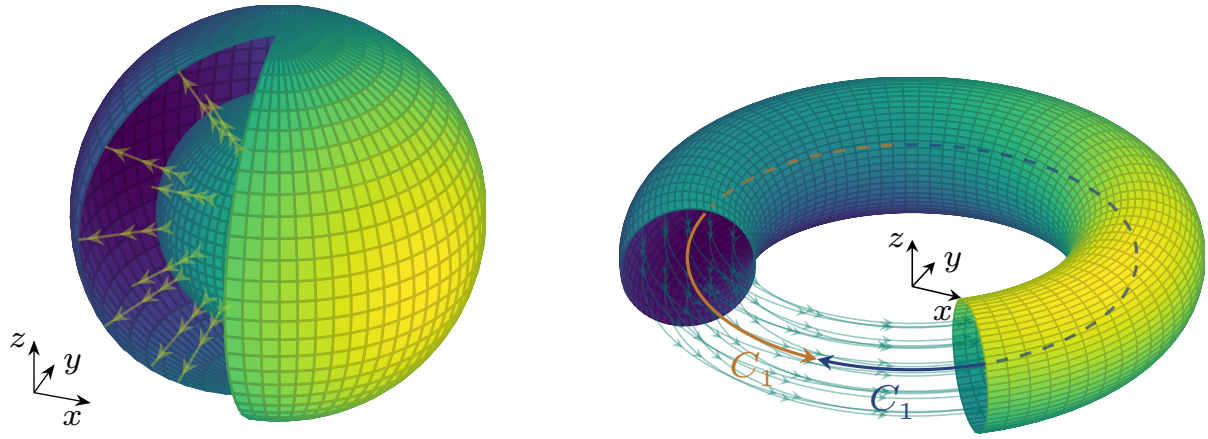

(a) Harmonic field in a hollow sphere domain.

(b) Harmonic field in a torus domain.

Figure 2.2: Harmonic fields in a hollow sphere and a torus domain.

that a line integral in the domain between two points is not line independent when integrating along a curve going around the hole in the center in different directions, i.e.,

$$\int_{C_1} \mathbf{F} \cdot \mathrm{d}\mathbf{s} \neq \int_{C_2} \mathbf{F} \cdot \mathrm{d}\mathbf{s}. \tag{2.24}$$

Therefore, for multiply connected domains, harmonic fields lie in the kernel of the curl-operator in addition to gradient fields and have to be considered for the gauging to guarantee a unique solution.

Note, that BCs play an important role in the question if a harmonic field exists for a specific problem. As an example, in the hollow sphere domain, we can find a harmonic field that satisfies (homogeneous or constant) Dirichlet BCs on the inner boundary and homogeneous Neumann BCs on the outer boundary or vice versa. However, we cannot construct a nontrivial harmonic field satisfying, e.g., homogeneous Dirichlet BCs on inner and outer boundary. For the torus, it is also not possible to find a harmonic field that fulfills homogeneous Dirichlet BCs.

Harmonic fields may occur, e.g., when modeling electric machines as toroidal domains or with periodic boundary conditions. Of course, there are more complex geometries where harmonic fields can occur, see, e.g., [59].

2.3 Electric Machines

Electric machines are electromechanichal energy converters that can be found in many industrial and household applications. When operated as motors, they convert electric energy to kinetic energy and vice versa when operated as generators [16]. Their functionality is based on the principle of electromagnetic induction. A current flowing through a conductor generates a magnetic field. The interaction of this magnetic field with an external one induces a force on the conductor. This force is exploited in electric machines to create motion in their moving components. There are linear and rotary machines. This work focuses on rotary electric machines, however, the proposed methods can be straightforwardly be applied to other machine types. Rotary machines consist of a stationary component known as the stator and a rotating

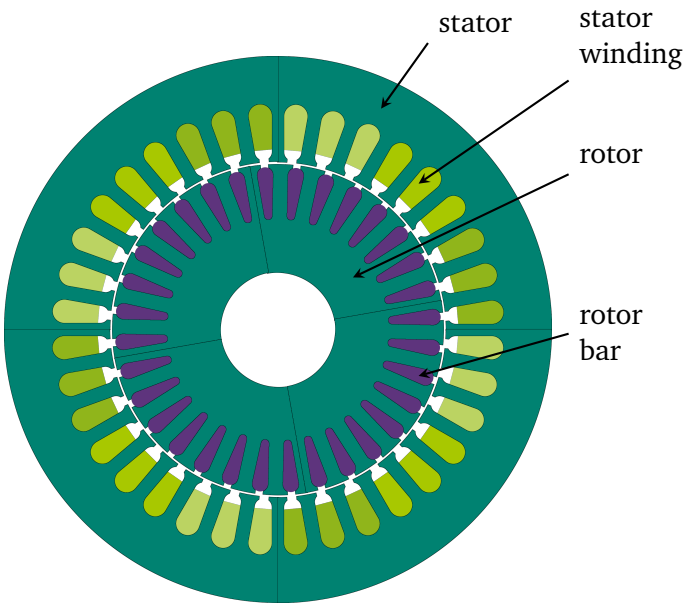

Figure 2.3: Example of one pole of a four-pole asynchronous machine. Onelab [75] model `im_3kw.pro`, see also [79].

component called the rotor and an air gap separating rotor and stator. Commonly, these machines have a cylindrical structure with the stator on the outside containing multiphase windings, where the number of phases will be denoted by N_k in the following, and a rotor on the inside with a setup that depends on the motor type, see Fig. 2.4. While this work focuses specifically on radial flux machines, where the magnetic flux flows perpendicular to the machine axis, it is worth noting that the proposed methods are applicable to other machine types, e.g., axial flux machines, where the magnetic flux flows parallel to the machine axis, could also benefit from these methods. Isogeometric analysis (IGA) has been successfully employed for the simulation of axial flux machines in [68]. Electric machines are traditionally classified into commutator machines, asynchronous (or induction) machines, and synchronous machines. As the significance of brushed direct current (DC) commutator machines is decreasing, the market for alternating current (AC) machines, e.g., synchronous and asynchronous machines, is growing each year [76]. This work will therefore outline the fundamental principles of synchronous and asynchronous machines. Other machine types, e.g., reluctance machines will not be considered in this work.

Asynchronous machines Asynchronous machines, also called induction machines, are used in many appliances. Their rotor contains either windings or, in the case of the most popular type, i.e., the (squirrel) cage induction machine, contains conductive bars, which typically consist of copper or aluminum [16]. An example of an asynchronous machine geometry is shown in Fig. 2.3. The multiphase stator windings are supplied with an AC, generating a rotating magnetic field. This field then induces currents in the rotor windings or bars, which create a rotor magnetic field opposing that of the stator. The interaction between these fields exerts a torque on the rotor, setting it in motion. The relative difference between the rotational speed of the stator field and the rotational speed of the rotor is called the slip, which enables the generation of this torque. Consequently, no torque is transmitted when the rotor rotates at the synchronous speed with the stator magnetic field (zero slip). This gives the asynchronous machine its name. Asynchronous/induction machines can be operated as motors generating torque when the rotor

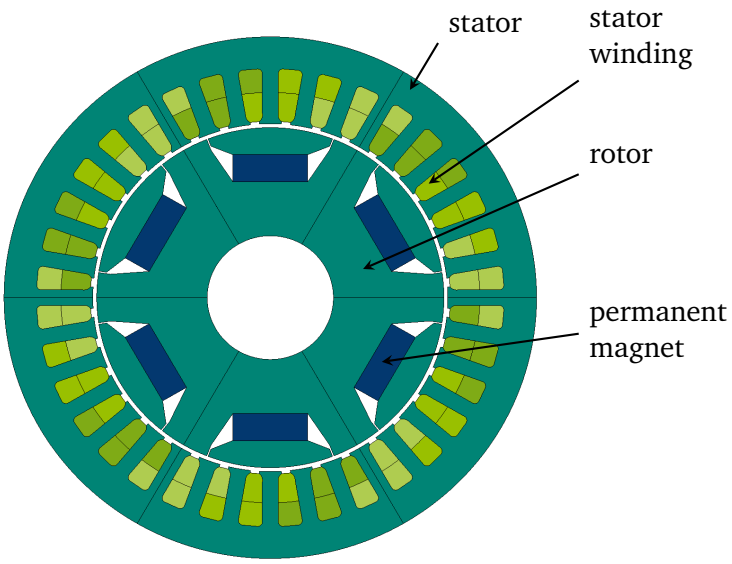

Figure 2.4: Example of a permanent magnet synchronous machine with six poles, original design[123].

rotates at a lower frequency than the stator field, or as generators generating electricity when driven by an external mechanical force at a higher rotational speed than the stator field. Induction machines do not require power electronic converters for constant speed operation. They have gained popularity due to their straightforward construction and maintenance, without the general need for commutator or slip rings, along with their cost-effectiveness [76].

Synchronous machines This thesis focuses on the simulation of synchronous machines. In synchronous machines, the rotor contains windings or permanent magnets which generate a magnetic field. The number of magnetic pole pairs will be called N_p in the following. The stator's multiphase winding generates a rotating magnetic field, which interacts with the rotor's magnetic field, causing the rotor to rotate at synchronous speed. Depending on the load angle, i.e., the phase difference between the rotating stator field and the rotor field, the machine can be operated in motor mode as previously explained, or in generator. In generator mode, the rotating rotor induces a voltage, called the electromotive force (EMF), in the stator windings, generating an AC current with a frequency proportional to the rotational speed of the rotor. Among machine types, permanent magnet synchronous machines (PMSMs) exhibit the highest energy density and do not require an additional DC power supply to the rotor. However, they exhibit cogging torque which negatively affects their operation smoothness. In contrast to asynchronous machines, synchronous machines always require frequency converters, as they can only be operated at synchronous speed. However, this disadvantage is mitigated by the decreasing cost of power electronics components. Furthermore, due to the increased need for controllability and efficiency power electronics are also employed in asynchronous machines. From a motor control point of view, synchronous machines have several advantages over asynchronous machines, including a torque proportional to the input voltage and a speed dependence only on the input frequency [76]. In this thesis, we will consider the PMSM shown in Fig. 2.4. The design is derived from a machine that was originally designed as part of a tool machine [123, page 124]. The parameters for the geometry and materials of the machine have been taken from [22, Chapter V.A].

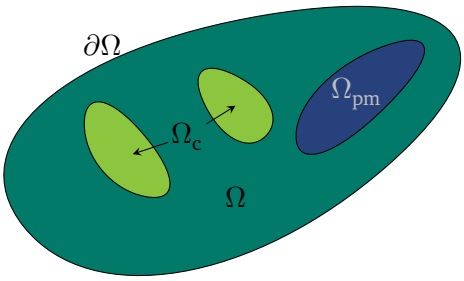

Figure 2.5: Example for a domain Ω with coil region Ω_{c}, permanent magnet region Ω_{pm} and domain boundary $\partial\Omega$. Adapted from [114]. ©2021 IEEE

2.3.1 Magnetoquasistatic Formulation

It is not always necessary to consider the whole set of Maxwell's equations. Depending on the application it can suffice to only consider a simplifying approximation of Maxwell's equations. If capacitive effects can be neglected, as it is often the case for electric machines, we can employ the magnetoquasistatic (or eddy current) approximation of Maxwell's equations. In this case, the variation of the electric flux density is negligible compared to the electric current density. The time derivative of the electric flux density can thus be disregarded, yielding the relevant equations

$$\nabla \times \mathbf{E} = -\frac{\partial \mathbf{B}}{\partial t}, \tag{2.1b}$$

$$\nabla \times \nu\mathbf{B} = \mathbf{J}_{\mathrm{src}} + \sigma\mathbf{E} + \nabla \times \mathbf{M}, \tag{2.2b}$$

$$\nabla \cdot \mathbf{B} = 0. \tag{2.4b}$$

Various potential formulations can be employed to to solve the magnetoquasistatic problem, including the $\mathbf{A}$-Φ, $\mathbf{A}^*$, $\mathbf{H}$-Φ or $\mathbf{T}$-Ω formulations [17, 44, 67, 94, 158]. Here, we use an $\mathbf{A}^*$ potential formulation [67]. With (2.11), (2.12) and (2.1b)–(2.4b) and the magnetic vector potential which is defined by

$$\mathbf{B} = \nabla \times \mathbf{A}^*, \tag{2.25}$$

we obtain the potential formulation of the eddy current problem

$$\nabla \times (\nu \nabla \times \mathbf{A}^*) + \sigma \frac{\partial \mathbf{A}^*}{\partial t} = \mathbf{J}_{\mathrm{src}} + \nabla \times \mathbf{M}, \tag{2.26}$$

with the (modified) magnetic vector potential $\mathbf{A}^*$, which we will simply call $\mathbf{A}$ in the following. For electric machines, the source current density

$$\mathbf{J}_{\mathrm{src}} = \sum_{k=1}^{N_k} \boldsymbol{\chi}_k i_k \tag{2.27}$$

is described by distribution functions $\boldsymbol{\chi}_k$ and currents i_k where k indicates that the winding belongs to the k-th phase in a N_k-phase winding [146]. The winding functions $\boldsymbol{\chi}_k$ vanish outside the coil region of the k-th phase winding. An abstract sketch of the domain Ω containing coil regions Ω_{c}, where the machine windings are defined, and permanent magnet regions Ω_{pm} is given in Fig. 2.5 . The magneti-

zation of the permanent magnets is given by $\mathbf{M}$ and vanishes outside of the permanent magnet region Ω_{pm}. To reduce Joule losses in electric machines, whenever possible, parts are made up of laminated material, such that the effects of eddy currents are minimized and can be neglected in the field simulation and estimated by loss models [112]. This is in particular the case for most PMSMs and we therefore disregard the corresponding term. Hence, we can use the magnetostatic approximation of Maxwell's equations, where all time derivatives go to zero and (2.26) reduces to the magnetostatic potential formulation

$$\nabla \times (\nu \nabla \times \mathbf{A}) = \mathbf{J}_{\text{src}} + \nabla \times \mathbf{M}. \tag{2.28}$$

Dirichlet and Neumann BCs for the magnetic vector potential that are consistent with (2.18) and (2.19) are given by

$$\mathbf{n} \times \mathbf{A} = \mathbf{g} \qquad \text{on } \Gamma_{\text{dir}}, \tag{2.29}$$
$$\mathbf{n} \times \nu (\nabla \times \mathbf{A}) = \mathbf{h} \qquad \text{on } \Gamma_{\text{neu}}. \tag{2.30}$$

with given functions $\mathbf{g}$ and $\mathbf{h}$, respectively. In the case of homogeneous Dirichlet BCs, i.e., $\mathbf{g} = \mathbf{0}$, this corresponds to an electric BC consistent with (2.17). Physically, this can be interpreted as a magnetic flux barrier meaning that the normal component of the magnetic flux density vanishes $\mathbf{B} \cdot \mathbf{n} = 0$. A homogeneous Neumann BC with $\mathbf{h} = \mathbf{0}$ corresponds to a magnetic BC consistent with (2.17) and can be interpreted as setting the tangential components of the magnetic field strength $\mathbf{H} \cdot \mathbf{t} = 0$ where $\mathbf{t} \perp \mathbf{n}$ is any vector tangential to the boundary $\partial\Omega$. To prove existence and uniqueness of the magnetic vector potential, Alonso et. al [3] formulate a mixed problem using either the Coulomb or Lorenz gauge. This gauge freedom can be deduced from the Helmholtz decomposition. It states that any vector field in a simply connected domain can be expressed as the sum of a divergence-free (solenoidal) vector field and a curl-free (irrotational) vector field [78, 117]

$$\mathbf{F} = \underbrace{\nabla p}_{\text{irrotational}} + \underbrace{\nabla \times \mathbf{w}}_{\text{solenoidal}}. \tag{2.31}$$

This had motivated the use of the magnetic vector potential (2.7). However, the fields p and $\mathbf{w}$ of the Helmholtz decomposition are not unique as we can add any constant c or gradient field $\nabla\psi$, respectively, without changing the original vector field

$$\mathbf{F} = \nabla(p + c) + \nabla \times (\mathbf{w} + \nabla\psi) = \nabla p + \nabla \times \mathbf{w}. \tag{2.32}$$

This is because constants and gradient fields lie in the kernel of the gradient and curl operators, respectively. In particular in (2.7), we see that we can also add any gradient field to the magnetic vector potential without changing the physical $\mathbf{B}$-field. The Helmholtz decomposition also implies that any vector field is uniquely defined by its curl and its divergence [78] in a finite domain with boundary conditions or in free space with appropriate radiation conditions ensuring that the fields go to zero at infinity. We have only specified the curl of the magnetic vector potential in (2.7). Therefore, $\mathbf{A}$ is not uniquely defined, such that (2.28) does not have a unique solution. To obtain a unique solution for (2.28), we have to set a gauging condition to fix the divergence of $\mathbf{A}$ [18]. Gauging will be discussed in more detail in Section 3.4.

Two-Dimensional Model For electric machines, the problem can often be reduced to two-dimensional (2D) planar model in the x-y-plane [141, 154]. This is achieved by considering a cross section of the

machine and assuming A_x, A_y, $J_{\text{src},x}$, $J_{\text{src},y}$ and M_z vanish and $\partial_z = 0$, where F_u denotes the u-component of the vector field $\mathbf{F} \in \{\mathbf{A}, \mathbf{J}, \mathbf{M}\}$ for $u \in \{x, y, z\}$ and $\partial_u = \frac{\partial}{\partial u}$. For the sake of a more compact notation, the index z is dropped. In this case the magnetostatic potential equation (2.28) with homogeneous boundary conditions reduces to a Poisson problem

$$-\nabla \cdot (\nu \nabla A) = J_{\text{src}} - \nabla \cdot \mathbf{M}^{\perp} \qquad \text{in } \Omega \tag{2.33}$$

$$A = g \qquad \text{on } \Gamma_{\text{dir}} \tag{2.34}$$

$$\mathbf{n} \cdot (\nabla A) = h \qquad \text{on } \Gamma_{\text{neu}}, \tag{2.35}$$

where $\mathbf{M}^{\perp} = \begin{bmatrix} -M_y, M_x \end{bmatrix}^{\top}$ is the rotated magnetization vector and (2.34) and (2.35) are Dirichlet and Neumann BCs with the prescribed functions g and h. Here, we assume the reluctivity to be isotropic. In the case of non-isotropic material, the reduction of the reluctivity to two-dimensions is not as straightforward as it is not the inverse of the reduced permeability. For details on the reduction in the anisotropic case, see e.g., [162]. Furthermore, in the case of our electric machine, we assume homogeneous Dirichlet BCs on the whole boundary, i.e., $g = 0$ on $\Gamma_{\text{dir}} = \partial\Omega$. Again, due to the non-continuous material and right-hand side in the general case, we refer to the weak formulation of the problem for the proof of existence and uniqueness, see also Section 3.1 [117, Theorem 3.14].

Furthermore, note that problems with inhomogeneous Dirichlet BCs can be reduced to problems with homogeneous Dirichlet BCs by homogenizing the BCs [28]. Therefore, we will assume homogeneous Dirichlet BCs in the following without loss of generality .

2.3.2 Electroquasistatic Formulation

In electric machines, commonly capacitive effects are disregarded. However, in the case when inductive effects in a system can be neglected, the electroquasistatic approximation of Maxwell's equations can be employed. This is the case if electric fields are dominant in the system and the variation of the magnetic flux density is negligible. The relevant set of Maxwell's equations for electroquasistatics is given by

$$\nabla \times \mathbf{E} = \mathbf{0}, \tag{2.1c}$$

$$\nabla \times \mathbf{H} = \frac{\partial \varepsilon \mathbf{E}}{\partial t} + \sigma \mathbf{E} + \mathbf{J}_{\text{src}}, \tag{2.2c}$$

$$\nabla \cdot \varepsilon \mathbf{E} = \rho. \tag{2.3c}$$

As the electric field is irrotational according to (2.1c), it can be represented by an electric scalar potential Φ as

$$\mathbf{E} = -\nabla \Phi. \tag{2.36}$$

Applying the divergence operator to (2.2c) and inserting Gauss's law, we obtain the electroquasistatic potential equation

$$-\nabla \cdot \left(\frac{\partial}{\partial t} \varepsilon \nabla \Phi \right) - \nabla \cdot (\sigma \nabla \Phi) = \nabla \cdot \mathbf{J}_{\text{src}}, \tag{2.37}$$

where the BCs are given by

$$\Phi = g \qquad \text{on } \Gamma_{\text{dir}} \tag{2.38}$$

$$\mathbf{n} \cdot (\nabla \Phi) = h \qquad \text{on } \Gamma_{\text{neu}}. \tag{2.39}$$

In the static limit, i.e., $\frac{\partial}{\partial t} = 0$ and the absence of source currents, the electroquasistatic problem is reduced to the stationary current problem in the conducting domain Ω_c

$$\nabla \cdot (\sigma \nabla \Phi) = 0, \qquad \text{in } \Omega_c, \tag{2.40}$$

$$\Phi = g \qquad \text{on } \Gamma_{\text{dir}} \tag{2.41}$$

$$\mathbf{n} \cdot (\nabla \Phi) = h \qquad \text{on } \Gamma_{\text{neu}}, \tag{2.42}$$

which can be employed to compute the current distribution function $\boldsymbol{\chi}$ from (2.27) in the windings of electric machines, see for details Section 4.4 and [146].

2.3.3 Key Performance Indicators of Electric Machines

In the design of electric machines there are various KPIs. They play an important role in the optimization process, where up to 20 KPIs are considered [124]. Among them are, e.g., torque, cost, efficiency and noise, vibration, harshness (NVH) characteristics. In the following, we introduce KPIs which will be used in the optimization in Chapter 5.

Torque One of the KPIs of electric machines is the mechanical torque [16, 76] which describes the rotational force. Electromagnetic torque is caused by the interaction of electromagnetic fields. In the case of electric motors, it is caused by the magnetic fields, induced by the currents in the windings and by permanent magnets in the case of permanent magnet machines.

The electromagnetic torque acting on a volume can be calculated by integrating the Maxwell stress tensor $\boldsymbol{\sigma}$, over a closed surface enclosing this volume, see, e.g., [91, 141]. Its entries in a homogeneous medium with permeability μ_0 are given by

$$\sigma_{ij} = \nu_0 \left(B_i B_j - \frac{1}{2} |\mathbf{B}|^2 \delta_{ij} \right), \tag{2.43}$$

with $i, j \in \{1, 2, 3\}$ and B_1, B_2, and B_3 corresponding to the x-, y- and z-component of the $\mathbf{B}$-field, respectively, and δ_{ij} denotes the Kronecker delta. The torque on the volume V can then be calculated by

$$\mathbf{T} = \oint_{\partial V} \mathbf{x} \times \boldsymbol{\sigma} \cdot \, \mathrm{d}\mathbf{S}, \tag{2.44}$$

where $\mathbf{x} \in \partial V$ is the position vector on the boundary of the volume and $\mathbf{S}$ includes the normal direction of the integration surface, see [6, 98].

Electromotive force Another important quantity of interest is the counter- or back-EMF, also simply called EMF [76, 78, 114]. The EMF $\mathcal{E}_k$ is defined as the voltage that is induced in the winding k when the motor is rotating, assuming that the coils of the poles are connected in series. The EMF in the k-th winding can be computed by

$$\mathcal{E}_k(\mathbf{A}(t)) = \partial_t \Psi_k(\mathbf{A}(t)), \tag{2.45}$$

with the flux linkage

$$\Psi_k(\mathbf{A}(t)) = N_p \int_\Omega \boldsymbol{\chi}_k \cdot \mathbf{A}(t) \ \mathrm{d}\Omega, \tag{2.46}$$

where N_p is the number of pole pairs and $\boldsymbol{\chi}_k$ is the winding function of the k-th winding, see (2.27). Note that $\mathbf{A}$ depends on both space and time. While the dependence on $\mathbf{x}$ is dropped for the sake of readability, the dependence on t is explicitly stated here, as this will be necessary later in this thesis.

Total Harmonic Distortion The total harmonic distortion (THD) of a function is a measure for the distortion of the respective function from a sinusoidal wave of a base frequency [114, 163]. The THD of a function, e.g., the EMF $\mathcal{E} = \mathcal{E}(t)$ is defined as

$$\mathrm{THD}_{\mathcal{I}}(\mathcal{E}) = \frac{\sqrt{\sum_{n\in\mathcal{I}, n\neq 1} |c_n|^2}}{|c_1|}, \tag{2.47}$$

where c_n are the coefficients of the Fourier expansion of $\mathcal{E}(t)$, i.e.,

$$\mathcal{E}(t) = \sum_{n=-\infty}^{\infty} c_n e^{\imath n t}, \tag{2.48}$$

and $\mathcal{I} \subset \mathbb{N}$ is an index-set of frequencies to consider. An alternative representation of the Fourier series (2.48) is given by

$$\mathcal{E}(t) = \frac{\mathcal{A}_0}{2} + \sum_{n=1}^{\infty} \mathcal{A}_n \cos(nt) + \mathcal{B}_n \sin(nt) \tag{2.49}$$

with the coefficients

$$\mathcal{A}_n = c_n + c_{-n} \text{ for } n \geq 0 \quad \text{and} \quad \mathcal{B}_n = \imath(c_n - c_{-n}) \text{ for } n \geq 1. \tag{2.50}$$

Note that $|c_n| = \sqrt{\mathcal{A}_n^2 + \mathcal{B}_n^2}/2$ holds. With this representation, the THD can be rewritten as

$$\mathrm{THD}(\mathcal{E}) = \sqrt{\frac{\sum_{n\in\mathcal{I}, n\neq 1} \mathcal{A}_n^2 + \mathcal{B}_n^2}{\mathcal{A}_1^2 + \mathcal{B}_1^2}}. \tag{2.51}$$

2.4 Summary

In this chapter, we have introduced the fundamental equations necessary for describing the behavior of electric machines. Maxwell's equations and the constitutive laws provide tools to understand and describe electromagnetic fields in general. From this general setting, the magnetoquasistatic and electroquasistatic formulations were derived as approximations for slowly varying fields. Additionally, we discussed the simplifications that can be applied in two dimensions, which are commonly used in electric motor simulations. A short introduction on electric machines was given and some KPIs were introduced which will be quantities of interest in the following chapters, including the torque, the electromotive force and the total harmonic distortion. Finally, the concept of harmonic fields for non-contractible domains was introduced

which will be relevant later in this thesis. The introduced problems will be translated to discrete formulations which can be solved computationally in the following chapter.

3 Basics of Numerical Analysis

To solve real-world physical problems, computers are employed when a closed-form solution of the underlying PDE cannot be derived. Numerical methods tackle these problems by discretizing the problem's geometry and solution. In this chapter, we give a review on existing methods we employ for the simulation of electric machines. We use the Galerkin finite element method (FEM) [28, 117] based on the weak formulation of the PDE, i.e., the magnetostatic problem (2.28). Splines serve as basis functions for the geometry and discretization which leads to a method that is also known as IGA [88]. Non-conforming interfaces and gauging are discussed. This chapter is based on [45, 88, 95, 114, 116].

3.1 Weak Formulations

The various electromagnetic fields need to satisfy certain regularity conditions, meaning that they belong to specific function spaces. Specifically, in the context of Maxwell's equations, the fields are contained in one of the Sobolev spaces [117]

$$H^1(\Omega) = \left\{u \in L^2(\Omega) : \nabla u \in (L^2(\Omega))^3\right\}, \tag{3.1}$$

$$H(\mathrm{curl};\Omega) = \left\{\mathbf{u} \in (L^2(\Omega))^3 : \nabla \times \mathbf{u} \in (L^2(\Omega))^3\right\}, \tag{3.2}$$

$$H(\mathrm{div};\Omega) = \left\{\mathbf{u} \in (L^2(\Omega))^3 : \nabla \cdot \mathbf{u} \in L^2(\Omega)\right\}, \tag{3.3}$$

and the space of square integrable functions

$$L^2(\Omega) = \left\{u : \int_\Omega |u|^2 \,\mathrm{d}\Omega < \infty\right\}. \tag{3.4}$$

We use the same notation but with subscript 0, e.g., $H_0(\mathrm{curl};\Omega)$, for spaces with homogeneous Dirichlet BC on Γ_{dir}. These spaces satisfy the well-known de Rham sequence, also known as the de Rham complex [117]

$$H^1(\Omega) \xrightarrow{\nabla} H(\mathrm{curl};\Omega) \xrightarrow{\nabla\times} H(\mathrm{div};\Omega) \xrightarrow{\nabla\cdot} L^2(\Omega), \tag{3.5}$$

for Ω being a simply connected domain. The complex forms an exact sequence on Ω, i.e., the image of an operator in (3.5) is exactly the kernel of the subsequent operator. Among other consequences, this justifies the use of the magnetic vector potential in (2.7) [78, 138].

3.1.1 Magnetoquasistatic Formulation

Using the concept of weak derivatives, the weak formulation of (2.26) is obtained by multiplication with test functions $\mathbf{v}$, and integration over the domain Ω

$$\int_\Omega \nabla \times (\nu \nabla \times \mathbf{A}) \cdot \mathbf{v} \, \mathrm{d}\Omega + \int_\Omega \sigma \frac{\partial}{\partial t} \mathbf{A} \cdot \mathbf{v} \, \mathrm{d}\Omega = \int_\Omega (\mathbf{J}_{\text{src}} + \nabla \times \mathbf{M}) \cdot \mathbf{v} \, \mathrm{d}\Omega, \tag{3.6}$$

which must hold for all test functions $\mathbf{v} \in H(\text{curl}; \Omega)$. Using integration by parts, this can be written as the first order differential equation

$$\int_\Omega (\nu \nabla \times \mathbf{A}) \cdot (\nabla \times \mathbf{v}) \, \mathrm{d}\Omega - \int_{\partial\Omega} (\nu \nabla \times \mathbf{A}) \times \mathbf{n} \cdot \mathbf{v} \, \mathrm{d}\Gamma + \int_\Omega \sigma \frac{\partial}{\partial t} \mathbf{A} \cdot \mathbf{v} \, \mathrm{d}\Omega = \int_\Omega \mathbf{J}_{\text{src}} \cdot \mathbf{v} + \mathbf{M} \cdot (\nabla \times \mathbf{v}) \, \mathrm{d}\Omega, \tag{3.7}$$

where we assumed the magnetization $\mathbf{M}$ to vanish on $\partial\Omega$. For the machines relevant in this thesis we only consider the magnetostatic approximation (2.28), where the weak formulation can be derived analogously. With homogeneous Dirichlet and Neumann BCs, the problem then reads: Find $\mathbf{A} \in H_0(\text{curl}; \Omega)$, s.t.

$$\int_\Omega (\nu \nabla \times \mathbf{A}) \cdot (\nabla \times \mathbf{v}) \, \mathrm{d}\Omega = \int_\Omega \mathbf{J}_{\text{src}} \cdot \mathbf{v} + \mathbf{M} \cdot (\nabla \times \mathbf{v}) \, \mathrm{d}\Omega, \tag{3.8}$$

for all $\mathbf{v} \in H_0(\text{curl}; \Omega)$. The subscript in $H_0(\text{curl}; \Omega)$ indicates that the functions in this space fulfill the Dirichlet BCs. This subscript notation is employed in the following for all function spaces including Dirichlet BCs.

Similarly, for two-dimensional domains $\Omega \in \mathbb{R}^2$ the weak form of the magnetostatic problem (2.33) can be derived as the first-order differential equation

$$\int_\Omega \nu \nabla A \cdot \nabla v \, \mathrm{d}\Omega - \int_{\partial\Omega} (\nu \nabla A \cdot \mathbf{n}) \, v \, \mathrm{d}\Gamma = \int_\Omega J_{\text{src}} v + \mathbf{M}^\perp \cdot \nabla v \, \mathrm{d}\Omega, \tag{3.9}$$

with $A \in H^1(\Omega)$ and the test functions $v \in H^1(\Omega)$. Assuming homogeneous Neumann and Dirichlet BCs, we obtain the problem: Find $A \in H_0^1(\Omega)$, such that

$$\int_\Omega \nu \nabla A \cdot \nabla v \, \mathrm{d}\Omega = \int_\Omega J_{\text{src}} v + \mathbf{M}^\perp \cdot \nabla v \, \mathrm{d}\Omega, \tag{3.10}$$

for all $v \in H_0^1(\Omega)$, where $H_0^1(\Omega)$ fulfill the Dirichlet BC on Γ_{dir}. With a Lipschitz boundary $\partial\Omega$, it can be shown that there exists a unique solution of (3.10) using the Lax-Milgram Lemma [117, Theorem 3.14].

Note that in the following, we will use several notations for the inner product depending on the level of abstraction needed, e.g.,

$$\int_\Omega \nu \nabla A \cdot \nabla v \, \mathrm{d}\Omega = \langle \nu \nabla A, \nabla v \rangle_\Omega = a(A, v), \tag{3.11}$$

where $a(\star, \star)$ is usual notation for a bilinear form in mathematics, see e.g., [117, Chapter 2].

Discretization For the numerical discretization of the magnetostatic problem, we approximate the solution of the problem by a finite set of basis functions, i.e.,

$$\mathbf{A}(\mathbf{x}) \approx \mathbf{A}_h(\mathbf{x}) = \sum_{j=1}^{N_{\text{dof}}} u_j \mathbf{w}_j(\mathbf{x}), \tag{3.12}$$

where $\mathbf{w}_j(\mathbf{x}) \in V_h$ are vector valued basis functions which form the discrete function space $V_h \subset H(\text{curl}; \Omega)$ depending on the spatial coordinate $\mathbf{x}$, u_j are coefficients and N_{dof} is the number of basis functions. Using the Ritz-Galerkin approach, we choose to use the same functions for testing in (3.8) and as basis (3.12). This leads to the following linear system of equations: Find u_j for $j = 1, \dots, N_{\text{dof}}$, s.t.

$$\sum_{j=1}^{N_{\text{dof}}} u_j \int_\Omega \left(\nu \nabla \times \mathbf{w}_j\right) \cdot \left(\nabla \times \mathbf{v}_i\right) \, \mathrm{d}\Omega = \int_\Omega \mathbf{J}_{\text{src}} \cdot \mathbf{v}_i + \mathbf{M} \cdot \left(\nabla \times \mathbf{v}_i\right) \, \mathrm{d}\Omega, \tag{3.13}$$

for all $\mathbf{v}_i \in V_h$, $i = 1, \dots, N_{\text{dof}}$. The system of equations (3.13) can be written compactly in matrix form as

$$\mathbf{K}\mathbf{u} = \mathbf{f}, \tag{3.14}$$

where $\mathbf{K}$ is the stiffness matrix, $\mathbf{f}$ is the excitation vector, and $\mathbf{u}$ is the vector of unknowns, i.e., it contains the coefficients of (3.12). The entries of $\mathbf{K}$ and $\mathbf{f}$ are given by

$$(\mathbf{K})_{ij} = \int_\Omega \left(\nu \nabla \times \mathbf{w}_j\right) \cdot \left(\nabla \times \mathbf{v}_i\right) \, \mathrm{d}\Omega, \tag{3.15}$$

$$(\mathbf{f})_i = \int_\Omega \mathbf{J}_{\text{src}} \cdot \mathbf{v}_i + \mathbf{M} \cdot \left(\nabla \times \mathbf{v}_i\right) \, \mathrm{d}\Omega, \tag{3.16}$$

respectively. Note, that if the closed form solution of these integrals is not known, they are evaluated using numerical quadrature, e.g., Gaussian quadrature, see, e.g. [127, Chapter 6.8].

In the two-dimensional case, we can discretize the problem (3.10) by approximating the solution as

$$A(\mathbf{x}) \approx A_h(\mathbf{x}) = \sum_{j=1}^{N_{\text{dof}}} u_j w_j(\mathbf{x}), \tag{3.17}$$

where $w_j(\mathbf{x}) \in V_{h2D}$ are scalar valued basis functions form the discrete function space $V_{h2D} \subset H^1(\Omega)$ depending on the spatial coordinate $\mathbf{x}$, u_j are coefficients and N_{dof} is the number of basis functions. Analogously to the three-dimensional case, applying a Ritz-Galerkin approach, we use the same basis function space for the discrete test functions $v_i \in V_{h2D}$ as for the basis functions. This then leads to the discretized problem:

Find u_j for $j = 1, \dots, N_{\text{dof}}$, s.t.

$$\sum_{j=1}^{N_{\text{dof}}} u_j \int_\Omega \nu \nabla w_j \cdot \nabla v_i \, \mathrm{d}\Omega = \int_\Omega J_{\text{src}} v_i + \mathbf{M}^\perp \cdot \nabla v_i \, \mathrm{d}\Omega, \tag{3.18}$$

for all $v_i \in V_h$, $i = 1, \dots, N_{\text{dof}}$.

By writing (3.18) in matrix form, we obtain

$$\mathbf{K}_{2D}\mathbf{u}_{2D} = \mathbf{f}_{2D}, \tag{3.19}$$

with the entries

$$(\mathbf{K}_{2D})_{ij} = \int_\Omega \nu \nabla w_j \cdot \nabla v_i \,\mathrm{d}\Omega, \tag{3.20}$$

$$(\mathbf{f}_{2D})_i = \int_\Omega J_{\mathrm{src}} v_i + \mathbf{M}^\perp \cdot \nabla v_i \,\mathrm{d}\Omega, \tag{3.21}$$

for stiffness matrix $\mathbf{K}_{2D}$ and right-hand side $\mathbf{f}_{2D}$, respectively. The entries of the vector of unknowns $\mathbf{u}_{2D}$ are the coefficients of approximation (3.17). In the following, by slight abuse of notation, we will drop the index $2D$ for the two-dimensional domains, function spaces and matrices such that they coincide with the notation of the three-dimensional case. Note, that their definitions differ for two or three dimensions. Therefore, it is understood that we are referring to the appropriate definitions based on the dimensionality of the problem.

3.1.2 Electroquasistatic Formulation

Similar to the magnetoquasistatic formulation, we can obtain the weak formulation of the electroquasistatic problem (2.37) with homogeneous BCs as: Find $\Phi \in H_0^1(\Omega)$, such that

$$\int_\Omega \sigma \nabla \Phi \cdot \nabla v \,\mathrm{d}\Omega + \int_\Omega \frac{\partial}{\partial t} \varepsilon \nabla \Phi \cdot \nabla v \,\mathrm{d}\Omega = \int_\Omega \mathbf{J} \cdot \nabla v \,\mathrm{d}\Omega, \tag{3.22}$$

for all $v \in H_0^1(\Omega)$, where $H_0^1(\Omega)$ fulfill the Dirichlet BC on Γ_{dir}. In the static limit case, the weak form of the stationary current problem (2.40) is thus given as: Find $\Phi \in H_0^1(\Omega_{\mathrm{c}})$, such that

$$\int_{\Omega_{\mathrm{c}}} \sigma \nabla \Phi \cdot \nabla v \,\mathrm{d}\Omega = \int_{\Omega_{\mathrm{c}}} \mathbf{J} \cdot \nabla v \,\mathrm{d}\Omega, \tag{3.23}$$

for all $v \in H_0^1(\Omega_{\mathrm{c}})$.

Discretization As in the magneto(quasi)static case, we can approximate the solution of the problem (3.22) as a linear combination of a finite set of basis functions

$$\Phi(\mathbf{x}) \approx \Phi_h(\mathbf{x}) = \sum_{j=1}^{N_{\mathrm{dof}}} u_j w_j(\mathbf{x}), \tag{3.24}$$

where $w_j(\mathbf{x}) \in V_h$ are scalar valued basis functions form the discrete function space $V_h \subset H^1(\Omega)$ depending on the spatial coordinate $\mathbf{x}$, u_j are coefficients and N_{dof} is the number of basis functions. We apply a Ritz-Galerkin approach, where we use the same basis function space for the discrete test functions $v_i \in V_h$ as for the basis functions. This then leads to the discretized problem:

Find u_j for $j = 1, \dots, N_{\text{dof}}$, s.t.

$$\sum_{j=1}^{N_{\text{dof}}} u_j \int_\Omega \sigma \nabla w_j \cdot \nabla v_i \, \mathrm{d}\Omega + \frac{\mathrm{d}}{\mathrm{d}t} \sum_{j=1}^{N_{\text{dof}}} u_j \int_\Omega \varepsilon \nabla w_j \cdot \nabla v_i \, \mathrm{d}\Omega = \int_\Omega \mathbf{J} \cdot \nabla v \, \mathrm{d}\Omega, \tag{3.25}$$

for all $v_i \in V_h$, $i = 1, \dots, N_{\text{dof}}$.

By writing (3.25) in matrix form, we obtain

$$\mathbf{K}\mathbf{u} + \frac{\mathrm{d}}{\mathrm{d}t}\mathbf{M}\mathbf{u} = \mathbf{f}, \tag{3.26}$$

with the entries

$$(\mathbf{K})_{ij} = \int_\Omega \sigma \nabla w_j \cdot \nabla v_i \, \mathrm{d}\Omega, \tag{3.27}$$

$$(\mathbf{M})_{ij} = \int_\Omega \varepsilon \nabla w_j \cdot \nabla v_i \, \mathrm{d}\Omega, \tag{3.28}$$

$$(\mathbf{f})_i = \int_\Omega \mathbf{J} \cdot \nabla v_i \, \mathrm{d}\Omega, \tag{3.29}$$

for stiffness matrix $\mathbf{K}$, mass matrix $\mathbf{M}$ and right-hand side $\mathbf{f}$, respectively. The entries of the vector of unknowns $\mathbf{u}$ are the coefficients of approximation (3.24). In the static limit the problem reduces to

$$\mathbf{K}\mathbf{u} + \frac{\mathrm{d}}{\mathrm{d}t}\mathbf{M}\mathbf{u} = \mathbf{f}, \tag{3.30}$$

in the conducting domain Ω_{c}. Note, that the problem can be solved on the whole domain, treated as an electroquasistatic problem if an appropriate stabilization is employed, see, e.g. [10].

3.2 Isogeometric Analysis

IGA was introduced in 2005 by Hughes et. al [88] as a method for the discretization and numerical solution of PDEs. In contrast to the classical FEM, which commonly uses unstructured triangular/quadrilateral meshes in 2D or tetrahedral/hexahedral meshes in 3D, IGA uses the same functions used in computer aided design (CAD) software for the representation of the geometry, namely B-splines and non-uniform rational B-splines (NURBS), based on a cartesian reference mesh. This alleviates the need for meshing geometries which are usually already given by their CAD representation. In particular, conic sections, e.g., circles and ellipses, can be represented exactly by NURBS while conventional meshes, even when (polynomially) curved elements are used, introduce a geometry approximation error. This error can be avoided even on the coarsest refinement levels when using IGA for the numerical solution of PDEs. To arrive at an IGA discretization, we will first introduce the required functions, i.e., B-splines and NURBS following [45], where we focus first on the geometry representation and then on the discretization of electromagnetic fields.

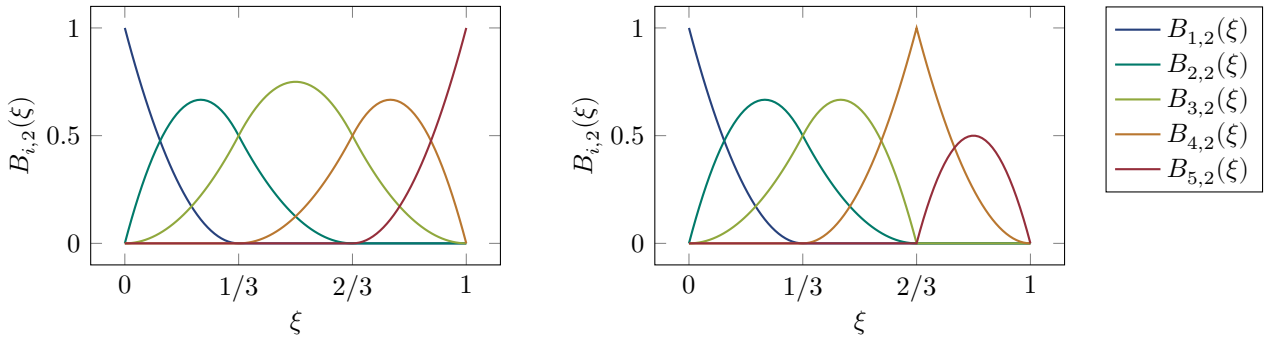

(a) $\Xi = \{0, 0, 0, 1/3, 2/3, 1, 1, 1\}$ **(b)** $\Xi = \{0, 0, 0, 1/3, 2/3, 2/3, 1, 1, 1\}$

Figure 3.1: B-spline basis functions of degree $p = 2$ for open knot vectors.

3.2.1 B-Splines and NURBS Basis Functions

B-splines are piecewise polynomial functions which are defined by their degree p and a *knot vector* $\Xi = \{\xi_1, \xi_2, \dots, \xi_{n+p+1}\}$ where the knots $\xi_j \in [0, 1]$ for all $j \in \{1, \dots, n+p+1\}$ are coordinates in the parametric space, where n is the dimension of the space. The B-spline basis functions are defined by the Cox-de Boor recursion formula [126], where the i-th basis function of degree p is given by

$$\hat{B}_i^p(\xi) = \frac{\xi - \xi_i}{\xi_{i+p} - \xi_i} \hat{B}_i^{p-1}(\xi) + \frac{\xi_{i+p+1} - \xi}{\xi_{i+p+1} - \xi_{i+1}} \hat{B}_{i+1}^{p-1}(\xi), \tag{3.31}$$

for all $p \geq 1$ and for $p = 0$ via

$$\hat{B}_i^0(\xi) = \begin{cases} 1 & \text{if } \xi_i \leq \xi < \xi_{i+1}, \\ 0 & \text{else,} \end{cases} \tag{3.32}$$

where $0/0 = 0$ is formally assumed. The space spanned by these B-spline basis functions is denoted by $S_p(\Xi)$. B-spline basis functions have local support ranging over $p+1$ knot spans and are C^∞ smooth except at the knots, where their smoothness is reduced to $p - m$, where m is the multiplicity of the respective knot. Thus, a multiplicity of $m = p$ results in a kink in the basis functions, see Fig. 3.1. We will mainly use open knot vectors, i.e., the first and last knot has a multiplicity of $m = p+1$. This makes the B-splines interpolatory at the ends of the knot spans which will be an important property when considering IGA later. The B-spline basis functions also fulfill the partition of unity property

$$\sum_{i=1}^{n} \hat{B}_i^p(\xi) = 1 \tag{3.33}$$

for $\xi \in [\xi_1, \xi_{n+p+1}]$. Furthermore, it can easily be shown that the derivative of a B-spline is also a B-spline given by differentiating the basis functions yielding

$$\frac{\mathrm{d}}{\mathrm{d}\xi} \hat{B}_i^p(\xi) = \frac{p}{\xi_{i+p} - \xi_i} \hat{B}_i^{p-1}(\xi). \tag{3.34}$$

Using the B-spline basis functions, NURBS basis functions are defined by

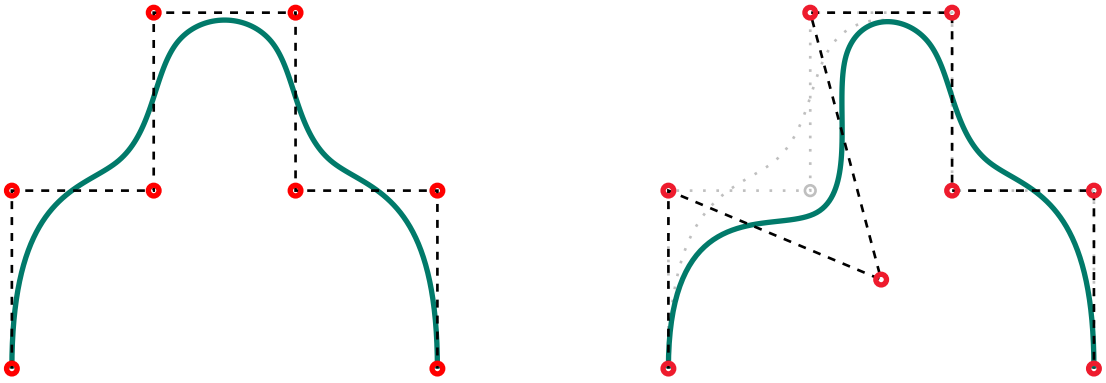

(a) Original NURBS curve.

(b) Modified NURBS curve where one control point is changed.

Figure 3.2: Visualization of the modification of the shape of a NURBS curve by moving one control point. Taken from [114] ©2021 IEEE.

$$\hat{N}_i^p(\xi) = \frac{w_i \hat{B}_i^p(\xi)}{\sum_{k=1}^n w_k \hat{B}_k^p(\xi)}, \tag{3.35}$$

where $w_k > 0$ for all $k = 1, 2, \dots, n$ are so-called *weights*. B-splines can be considered as a special case of NURBS where all weights are $w_i = 1$. However, the derivative of a NURBS is is not a NURBS as it is the case for B-splines, see (3.34).

3.2.2 Representation of the Geometry

One of the first steps in the simulation of real-world problems is having a discretization of the problem geometry. In IGA we use B-splines and NURBS for the geometry description. When the geometry is represented via a volumetric NURBS parametrization, the physical domain Ω is defined as a smooth mapping $\mathbf{F}$ from the reference domain $\hat{\Omega}$ such that

$$\mathbf{F} : \hat{\Omega} \to \Omega, \tag{3.36}$$

where the reference domain in d dimensions is given by $\hat{\Omega} = [0, 1]^d$ which is the unit square or unit cube in 2D or 3D, respectively, and the physical domain in the n-dimensional space $\Omega \subset \mathbb{R}^n$.

NURBS curves can be defined by the NURBS basis functions and control points $\mathbf{P}_i$ as

$$\mathbf{C}(\xi) = \sum_{i=1}^{n} \mathbf{P}_i \hat{N}_i^p(\xi). \tag{3.37}$$

Note that this can be written analogously for B-splines. The NURBS have been popular in CAD since the local support of the basis functions allows for a local modification of the curve by moving control points as visualized in Fig. 3.2. This is a very simple way of locally manipulating B-spline/NURBS geometries, making it also very convenient for shape optimization, see Chapter 5. Using a tensor product

construction, we extend the definition of curves (3.37) to NURBS surfaces $\mathbf{S}(\xi,\eta)$ and volumes $\mathbf{V}(\xi,\eta,\zeta)$ as

$$\mathbf{S}(\xi,\eta) = \sum_{i=1}^{n}\sum_{j=1}^{m} \mathbf{P}_{i,j}\hat{N}_i^p(\xi)\hat{M}_j^q(\eta), \tag{3.38}$$

and

$$\mathbf{V}(\xi,\eta,\zeta) = \sum_{i=1}^{n}\sum_{j=1}^{m}\sum_{k=1}^{l} \mathbf{P}_{i,j,k}\hat{N}_i^p(\xi)\hat{M}_j^q(\eta)\hat{L}_k^r(\zeta), \tag{3.39}$$

with the control grid $\mathbf{P}_{i,j,k}$, the knot vectors $\Xi = \left\{\xi_1, \xi_2, \dots, \xi_{n+p+1}\right\}$, $\mathrm{H} = \left\{\eta_1, \eta_2, \dots, \eta_{m+q+1}\right\}$ and $\mathrm{Z} = \left\{\zeta_1, \zeta_2, \dots, \zeta_{l+r+1}\right\}$ defining the NURBS basis functions $\hat{N}_i^p$, $\hat{M}_j^q$, and $\hat{L}_k^r$ of degree p, q, and r, respectively. Using a more compact notation, multivariate B-spline basis functions in d dimensions, where we typically consider $d = 2$ or $d = 3$, i.e., from the domain $[0,1]^d$, can be defined by the tensor-products of univariate B-splines as

$$\hat{B}_{\mathbf{i}}^{\mathbf{p}}(\boldsymbol{\xi}) = \hat{B}_{i_1}^{p_1}(\xi_1) \dots \hat{B}_{i_d}^{p_d}(\xi_d), \tag{3.40}$$

where $\xi_1, \dots, \xi_d$ denote the parametric variables in each direction, $\mathbf{p} = (p_1, \dots, p_d)$ is the degree vector and $\mathbf{i} = (i_1, \dots, i_d)$ the multivariate index. These splines span the multivariate spline space

$$S_{\mathbf{p}}(\Xi_1, \dots, \Xi_d) = S_{p_1,\dots,p_d}(\Xi_1, \dots, \Xi_d) = S_{p_1}(\Xi_1) \otimes \dots \otimes S_{p_d}(\Xi_d). \tag{3.41}$$

Analogously, multivariate NURBS basis functions are given by

$$\hat{N}_{\mathbf{i}}^{\mathbf{p}}(\boldsymbol{\xi}) = \hat{N}_{i_1}^{p_1}(\xi_1) \dots \hat{N}_{i_d}^{p_d}(\xi_d). \tag{3.42}$$

Unifying this notation, any d-dimensional NURBS geometry can be described by the mapping

$$\mathbf{F}(\boldsymbol{\xi}) = \sum_{\mathbf{i}} \mathbf{P}_{\mathbf{i}}\hat{N}_{\mathbf{i}}^{\mathbf{p}}(\boldsymbol{\xi}), \quad \boldsymbol{\xi} \in [0,1]^d, \tag{3.43}$$

where we chose $\left[\xi_1, \xi_{n+p+1}\right] = [0,1]$ as parameter space interval for the knots in all parametric directions. Note, that a d-dimensional geometry might exist within a higher-dimensional space $\mathbb{R}^n$ depending on the dimension of the control points $\mathbf{P}_\star \in \mathbb{R}^n$, e.g., a surface ($d = 2$) may be embedded in $\mathbb{R}^3$.

Refinement When refining geometries, it is important to correctly deal with control points and knot multiplicities in order to preserve the original geometry including its regularity. There are different refinement methods to enrich the B-spline basis which guarantee that these properties are preserved:

Knot insertion: When refining the B-spline basis via knot insertion (also called h-refinement), a knot $\bar{\xi}$ is inserted in the knot vector Ξ. This leads to an increased number of basis functions, thus, enlarging the discrete space. When refining a B-spline or NURBS geometry, e.g., a curve, naturally, the number of control points also needs to be increased. The new control points can be constructed as a linear combination of the old control points. For more information, see, e.g., [45]. Inserting a knot will lower the continuity at that knot. However, this can be compensated for the curve by appropriately constructing the new control points.

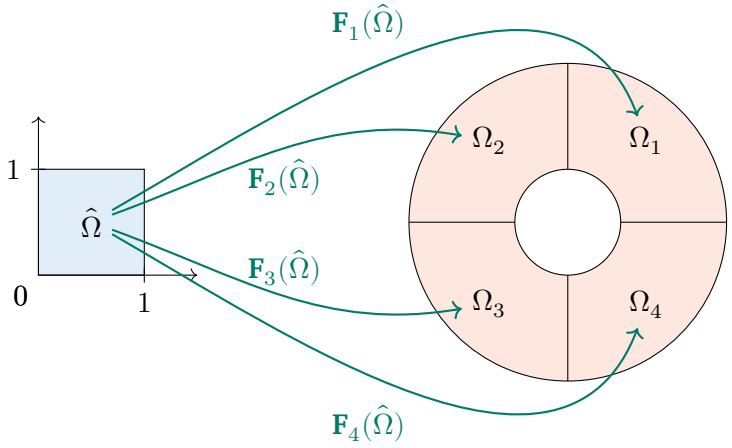

Figure 3.3: Visualization of the mappings $\mathbf{F}_k$ from the reference domain $\hat{\Omega}$ to the patches Ω_k of a multi-patch geometry. Taken from [114] ©2021 IEEE.

Degree elevation: Of course, the B-spline basis can also be enriched by elevating the degree. Degree elevation is similar to p-refinement in the classical FEM. However, while p-refinement always starts from a basis of C^0 regularity at all element borders, degree elevation in IGA allows to deal with any combination of regularities. As degree elevation also elevates the continuity at the knots, in order to obtain a new basis with the same regularity as the old one, the multiplicity of each knot has to be increased, such that $p - m_i$ are maintained at all element boundaries. This is necessary when elevating the degree of a NURBS geometry, such that, e.g., kinks in the geometry are preserved. When only interested in the enrichment of the basis function space when dealing with basis functions of highest possible regularity, naturally, it is not necessary to increase the multiplicity of the knots.

k-refinement: A unique way of refinement for B-splines and NURBS is the so called k-refinement. It allows for a higher degree with higher regularity. It uses a combination of degree elevation and knot insertion and allows for a more flexible refinement than it is possible for the basis functions in the classical FEM. This is achieved by elevating the degree first and then inserting new knots. In contrast to first inserting new knots and afterwards elevating the degree, this leads to a higher regularity as the multiplicity of the new knot is not increased during the degree elevation. For more details, see, e.g., [45].

Often, problem geometries cannot be described as a single regular mapping in the form (3.36) from the reference to the physical domain, e.g., when the topology of the physical domain is different from that of the reference domain, or it is inconvenient because there are different materials present in the domain. In this case a multi-patch model can be used, where each patch is described by a regular transformation $\mathbf{F}_k$ from the reference domain $\hat{\Omega}$ to the patches Ω_k as illustrated in Fig. 3.3. In the following we will assume that the domain Ω is defined by a (patchwise) NURBS mapping as given in (3.43).

3.2.3 Representation of the Solution

Similar to the classical FEM, in IGA the weak formulation, e.g. (3.8), is used to obtain an approximative solution of the problem. Again, the Ritz-Galerkin approach is used where the basis functions of the solution and the test functions are chosen to be the same. In the case of IGA, the basis is chosen as a B-spline basis in contrast to the classical FEM where piecewise polynomial basis functions with global C^0 continuity are typically used. The B-splines are defined on the reference domain $\hat{\Omega} = [0,1]^d$ and are transformed using push-forwards to obtain the basis functions on the physical domain Ω. In order for the de Rham sequence to be fulfilled in both the reference and physical domain, the operators acting on the transformed functions of the respective function spaces need to be consistent. For this, we need gradient-preserving, curl-preserving and divergence-preserving transformations. Following [117], for the mapping (3.36) the transformation of functions from the function spaces of (3.5) are given by the push-forwards

$$\varphi^0(\hat{u}) = u \circ \mathbf{F} = \hat{u} \qquad \hat{u} \in H^1(\hat{\Omega}) \tag{3.44}$$

$$\varphi^1(\hat{\mathbf{u}}) = \mathbf{u} \circ \mathbf{F} = (\mathrm{d}\mathbf{F})^{-\top}\hat{\mathbf{u}} \qquad \hat{\mathbf{u}} \in H\left(\mathrm{curl}; \hat{\Omega}\right) \tag{3.45}$$

$$\varphi^2(\hat{\mathbf{u}}) = \mathbf{u} \circ \mathbf{F} = \frac{1}{\det(\mathrm{d}\mathbf{F})}\mathrm{d}\mathbf{F}\,\hat{\mathbf{u}} \qquad \hat{\mathbf{u}} \in H\left(\mathrm{div}; \hat{\Omega}\right) \tag{3.46}$$

$$\varphi^3(\hat{u}) = u \circ \mathbf{F} = \frac{1}{\det(\mathrm{d}\mathbf{F})}\hat{u} \qquad \hat{u} \in L^2(\hat{\Omega}) \tag{3.47}$$

where $\mathrm{d}\mathbf{F}$ is the Jacobian of the geometry mapping $\mathbf{F}$ and the hat $\hat{\star}$ always indicates the association to the reference domain, e.g., $\hat{u} \in H^1(\hat{\Omega})$ is defined on the reference domain $\hat{\Omega}$.

The discretization of the magnetostatic problem is then carried out as explained in Section 3.1.1 and Section 3.1.1, where as discrete function spaces for the basis and test functions, we use B-spline function spaces, which are explained in more detail in the following Section 3.2.4.

3.2.4 B-spline Function Spaces for Magnetostatics

When discretizing Maxwell's equations it is necessary to choose the discrete function spaces, such that they also fulfill the discrete De Rham sequence (3.5). For B-splines, appropriate B-spline spaces have been introduced in [35, 36], fulfilling the discrete de Rham sequence

$$S^0_{\mathbf{p}}(\Omega) \xrightarrow{\nabla} S^1_{\mathbf{p}}(\Omega) \xrightarrow{\nabla\times} S^2_{\mathbf{p}}(\Omega) \xrightarrow{\nabla\cdot} S^3_{\mathbf{p}}(\Omega), \tag{3.48}$$

where the spaces in the parametric domain $\hat{\Omega}$ are given by

$$S^0_{\mathbf{p}}\left(\hat{\Omega}\right) = S_{p_1,p_2,p_3}\left(\Xi_1, \Xi_2, \Xi_3\right), \tag{3.49}$$

$$S^1_{\mathbf{p}}\left(\hat{\Omega}\right) = S_{p_1-1,p_2,p_3}\left(\Xi'_1, \Xi_2, \Xi_3\right) \times S_{p_1,p_2-1,p_3}\left(\Xi_1, \Xi'_2, \Xi_3\right) \times S_{p_1,p_2,p_3-1}\left(\Xi_1, \Xi_2, \Xi'_3\right), \tag{3.50}$$

$$S^2_{\mathbf{p}}\left(\hat{\Omega}\right) = S_{p_1,p_2-1,p_3-1}\left(\Xi_1, \Xi'_2, \Xi'_3\right) \times S_{p_1-1,p_2,p_3-1}\left(\Xi'_1, \Xi_2, \Xi'_3\right) \times S_{p_1-1,p_2-1,p_3}\left(\Xi'_1, \Xi'_2, \Xi_3\right), \tag{3.51}$$

$$S^3_{\mathbf{p}}\left(\hat{\Omega}\right) = S_{p_1-1,p_2-1,p_3-1}\left(\Xi'_1, \Xi'_2, \Xi'_3\right), \tag{3.52}$$

with the knot vectors Ξ_1, Ξ_2 and Ξ_3 and the reduced knot vectors Ξ'_1, Ξ'_2 and Ξ'_3, where the first and last knot are removed. The discrete de Rham sequence (3.48) with the B-spline spaces (3.49)–(3.52)

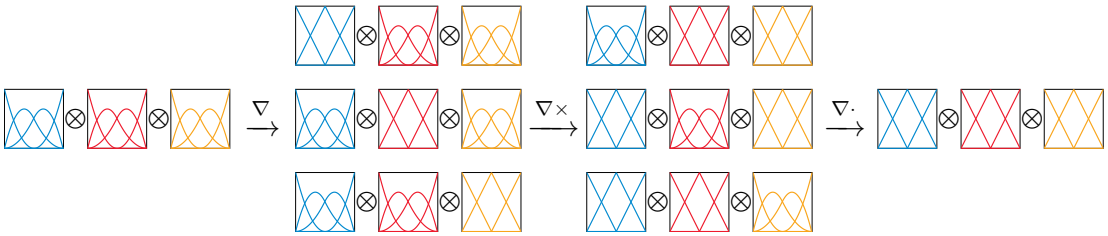

Figure 3.4: Visualization of the discrete de Rham sequence (3.48) with the B-spline spaces of (3.49)–(3.52) for $p = (2, 2, 2)$.

is visualized in Fig. 3.4. The spaces in the physical domain Ω are obtained by using the push-forwards (3.44)–(3.47), e.g.,

$$S^0_{\mathbf{p}}(\Omega) = \left\{ u = \varphi^0(\hat{u}), \quad \hat{u} \in S^0_{\mathbf{p}}(\hat{\Omega}) \right\}, \tag{3.53}$$

and similarly for the other spaces. Analogously to the classical Nédélec basis [117], the basis functions in $S^0_{\mathbf{p}}$ are associated to the control points or vertices of the control mesh while functions in $S^1_{\mathbf{p}}$ are associated to edges, functions in $S^2_{\mathbf{p}}$ to facets and functions in $S^3_{\mathbf{p}}$ to cells of the control mesh [95].

In the following, for simplicity of notation, we will assume the same degree in all parametric directions, i.e., $p = p_1 = p_2 = p_3$ and therefore will adopt the notation $S^\star_p := S^\star_{\mathbf{p}}$.

Trace spaces When setting boundary or interface conditions according to Section 2.1.3, we require the traces of the field quantities at the interface. Let us define the traces of a scalar function f or a vector function $\mathbf{f}$ on a part of the boundary $\Gamma \subset \partial\Omega$ by the trace operators

$$\gamma^0_\Gamma(f) = f, \tag{3.54}$$
$$\gamma^1_\Gamma(\mathbf{f}) = (\mathbf{n} \times \mathbf{f}) \times \mathbf{n}, \tag{3.55}$$
$$\gamma^{1^*}_\Gamma(\mathbf{f}) = \mathbf{f} \times \mathbf{n}, \tag{3.56}$$
$$\gamma^2_\Gamma(\mathbf{f}) = \mathbf{f} \cdot \mathbf{n} \tag{3.57}$$

where γ^0 is the scalar trace operator, γ^1 is the tangential trace operator, γ^{1^*} is the rotated tangential trace operator and γ^2 is the normal trace operator [117]. The spline-based fields on the boundary Γ are then in the trace spaces [33, 95]

$$\gamma^0_\Gamma\left(S^0_p(\Omega)\right) = S^0_p(\Gamma), \tag{3.58}$$
$$\gamma^1_\Gamma\left(S^1_p(\Omega)\right) = S^1_p(\Gamma), \tag{3.59}$$
$$\gamma^{1^*}_\Gamma\left(S^1_p(\Omega)\right) = S^{1^*}_p(\Gamma), \tag{3.60}$$
$$\gamma^2_\Gamma\left(S^2_p(\Omega)\right) = S^2_p(\Gamma). \tag{3.61}$$

With these spaces we can define the trace sequences

$$S_p^0(\Gamma) \xrightarrow{\nabla} S_p^1(\Gamma) \xrightarrow{\nabla\times} S_p^2(\Gamma),$$

$$S_p^0(\Gamma) \xrightarrow{\nabla^\perp} S_p^{1^*}(\Gamma) \xrightarrow{\nabla\cdot} S_p^2(\Gamma).$$

Here, $S_p^1(\Gamma)$ and $S_p^{1^*}(\Gamma)$ are curl-conforming and divergence-conforming spline spaces, respectively. They are defined by appropriate push-forwards from the spaces in the reference domain $\hat{\Gamma}$ which are given by

$$S_p^1(\hat{\Gamma}) = S_{p-1,p}(\Xi'_k, \Xi_l) \times S_{p,p-1}(\Xi_k, \Xi'_l), \tag{3.62}$$

$$S_p^{1^*}(\hat{\Gamma}) = S_{p,p-1}(\Xi_k, \Xi'_l) \times S_{p-1,p}(\Xi'_k, \Xi_l), \tag{3.63}$$

where the indices $l, k \in \{1, 2, 3\}$ of the knot vectors depend on which boundary of the parametric domain we are considering.

In the special case of vanishing trace on a part $\Sigma \subset \Gamma_{\text{dir}}$ of the boundary, we obtain the sequence

$$S_p^0(\Omega; \Sigma) \xrightarrow{\nabla} S_p^1(\Omega; \Sigma) \xrightarrow{\nabla\times} S_p^2(\Omega; \Sigma) \xrightarrow{\nabla\cdot} S_p^3(\Omega; \Sigma),$$

where in particular, the curl-conforming space is given by

$$S_p^1(\Omega; \Sigma) = \{\mathbf{u} \in S_p^1(\Omega) : \gamma_\Gamma^1(\mathbf{u}) = \mathbf{0} \text{ on } \Sigma\},$$

and the other spaces are given analogously.

3.3 Domain Decomposition Methods for Non-Conforming Meshes

When simulating rotating structures like electric motors it is necessary to find a method to treat rotation efficiently. Most methods like the classical FEM and also IGA use conforming meshes for the computation of the solution. Thus, when rotating a part of the computational domain using a naive implementation, we have to create a new mesh for each rotation angle. As up to $75\,\%$ of the simulation time is spent on modeling, geometry decomposition and mesh generation [20], this is not an efficient solution. Several methods have been proposed to deal with rotating geometries. These methods commonly involve dividing the geometry into a stationary part (stator) and a rotating part (rotor) and creating the mesh on those subdomains separately. Such methods include for example the moving band method, where a moving band is placed between the domains and only the discretization of this band has to be recalculated [46], sliding surface methods based on Lagrange multipliers [50, 134] or locked-step methods which only allow for certain rotation angles. In the following, based on [63, 64, 95], we want to investigate a particular class of methods for the simulation of geometries with non-conforming discretizations, namely the Lagrange multiplier based mortaring method [130] and a Nitsche-type coupling method [5, 136].

3.3.1 Mortaring

Let us consider a computational domain which is divided into two subdomains $\overline{\Omega} = \overline{\Omega}_1 \cup \overline{\Omega}_2$. Note that from now on, by abuse of notation, we will denote the subdomains by Ω_1 and Ω_2, which might each consist of multiple patches. The subscript now refers to the subdomain instead of the patches. Using the mortar method, which can be interpreted as a special case of the three-field method [130], we can couple them at their common interface $\Gamma_{\text{int}} = \partial\Omega_1 \cap \partial\Omega_2$, where $\partial\Omega_\star$ denotes the boundary of $\Omega_\star$. In the following, subscripts, i.e.,

$$f_i \coloneqq f|_{\Omega_i} \tag{3.64}$$

with $i \in \{1, 2\}$, will denote the restriction of a function f to the subdomain Ω_i

On the interface Γ_{int} the solution of (3.8) needs to fulfill the interface conditions

$$\mathbf{n}_\Gamma \times \mathbf{A}_1 = \mathbf{n}_\Gamma \times \mathbf{A}_2, \qquad \text{on } \Gamma_{\text{int}} \tag{3.65}$$

$$(\nu\nabla \times \mathbf{A}_1) \times \mathbf{n}_\Gamma = (\nu\nabla \times \mathbf{A}_2) \times \mathbf{n}_\Gamma \qquad \text{on } \Gamma_{\text{int}}, \tag{3.66}$$

with the normal vector $\mathbf{n}_\Gamma$ on the interface pointing from Ω_1 to Ω_2. These interface conditions correspond to the normal continuity of the magnetic flux density (2.16) and the tangential continuity of the magnetic field (2.14). The interface condition (3.66) allows us to introduce the Lagrange multiplier

$$\boldsymbol{\lambda} \coloneqq (\nu\nabla \times \mathbf{A}) \times \mathbf{n}_\Gamma \qquad \text{on } \Gamma_{\text{int}} \tag{3.67}$$

on both subdomains, i.e., $\partial\Omega_1 \cap \Gamma_{\text{int}}$ and $\partial\Omega_2 \cap \Gamma_{\text{int}}$. It can easily be verified that the Lagrange multiplier corresponds to the rotated tangential magnetic field on the interface Γ_{int}. Inserting the Lagrange multiplier and homogeneous Dirichlet and Neumann BCs in (3.8) yields a decomposed problem: Find $\mathbf{A}_1 \in V_1, \mathbf{A}_2 \in V_2, \boldsymbol{\lambda} \in M$, such that

$$\int_{\Omega_1} \nu(\nabla \times \mathbf{A}_1) \cdot (\nabla \times \mathbf{v}_1)\,\mathrm{d}\Omega - \int_{\Gamma_{\text{int}}} \boldsymbol{\lambda} \cdot \mathbf{v}_1\,\mathrm{d}\Gamma = \int_\Omega \mathbf{J}_{\text{src}} \cdot \mathbf{v}_1 + \mathbf{M} \cdot (\nabla \times \mathbf{v}_1)\,\mathrm{d}\Omega, \tag{3.68}$$

$$\int_{\Omega_2} \nu(\nabla \times \mathbf{A}_2) \cdot (\nabla \times \mathbf{v}_2)\,\mathrm{d}\Omega + \int_{\Gamma_{\text{int}}} \boldsymbol{\lambda} \cdot \mathbf{v}_2\,\mathrm{d}\Gamma = \int_\Omega \mathbf{J}_{\text{src}} \cdot \mathbf{v}_2 + \mathbf{M} \cdot (\nabla \times \mathbf{v}_2)\,\mathrm{d}\Omega, \tag{3.69}$$

$$\int_{\Gamma_{\text{int}}} (\mathbf{A}_2 - \mathbf{A}_1) \cdot \boldsymbol{\mu}\,\mathrm{d}\Gamma = 0, \tag{3.70}$$

for all $\mathbf{v}_1 \in V_1, \mathbf{v}_2 \in V_2, \boldsymbol{\mu} \in M$, with the spaces $V_1, V_2 \subset H(\text{curl}; \Omega)$ which satisfy Dirichlet BCs on Γ_{dir}, and the Lagrange multiplier space $M = \{(\nabla \times \mathbf{v}) \times \mathbf{n}_\Gamma : \mathbf{v} \in V_1\}$. Here, (3.70) enforces the tangential continuity of the magnetic vector potential in a weak sense. Note, that this method can be easily extended for more than two subdomains. For simplicity, and as we only require two-subdomains we will only consider this case.

The discretization of this problem using (3.12) for both stator and rotor domain and the discrete approximation of the Lagrange multipliers

$$\boldsymbol{\lambda}(\mathbf{x}) \approx \boldsymbol{\lambda}_h(\mathbf{x}) = \sum_{j=1}^{N} \lambda_j \boldsymbol{\eta}_j(\mathbf{x}), \tag{3.71}$$

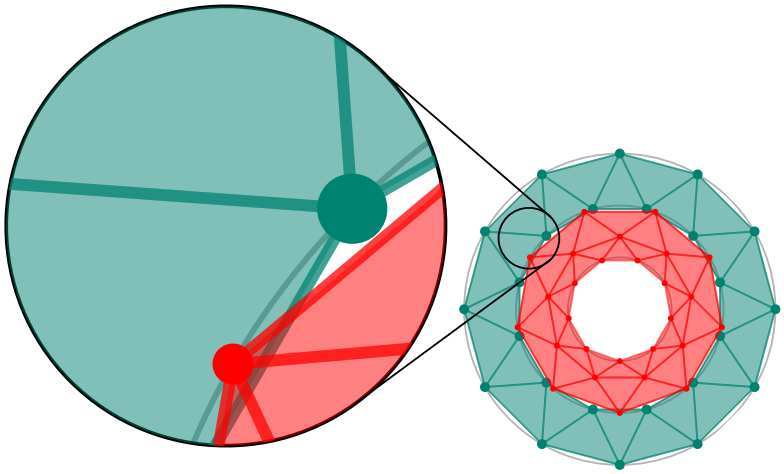

Figure 3.5: Non-matching discretizations of stator and rotor at the interface Γ_{int} when using conventional finite elements. Taken from [95].

with the discrete basis functions $\boldsymbol{\eta}_j \in M_h$ and coefficients λ_j, leads to the saddle-point problem

$$\begin{bmatrix} \mathbf{K}_1 & \mathbf{0} & -\mathbf{G}_1 \\ \mathbf{0} & \mathbf{K}_2 & \mathbf{G}_2 \\ -\mathbf{G}_1^\top & \mathbf{G}_2^\top & \mathbf{0} \end{bmatrix} \begin{bmatrix} \mathbf{u}_1 \\ \mathbf{u}_2 \\ \boldsymbol{\lambda} \end{bmatrix} = \begin{bmatrix} \mathbf{f}_1 \\ \mathbf{f}_2 \\ \mathbf{0} \end{bmatrix}, \tag{3.72}$$

where $\mathbf{K}_\star$, $\mathbf{f}_\star$ and $\mathbf{u}_\star$ are the domain-wise stiffness matrices (3.15), excitation (3.15) and degrees of freedom of the subdomains, respectively, $\boldsymbol{\lambda}$ is the vector of Lagrange multiplier coefficients, and $\mathbf{G}_\star$ are the coupling matrices with the entries

$$(\mathbf{G}_\star)_{ij} = \int_{\Gamma_{\text{int}}} \boldsymbol{\eta}_j \cdot \mathbf{v}_{\star i} \, \mathrm{d}\Gamma_{\text{int}}. \tag{3.73}$$

This saddle-point problem becomes unstable when the discrete inf-sup or Ladyzhenskaya–Babuška–Brezzi (LBB) condition [9, 28, 30] is not fulfilled. To guarantee stability, the discrete space of the Lagrange multiplier needs to be chosen adequately.

Realization of Rotation When using classical finite elements (FE), the geometry is approximated using a mesh with piecewise polynomial elements. For geometries with non-conforming meshes, the elements at the interface Γ_{int} might overlap and have gaps as visualized in Fig. 3.5, such that the evaluation of the interface integrals in (3.68)–(3.70) becomes cumbersome as projections on a suitable surface have to be employed before the actual evaluation of the integrals. This problem remains even for curved elements as they are not able to represent circles exactly. Using IGA resolves this problem as the geometries of the subdomains can be represented exactly, such that the integrals can be evaluated directly on Γ_{int}.

We assume that the interface $\Gamma_{\text{int}} = \partial\Omega_1 \cap \partial\Omega_2$ is a cylinder that is centered around the z-axis of our global coordinate system. On each subdomain we assume a coordinate system that is fixed to the domain, i.e., rotated with the domain. This way, if the rotor Ω_2 is rotated by an angle α, any point $\tilde{\mathbf{x}}$

in the rotated rotor coordinate system can be expressed in terms of the fixed global coordinate system by

$$\tilde{\mathbf{x}} = \rho_{-\alpha}(\mathbf{x}), \tag{3.74}$$

where $\mathbf{x}$ is the point in the fixed coordinate system and the transformation ρ_α describes a rotation of a point by an angle α around the z-axis, see Fig. 3.6. Following [24, 50, 64] we define the Lagrange multipliers on the stationary global coordinate system which coincides with the one of the stator. For both, stator and rotor (2.28) holds in their respective coordinate systems, such that the material distribution stays fixed under rotation. In practice, this allows us to model construct the discretizations for rotor and stator separately and to compute the interface integrals in (3.68)–(3.70) by numerical quadrature, evaluating the functions in their respective coordinate system, taking the transformation (3.74) into account.

3.3.1.1 Isogeometric Mortaring

As described earlier, the mortar method results in a saddle-point problem that becomes unstable when the discrete space of Lagrange multipliers is chosen too large. When using IGA for the discretization of the magnetic vector potential in (3.68)–(3.70), where each subdomain is described by a NURBS-mapping, appropriate choices for the Lagrange multiplier space have been introduced by Buffa et al. [32]. Following [32], we build the discrete Lagrange multiplier space M_h on the subdomain Ω_1. As M_h will constrain the functions in Ω_1, we will call Ω_1 the dependent (also called slave in the literature) subdomain, whereas Ω_2 will be called the independent (also called master in the literature) subdomain. The multiplier space is then constructed as a divergence-conforming space in the interface with reduced degree compared to the curl-conforming space of degree p in the dependent subdomain as

$$M_h = S^{1^*}_{p-1}(\Gamma_{\text{int}}). \tag{3.75}$$

Here, we used the reduced degree by one to obtain a space of degree $p-1$. Note, that it is also possible to reduce the degree by any odd number s, to obtain a space of degree $p-s$. It has been proven in [32] that using this space yields a stable mortar formulation in the sense that the inf-sup stability condition [9, 28, 30]

$$\sup_{\mathbf{u}\in\gamma^1_{\Gamma_{\text{int}}}(S^1_p(\Omega_1;\Sigma_1))} \frac{\int_{\Gamma_{\text{int}}} \mathbf{u}\cdot\mathbf{v}\,\mathrm{d}\Gamma}{\parallel \mathbf{u} \parallel_{-1/2,\mathbf{curl}}} \geq \beta \parallel \mathbf{v} \parallel_{-1/2,\text{div}} \qquad \text{for all } \mathbf{v}\in S^{1^*}_{p-1}(\Gamma_{\text{int}}) \tag{3.76}$$

is fulfilled. We obtain the discrete isogeometric mortar formulation: Find $\mathbf{A}_{1,h}\in V_{h,1}=S^1_{p_1}(\Omega_1)$, $\mathbf{A}_{2,h}\in V_{h,2}=S^1_{p_2}(\Omega_2)$ and $\boldsymbol{\lambda}_h\in M_h=S^{1^*}_{p_1-1}(\Gamma_{\text{int}})$, such that

$$\int_{\Omega_1}\nu(\nabla\times\mathbf{A}_{1,h})\cdot(\nabla\times\mathbf{v}_{1,h})\,\mathrm{d}\Omega-\int_{\Gamma_{\text{int}}}\boldsymbol{\lambda}_h\cdot\mathbf{v}_{1,h}\,\mathrm{d}\Gamma=\int_{\Omega}\mathbf{J}_{\text{src}}\cdot\mathbf{v}_{1,h}+\mathbf{M}\cdot\left(\nabla\times\mathbf{v}_{1,h}\right)\,\mathrm{d}\Omega, \tag{3.77}$$

$$\int_{\Omega_2}\nu(\nabla\times\mathbf{A}_{2,h})\cdot(\nabla\times\mathbf{v}_{2,h})\,\mathrm{d}\Omega+\int_{\Gamma_{\text{int}}}\boldsymbol{\lambda}_h\cdot\mathbf{v}_{2,h}\,\mathrm{d}\Gamma=\int_{\Omega}\mathbf{J}_{\text{src}}\cdot\mathbf{v}_{2,h}+\mathbf{M}\cdot\left(\nabla\times\mathbf{v}_{2,h}\right)\,\mathrm{d}\Omega, \tag{3.78}$$

$$\int_{\Gamma_{\text{int}}}(\mathbf{A}_{2,h}-\mathbf{A}_{1,h})\cdot\boldsymbol{\mu}_h\,\mathrm{d}\Gamma=0, \tag{3.79}$$

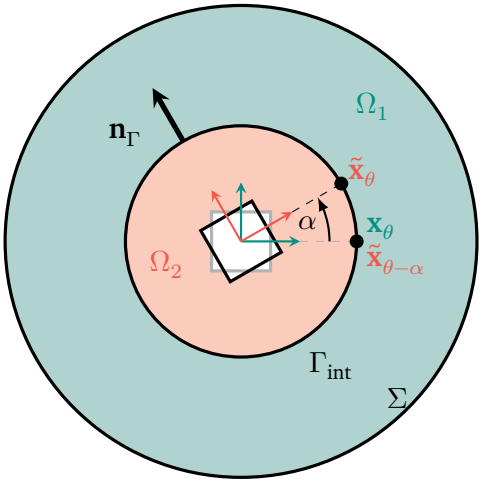

Figure 3.6: Sketch of the geometry. We denote by $\mathbf{x}_\theta$ a point in the fixed coordinate system (red) of the stator domain Ω_1 and by $\tilde{\mathbf{x}}_\theta$ a point given in terms of the rotated coordinate system (green) of the rotor domian Ω_2. In both cases we stress the azimuthal component in the respective coordinate system by writing it as a subscript. The are related by $\mathbf{x}_\theta = \tilde{\mathbf{x}}_{\theta-\alpha} = \rho_{-\alpha}(\mathbf{x})$ where α is the angle of rotation. Adapted from [63].

for all $\mathbf{v}_{1,h} \in V_{h,1}, \mathbf{v}_{2,h} \in V_{h,2}, \boldsymbol{\mu}_h \in M_h$. Note, that by abuse of notation, here we use p_1 and p_2 as the degree of the basis functions in each direction for domain Ω_1 and Ω_2, respectively.

3.3.1.2 Harmonic Coupling

In the two-dimensional case, the mortaring formulation can be obtained similarly. However, we can exploit several consequences of the simplification, see Fig. 3.6. The interface conditions in the 2D case in terms of the global coordinate system are then given by

$$A_1 = A_2 \circ \rho_{-\alpha}, \qquad \text{on } \Gamma_{\text{int}} \tag{3.80}$$

$$\nu \nabla A_1 \cdot \mathbf{n}_\Gamma = \nu \nabla A_2 \circ \rho_{-\alpha} \cdot \mathbf{n}_\Gamma, \qquad \text{on } \Gamma_{\text{int}} \tag{3.81}$$

$$\tag{3.82}$$

where $f \circ g(x) = f(g(x))$ denotes the concatenation of functions. Analogously to the three-dimensional case, (3.81) allows us to introduce the Lagrange multiplier

$$\lambda := \nu \nabla A \cdot \mathbf{n}_\Gamma \qquad \text{on } \Gamma_{\text{int}} \tag{3.83}$$

on the interface of both subdomains $\partial\Omega_1 \cap \Gamma_{\text{int}}$ and $\partial\Omega_2 \cap \Gamma_{\text{int}}$. Again, we can see that the Lagrange multiplier corresponds to the tangential magnetic field at the interface, which in the two-dimensional case with a circular interface is the angular component of the magnetic field. We obtain the problem: Find $A_1 \in V_1, A_2 \in V_2, \lambda \in M$, such that

$$\int_{\Omega_1} \nu \nabla A_1 \cdot \nabla \mathbf{v}_1 \, \mathrm{d}\Omega - \int_{\Gamma_{\text{int}}} \lambda \, \mathbf{v}_1 \, \mathrm{d}\Gamma_{\text{int}} = \int_\Omega J_{\text{src}} v_1 + \mathbf{M}^\perp \cdot \nabla v_1 \, \mathrm{d}\Omega, \tag{3.84}$$

$$\int_{\Omega_2} \nu \nabla A_2 \cdot \nabla \mathbf{v}_2 \,\mathrm{d}\Omega + \int_{\Gamma_{\text{int}}} \lambda \,\mathbf{v}_2 \,\mathrm{d}\Gamma_{\text{int}} = \int_{\Omega} J_{\text{src}} v_2 + \mathbf{M}^{\perp} \cdot \nabla v_2 \,\mathrm{d}\Omega, \tag{3.85}$$

$$\int_{\Gamma_{\text{int}}} (A_2 - A_1)\mu \,\mathrm{d}\Gamma = 0, \tag{3.86}$$

for all $\mathbf{v}_1 \in V_1, \mathbf{v}_2 \in V_2, \boldsymbol{\mu} \in M$, with the spaces $V_1, V_2 \subset H^1(\Omega)$ which satisfy Dirichlet BCs on $\partial\Omega \cap \Gamma_{\text{dir}}$, and the Lagrange multiplier space M.

As in the 3D case, we can discretize the system using the discrete functions introduced in (3.17) from the discrete function spaces $V_{h,1}$ and $V_{h,2}$ and the discretization of the Lagrange multipliers

$$\lambda(\mathbf{x}) \approx \lambda_h(\mathbf{x}) = \sum_{j=1}^{N} \lambda_j \eta_j(\mathbf{x}), \tag{3.87}$$

with the discrete basis functions $\eta_j \in M_h$ and coefficients λ_j. This leads to the system

$$\begin{bmatrix} \mathbf{K}_1 & \mathbf{0} & -\mathbf{G}_1 \\ \mathbf{0} & \mathbf{K}_2 & \mathbf{G}_2 \\ -\mathbf{G}_1^{\top} & \mathbf{G}_2^{\top} & \mathbf{0} \end{bmatrix} \begin{bmatrix} \mathbf{u}_1 \\ \mathbf{u}_2 \\ \boldsymbol{\lambda} \end{bmatrix} = \begin{bmatrix} \mathbf{f}_1 \\ \mathbf{f}_2 \\ \mathbf{0} \end{bmatrix}, \tag{3.88}$$

analogously to (3.72), but with the matrix entries (3.20) and (3.21) for the stiffness matrices and excitation vectors, respectively, and the coupling matrix entries

$$(\mathbf{G}_\star)_{ij} = \int_{\Gamma_{\text{int}}} \eta_j v_{\star i} \,\mathrm{d}\Gamma_{\text{int}}. \tag{3.89}$$

Different choices can be made for the space M_h, e.g., modified trace spaces at the boundary, see, e.g. [15, 164]. In [164], Wohlmuth introduced a dual space with local support for classical FE. Appropriate dual multiplier spaces for B-splines have been introduced and proven to be inf-sup stable in [31]. For electric motors which have a periodic structure and where subdomains are rotated by an angle α, harmonic functions are a natural choice of basis functions for the Lagrange multiplier in the two-dimensional case. Therefore, as an approximation of the Lagrange multipliers, we consider the discrete space

$$M_N := \left\{ \mu_N(\theta) = \frac{\mathcal{A}_0}{2} + \sum\nolimits_{n=1}^{N} \mathcal{A}_n \cos(n\theta) + \mathcal{B}_n \sin(n\theta) : \mathcal{A}_n, \mathcal{B}_n \in \mathbb{R} \right\} \tag{3.90}$$

of trigonometric polynomials of degree $\leq N$. As the integral over the interface Γ_{int} corresponds to an integration over the angle, the entries of the coupling matrices can then be written depending on the rotation angle α as

$$\begin{aligned} [\mathbf{G}_2(\alpha)]_{i,2n} &= \int_{\Gamma_{\text{int}}} \cos(n\theta)\, w_i \circ \rho_{-\alpha} r_\Gamma d\theta, \qquad n \geq 0, \\ [\mathbf{G}_2(\alpha)]_{i,2n-1} &= \int_{\Gamma_{\text{int}}} \sin(n\theta)\, w_i \circ \rho_{-\alpha} r_\Gamma d\theta, \qquad n \geq 1, \end{aligned} \tag{3.91}$$

where w_i are the basis functions for the Galerkin approximation on Ω_2. Using trigonometric summation formulas, this can be expressed in terms of the coupling matrix entries for angle $\alpha = 0$. The entries for the rotated subdomain Ω_2 can then be written as

$$\begin{aligned}[\mathbf{G}_2(\alpha)]_{i,2n} &= \cos(n\alpha)[\mathbf{G}_2(0)]_{i,2n} - \sin(n\alpha)[\mathbf{G}_2(0)]_{i,2n-1} \\ [\mathbf{G}_2(\alpha)]_{i,2n-1} &= \sin(n\alpha)[\mathbf{G}_2(0)]_{i,2n} + \cos(n\alpha)[\mathbf{G}_2(0)]_{i,2n-1}.\end{aligned} \tag{3.92}$$

This allows us to evaluate the integrals in the coupling matrix $\mathbf{G}_2(\alpha)$ only for a single angle $\alpha = 0$ and write

$$\mathbf{G}_2(\alpha) = \mathbf{G}_2(0)\mathbf{R}(\alpha) \tag{3.93}$$

where $\mathbf{R}(\alpha)$ is a block diagonal matrix with 2×2 blocks which are given in closed form such that no integral evaluation is needed.

Note, that the Lagrange multipliers can also be expressed as complex exponentials using Euler's formula. This leads to a diagonal rotation matrix which has been investigated in [24]. Further, note that closed form solutions exist for Fourier transformations of B-splines, i.e., products of trigonometric functions with B-splines [120]. Therefore, for B-spline basis functions w_i in (3.89) the entries of the coupling matrix $\mathbf{G}_\star$ can be computed very efficiently analytically, see Section 8.1.

Reduction to Interface Problem using a Schur Complement Based on [63], we can reformulate the system as an interface problem. Assuming the stiffness matrices $\mathbf{K}_1$ and $\mathbf{K}_2$ are non-singular due to Dirichlet BCs, we can rewrite system (3.88) as

$$\begin{bmatrix} \mathbf{I} & \mathbf{0} & -\mathbf{K}_1^{-1}\mathbf{G}_1 \\ \mathbf{0} & \mathbf{I} & \mathbf{K}_2^{-1}\mathbf{G}_2\mathbf{R}(\alpha) \\ -\mathbf{G}_1^\top & \mathbf{R}^\top(\alpha)\mathbf{G}_2^\top & \mathbf{0} \end{bmatrix} \begin{bmatrix} \mathbf{u}_1 \\ \mathbf{u}_2 \\ \boldsymbol{\lambda} \end{bmatrix} = \begin{bmatrix} \mathbf{K}_1^{-1}\mathbf{f}_1 \\ \mathbf{K}_2^{-1}\mathbf{f}_2 \\ \mathbf{0} \end{bmatrix}, \tag{3.94}$$

where $\mathbf{I}$ and $\mathbf{0}$ are identity and zero matrices of appropriate size and we write $\mathbf{G}_2 = \mathbf{G}_2(0)$ for the coupling matrix $\mathbf{G}_2$ evaluated without any angular displacement of the rotor. Using a Schur complement, the internal degrees of freedom can be eliminated, giving rise to the low-dimensional interface problem

$$\mathbf{K}_{\text{int}}(\alpha)\boldsymbol{\lambda} = \mathbf{f}_{\text{int}}(\alpha) \tag{3.95}$$

with

$$\mathbf{K}_{\text{int}}(\alpha) = \mathbf{G}_1^\top\mathbf{K}_1^{-1}\mathbf{G}_1 + \mathbf{R}^\top(\alpha)\mathbf{G}_2^\top\mathbf{K}_2^{-1}\mathbf{G}_2\mathbf{R}(\alpha), \tag{3.96}$$

$$\mathbf{f}_{\text{int}}(\alpha) = -\mathbf{G}_1^\top\mathbf{K}_1^{-1}\mathbf{f}_1 + \mathbf{R}^\top(\alpha)\mathbf{G}_2^\top\mathbf{K}_2^{-1}\mathbf{f}_2. \tag{3.97}$$

where the inverses of the stiffness matrices $\mathbf{K}_*^{-1}$ are not needed explicitly. Instead, we can use a factorization and a few forward/backward substitutions to precompute the necessary expressions, e.g., $\mathbf{K}_*^{-1}\mathbf{G}_*$, which are independent of the rotation angle α. Thus, only the smaller interface system (3.95) with the low-dimensional matrix $\mathbf{K}_{\text{int}} \in \mathbb{R}^{N\times N}$ has to be solved in the online phase for different rotation angles. This drastically reduces the computational effort when dealing with rotation.

The internal degrees of freedom can be cheaply reconstructed, i.e.,

$$\mathbf{u}_1 = \mathbf{K}_1^{-1}\mathbf{f}_1 + \mathbf{K}_1^{-1}\mathbf{G}_1\boldsymbol{\lambda}, \tag{3.98}$$

$$\mathbf{u}_2 = \mathbf{K}_2^{-1}\mathbf{f}_2 - \mathbf{K}_2^{-1}\mathbf{G}_2\mathbf{R}(\alpha)\boldsymbol{\lambda}. \tag{3.99}$$

Additionally, since only the rotation matrix $\mathbf{R}(\alpha)$ depends on α, the assembly of the matrices and vectors $\mathbf{K}_\star$, $\mathbf{G}_\star$ and $\mathbf{f}_\star$ only has to be performed once, as they are independent of the rotation angle. Only the rotation 2×2-block matrix $\mathbf{R}$ has to be updated for each rotation angle, which is computationally cheap as it is given in closed form. In the case of non-linear material relations, the stiffness matrices $\mathbf{K}_\star$ (3.20) depend on the magnetic field, such that the inverses cannot be precomputed. However, the Schur complement formulation can still be helpful, e.g., in the context of preconditioners or model order reduction [140, 143].

3.3.2 Nitsche-Type Coupling

The Nitsche method was originally proposed to solve boundary value problems, imposing Dirichlet BCs in a weak sense [121]. Weakly imposed boundary conditions based on the Nitsche method have been used in the context of isogeometric analysis, e.g., in [13, 66] for mechanical and fluid dynamics problems. The Nitsche-type coupling method was then also applied to couple subdomains by penalizing the jump of the quantities across the interface. Like the mortar method, it can be used to overcome difficulties when the mesh of the two subdomains is not matching at the interface. It has been applied to isogeometric analysis using nodal basis functions, e.g., for the elasticity problem [5, 100]. For Maxwell's equations, in particular for eddy current problems, the Nitsche method has been used for the classical FEM with Nédélec elements in [136]. While in the classical mortar method, Lagrange multipliers are introduced, in the Nitsche coupling method, this is not necessary such that the number of degrees of freedom (DoFs) is not increased.

To solve problem (3.8) on the domain Ω which is decomposed into the non-overlapping subdomains Ω_1 and Ω_2 with $\overline{\Omega} = \overline{\Omega}_1 \cup \overline{\Omega}_2$ and interface $\Gamma_{\text{int}} = \partial\Omega_1 \cap \partial\Omega_2$, we need to enforce the interface conditions (3.65) and (3.66). Using the Nitsche method, the discretized weak formulation of the coupled problem is obtained as:

Find $\mathbf{A}_h \in V_h \subset H_0(\text{curl}; \Omega)$

$$\begin{aligned}
&\sum_{i=1}^{2}\left(\int_{\Omega_i} \nu\nabla\times\mathbf{A}_h\cdot\nabla\times\mathbf{v}\,\mathrm{d}\Omega\right) - \int_{\Gamma_{\text{int}}} \left\{\nabla\times\mathbf{A}_h\times\mathbf{n}_\Gamma\right\}_\nu \cdot [\mathbf{v}]_{\Gamma_{\text{int}}}\,\mathrm{d}\Gamma_{\text{int}} \\
&\quad + \varepsilon\int_{\Gamma_{\text{int}}} \left\{\nabla\times\mathbf{v}\times\mathbf{n}_\Gamma\right\}_\nu \cdot [\mathbf{A}_h]_{\Gamma_{\text{int}}}\,\mathrm{d}\Gamma_{\text{int}} + \gamma\int_{\Gamma_{\text{int}}} \frac{\bar{\nu}p}{h}\,[\mathbf{A}_h\times\mathbf{n}_\Gamma]_{\Gamma_{\text{int}}}\cdot[\mathbf{v}\times\mathbf{n}_\Gamma]_{\Gamma_{\text{int}}}\,\mathrm{d}\Gamma_{\text{int}} \\
&\quad = \sum_{i=1}^{2}\int_{\Omega_i}\mathbf{J}\cdot\mathbf{v}\,\mathrm{d}\Omega
\end{aligned} \tag{3.100}$$

for all $\mathbf{v} \in V_h$, where $\mathbf{A}_h$ is the numerical approximation of the magnetic vector potential (3.12), $\mathbf{v}$ are test functions, V_h is a discrete function space including Dirichlet BCs and $\mathbf{n}_\Gamma$ is the normal vector of Γ_{int}. Here, the second term is the consistency term, ensuring that the interface condition (3.66) holds in an averaged sense. The third term is the symmetry term, where by choosing $\varepsilon = -1$ we obtain a symmetric interior penalty Galerkin formulation. The fourth term is the penalty term which penalizes the jump of

the tangential components of the magnetic vector potential across the interface, thus enforcing interface condition (3.65). Here, $\bar{\nu}$ is the average reluctivity, p and h are the polynomial degree and characteristic element size, respectively, and γ is the penalty or Nitsche factor. In this formulation, $[\star]_{\Gamma_{\text{int}}}$ denotes the jump across the interface Γ_{int} and $\{\star\}_{\nu}$ denotes the average, i.e.,

$$[\mathbf{w}]_{\Gamma_{\text{int}}} = \mathbf{w}_1(\mathbf{x}) - \mathbf{w}_2(\mathbf{x}), \tag{3.101}$$

$$\{\mathbf{w}\}_{\nu} = \frac{1}{\nu_1 + \nu_2} \left(\nu_1 \mathbf{w}_1(\mathbf{x}) + \nu_2 \mathbf{w}_2(\mathbf{x})\right), \tag{3.102}$$

for any quantity $\mathbf{w}$, where the subscript indicates whether the quantity belongs to Ω_1 or Ω_2, and $\mathbf{x} \in \Gamma_{\text{int}}$ is the spatial coordinate.

3.4 Tree-Cotree Gauging

As mentioned before, the magnetic vector potential is not uniquely defined in the magnetostatic formulation, such that a gauging is necessary to obtain a unique solution. The simplest form of gauging is the Coulomb gauge [78, Section 10.1] which sets

$$\nabla \cdot \mathbf{A} = 0. \tag{3.103}$$

Another choice for gauging time-dependent problems in an $\mathbf{A}$-Φ formulation is the Lorenz gauge [78, Section 10.1], given by

$$\nabla \cdot \mathbf{A} = -\mu\varepsilon \frac{\partial \Phi}{\partial t}. \tag{3.104}$$

Note, that we are applying a divergence operator to the magnetic vector potential here. Formally, there should be a material property present, e.g., $\nabla \cdot \varepsilon\mathbf{A}$ such that the divergence is applied to a function from $H(\text{div}; \Omega)$ and not to $\mathbf{A} \in H(\text{curl}; \Omega)$. However, this property was chosen to be constant, such that it can be omitted here for better readability. There are several ways to incorporate gauging in the discrete system. The Coulomb gauge can be enforced, e.g., using a mixed formulation or via a projector given in [40]. Iterative systems can also be used to find a solution of the system without explicitly setting the gauging condition [144]. Other methods of regularization include assuming a small virtual conductivity everywhere in the domain, such that a regular mass matrix is added to the system [41]. As gauging method to recover a unique solution of our discrete problem based on graph-theory, following [95], we introduce the tree-cotree gauging which was originally proposed for lowest order edge elements by Albanese and Rubinacci in [1]. Multiple formulations for tree-cotree gauging have been proposed and are summarized in [119].

Simply Connected Domains First, we will assume that the domain Ω and its boundary $\partial\Omega$ are simply connected. Albanese and Rubinacci showed in [1] that when using classical Nédélec edge elements, setting the DoFs belonging to the tree-edges of a spanning tree in a mesh graph to zero in (3.14) results in a reduced

system of full rank. Denoting the set of all edges in the mesh by E, the tree edges by T and the cotree-edges by $C = E \setminus T$, the system (3.14) can be decomposed into the system

$$\begin{bmatrix} \mathbf{K}_{CC} & \mathbf{K}_{CT} \\ \mathbf{K}_{TC} & \mathbf{K}_{TT} \end{bmatrix} \begin{bmatrix} \mathbf{a}_C \\ \mathbf{a}_T \end{bmatrix} = \begin{bmatrix} \mathbf{f}_C \\ \mathbf{f}_T \end{bmatrix}, \tag{3.105}$$

where the indices of the matrix/vector blocks indicate their affiliation to the tree/cotree. By setting the tree-DoFs $\mathbf{a}_C = \mathbf{0}$, we obtain the reduced system

$$\mathbf{K}_{CC}\mathbf{a}_C = \mathbf{f}_C. \tag{3.106}$$

This is due to the one-to-one correspondence of the DoFs to the edges of the mesh. In the lowest order case, this can be understood from the physical interpretation of the DoFs belonging to line integrals of vector fields. An intuition why removing the tree-DoFs results in a full-rank system is the following. The kernel of the curl-operator is the space of gradient fields $\mathbf{g} = \nabla\psi$. These can be defined by a potential ψ which is associated to the vertices of the mesh and connected by the edges. Therefore, a gradient field defined on the edges of the spanning tree defines the potential ψ on all vertices up to a constant, since the spanning tree connects all vertices. Thus, the DoFs of the whole gradient field $\mathbf{g}$ are defined by the tree-DoFs. Since we know that any gradient field can be added to our solution, due to it being in the kernel of the curl-operator, it is clear that we can prescribe any arbitrary gradient field on the tree-edges. So setting these DoFs to zero and thus reducing the system, yields a full-rank system with a unique solution.

It can easily be seen, that there are multiple ways to build the tree, resulting in different systems with different condition numbers [89] and different solutions for the DoFs. They are all valid, provided that they treat Dirichlet BCs correctly. When strongly imposing the Dirichlet BC on Γ_{dir} one simple way to deal with this is to start building the tree on the Dirichlet boundary Γ_{dir} and afterwards growing it into the interior of the domain [61]. This can be interpreted as collapsing all Dirichlet DoFs into a single vertex as all edges on Γ_{dir} are removed from the system. Starting to grow the tree on Γ_{dir} or collapsing all Dirichlet DoFs to one node ensures that no loops are formed by multiple interior tree edges touching Γ_{dir}. The procedure can be summarized in the following way [95]:

Algorithm 1 ***Tree-Cotree Decomposition***

1. *Build a spanning tree on the subgraph associated to* Γ_{dir}.
2. *Proceed growing the tree on the subgraph associated to* Γ_{neu}.
3. *Grow the tree on the remaining graph in the interior of* Ω.

As we assumed the Dirichlet boundary Γ_{dir} and the domain Ω to be connected and simply connected, we can use a simple breadth-first search (BFS) algorithm to find the spanning tree.

Multiply Connected Domains As explained in Section 3.4, the spanning tree can be used to filter out the functions with a vanishing curl when the discrete kernel of the curl-operator is exactly the space of gradient fields. However, in multiply connected domains the kernel also includes the harmonic fields explained in Section 2.2. The dimension of the space of these fields is equal to the number of closed curves that are not the boundary of any surface in the domain, i.e., the rank of the first cohomology group [118]. In this case, the tree does not suffice to span the whole kernel of the curl-operator. To capture the full kernel, we have

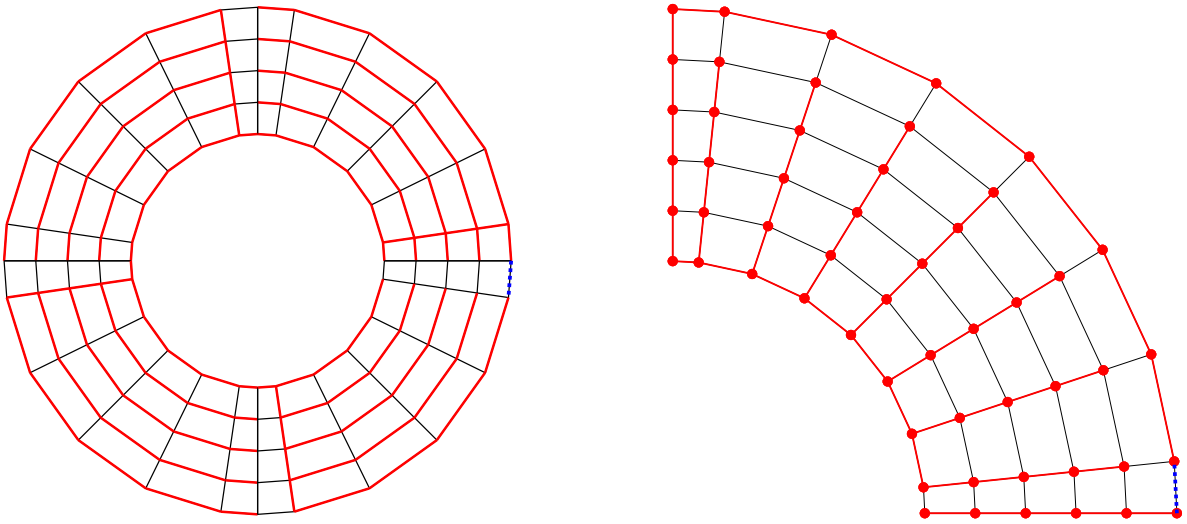

(a) Enrichment of the tree for gauging for an annulus.

(b) Enrichment of the tree for periodic conditions.

Figure 3.7: Example of the construction of a tree for non-trivial domain topologies. It is not sufficient to use a spanning tree (red) for gauging. To gauge correctly, an edge has to be added to the tree, for example the edged dotted in blue. Taken from [95].

to add specific edges to the tree. As an example, this is visualized for an annulus in Fig. 3.7a. When using periodic BCs for a domain in the shape of an annulus segment, this topologically corresponds to a whole annulus and therefore has to be treated the same as an annulus. An example for the enrichment of the tree to capture the whole kernel of the domain is shown in Fig. 3.7b. Here, the periodic boundary sides are identified as one single one, which means that they are topologically connected, creating a nontrivial domain topologically equivalent to the annulus.

To create an enriched tree that is sufficient for gauging also taking into account the topology of the domain, we require an algorithm to automatically compute the cohomology [56, 107]. While many algorithms have been considered prohibitively expensive, recently, the novel concept of lazy cohomology generators was introduced [57]. These cohomology generators are purely graph theoretic and have been shown to have a linear average complexity, leading to a significant speedup compared to other algorithms. An open source implementation for the computation of cohomology generators for discretized domains is available, see [55, 93].

3.5 Summary

In this chapter, we gave a brief review of the fundamentals of numerical analysis. These concepts form the basis for the simulation of electric machines. We introduced the weak formulations of the magneto(quasi)static problem and of the electroquasistatic problem in both two and three dimensions. The process of discretization was outlined, where the obtained weak formulation was discretized by approximating the continuous functions as a linear combination of discrete basis functions. As a special case of

discretization, isogeometric analysis (IGA) was introduced. To understand IGA, the functions classically used in computer aided design (CAD) are necessary. The definitions of these basis functions, i.e., B-splines and non-uniform rational B-splines (NURBS) were given. The representation of geometries using these CAD functions was explained and the possibilities of geometry manipulation are pointed out. The mappings from the reference domain were formally introduced, including the concept of multi-patch domains. The appropriate function spaces for Maxwell's equations were defined. We also introduce their discrete B-spline counterparts. Using these concepts, we can apply IGA for simulating electromagnetic problems. However, classical IGA requires a conforming patch discretization of the geometry. The creation of conforming patches is cumbersome when considering moving domains, such as rotating machines. To address this problem, we discussed methods for the coupling of non-conforming geometries, including the mortar method, harmonic mortaring and the Nitsche coupling method. Furthermore, the three-dimensional magnetostatic problem using a magnetic vector potential approach is not uniquely solvable. As a gauging method, the tree-cotree decomposition and its treatment of non-contractible domains (i.e., harmonic fields) is discussed.

This chapter equips us with the basic tools we require for the simulation of magnetic fields in electric machines.

4 Numerical Analysis and Simulation

For multiobjective design optimization of electric motors and generators, simulation is essential. To facilitate this process, efficient methods for discretizing and solving the magneto(quasi)static problem (2.28)–(2.30) or (2.33)–(2.35) are necessary. For this purpose, we can employ IGA as explained in Section 3.2. This approach is particularly convenient, due to its capability to exactly represent the cylindrical structure of rotating machines. IGA has been applied for the simulation of electric machines, e.g., in [24, 68]. For the simulation of rotating electric machines, techniques such as isogeometric mortaring [32], harmonic mortaring [24, 50] or the Nitsche coupling method are promising approaches. These coupling techniques allow for an independent modeling of the subsystems, i.e., stator and rotor. In this chapter we propose a modification of the B-spline Lagrange multiplier space introduced in [32] to allow for a correct gauging of the discrete problem. In addition, we propose a stability condition for the selection of the Lagrange multipliers in harmonic mortaring.

To gauge the three-dimensional magnetostatic problem, one can utilize a tree-cotree decomposition. This technique was initially introduced in the finite element domain in [1] and has led to several variants, see [26, Section 5.3] and the overview article [119] and the references therein. Initially, only lowest order discretizations were explored, simplifying the identification of degrees of freedoms with tree edges. However, [165, Section 6.3] discusses how the same concept can be applied to the lowest-order subspace of a hierarchical higher-order FE space. Further exploration of a more general tree-cotree decomposition for conventional higher-order FE on tetrahedra is discussed in [135]. In this chapter, we explain how the tree-cotree gauging can be applied to IGA and derive the correct tree construction for the case of mortaring.

This chapter presents new methodologies, expands on existing ones and further investigates the numerical methods that are especially well suited for the simulation of electric machines, outlined in the previous chapter. We also establish how to combine these methods for the simulation of electric machines, including necessary modifications. Moreover, we propose a method for simulating electric machines including the windings. This method does not require the air surrounding the windings to be resolved as a conforming multi-patch discretization.

4.1 Analysis of Mortar Formulations

The mortar method has been employed for standard FE discretizations in magnetostatics [27] and in particular for the coupling of non-conforming rotor and stator domains in electric machines, e.g., in [157]. Stator and rotor are separated by an air gap. For our purpose, we will assume that the interface is placed within the air gap, such that both stator and rotor domain include parts of the air gap as it is commonly realized, see, e.g., [4, 24]. It has been applied to isogeometric discretizations in [31, 32]. In this section, we will propose a modification to the B-spline Lagrange multiplier space proposed in [32]

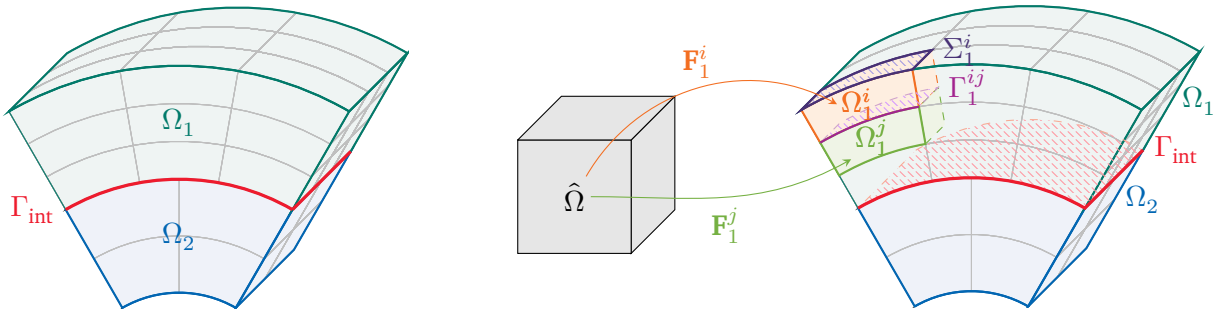

(a) Sketch of subdomains.

(b) Sketch of subdomains and two exemplary patches Ω_1^i and Ω_1^j.

Figure 4.1: Sketch of two non-conforming subdomains Ω_1 and Ω_2 which are coupled at the common interface Γ_{int}. The subdomains each consist of multi-patch discretizations which are conforming within the respective subdomains. The subdomains are shown in green and blue while the boundaries of the patches are shown in gray. In Fig. 4.1b, two exemplary patches are labeled.

to enable correct gauging of the discretized problem. For the case of two-dimensional machine models, we apply harmonic mortaring as presented in Section 3.3.1.2. Harmonic mortaring, which has been proposed for the simulation of rotating electric machines in [24, 50] is investigated in terms of stability, focusing on an appropriate choice for the Lagrange multiplier space and a stability condition is derived.

4.1.1 Isogeometric Mortaring for Multi-Patch Domains

The function space for the Lagrange multiplier for the isogeometric mortar problem introduced in [32] has been shown to result in a stable and spurious-free formulation. However, in the case of multi-patch subdomains, the discrete kernel of the system does not exactly coincide with the gradients of a suitable discrete space. Therefore, for gauging the system correctly, a modification of the discrete Lagrange multiplier space is necessary. Following [95], we derive the necessary modification of the discrete B-spline multiplier space. We assume both subdomains to be conforming multi-patch geometries. Thus, mortaring is only applied to couple the subdomains, which are allowed to be non-conforming across the interface Γ_{int}. A sketch of such a domain is visualized in Fig. 4.1a.

Lagrange Multiplier Space Let us assume that we have a multi-patch representation of both domains. This means both domains $\Omega_k = \cup_{i=1}^{N_k} \Omega_k^i$ for $k = 1, 2$ are given by N_k patches Ω_k^i which are represented by the parametrizations $\mathbf{F}_k^i$. The patches are non-overlapping and conforming. They are connected by the interfaces $\Gamma_k^{ij} = \partial\Omega_k^i \cap \partial\Omega_k^j$, for $i, j = 1, \dots, N_k$ which are either empty or the image of one complete side of the reference domain $\hat{\Omega}$ of the mappings $\mathbf{F}_k^i$. To impose BCs, we denote the boundaries by $\Sigma_k^i = \partial\Omega_k^i \cap \partial\Omega$. To illustrate this notation, a sketch of a domain consisting of two subdomains is shown in Fig. 4.1b, where the notation is demonstrated for two exemplary patches in Ω_1. Similarly to the definitions in the single patch case, we define the discrete curl-conforming spaces on the multi-patch subdomains with vanishing tangential trace on the boundary $\partial\Omega$ as

$$V_{k,h} = \{\mathbf{u} \in H(\text{curl}; \Omega_k) : \mathbf{u}|_{\Omega_k^i} \in S_p^1(\Omega_k^i; \Sigma_k^i) \text{ for } i = 1, \dots, N_k\},$$

where inside the subdomains, patches are glued together by a one-to-one identification of the tangential trace functions of coincident control mesh edges at patch interfaces. Note that the tangential trace only vanishes on the domain boundary and not on the subdomain interface Γ_{int}. For the space of the Lagrange multipliers we assume for simplicity that each patch Ω_1^i in the dependent subdomain Ω_1 only has one side on the interface Γ_{int} that we will denote by Γ^i. We define the Lagrange multiplier space as

$$M_h = \{\boldsymbol{\mu} \in (L^2(\Gamma_{\text{int}}))^3 : \boldsymbol{\mu} \in S_{p-1}^{1^*}(\Gamma^i) \text{ for } i = 1, \dots, N_1\}, \tag{4.1}$$

where, in contrast to the functions of V_h, the functions in M_h are not glued together at the patch interfaces. Using these spaces, the mortar formulation is the same as (3.77)–(3.79). The Lagrange multiplier space (4.1) for isogeometric mortaring was introduced in [32] and yields a stable formulation and spurious mode-free solution of the Maxwell eigenvalue problem (2.21). However, we will see in the following that when we want to apply a gauging method, this space is not suitable because the discrete kernel of the curl-operator does not exactly coincide with the gradient of a suitable discrete space.

Modification of the Lagrange Multiplier Space For analyzing the discrete kernel, we will consider the simpler but analogous case, where instead of coupling the subdomains using mortaring, we only consider Ω_1, where we impose Dirichlet boundary conditions weakly using the mortar formulation on Γ_{int} and strongly on all other boundaries $\partial\Omega_1 \setminus \Gamma_{\text{int}}$. The discrete space for the magnetic vector potential with weakly imposed BCs on Γ_{int} is then given by

$$X_h^1 = \{\mathbf{u} \in V_{1,h} : ((\mathbf{n} \times \mathbf{u}) \times \mathbf{n}, \boldsymbol{\mu})_{\Gamma_{\text{int}}} = 0 \ \ \forall \boldsymbol{\mu} \in M_h\}. \tag{4.2}$$

The discrete kernel is then defined as the subspace

$$K_h = \{\mathbf{u} \in X_h^1 : (\nabla \times \mathbf{u}, \nabla \times \mathbf{v})_{\Omega_1} = 0 \ \forall \mathbf{v} \in X_h^1\}. \tag{4.3}$$

To determine whether K_h contains all gradients, we also introduce the spaces of H^1-conforming functions

$$X_h^0 = \{\phi \in H^1(\Omega_1) : \phi|_{\Omega_1^i} \in S_p^0(\Omega_1^i; \Sigma_1^i) \text{ for } i = 1, \dots, N_1\}, \tag{4.4}$$

$$X_{h,0}^0 = \{\phi \in H_0^1(\Omega_1) : \phi|_{\Omega_1^i} \in S_p^0(\Omega_1^i; \Sigma_1^i) \text{ for } i = 1, \dots, N_1\} = X_h^0 \cap H_0^1(\Omega_1), \tag{4.5}$$

without and with vanishing traces on Γ_{int}, respectively (but both with vanishing trace on $\partial\Omega_1 \setminus \Gamma_{\text{int}}$). In order to have a discrete space with the correct kernel, it should hold that $\nabla X_{h,0}^0 = K_h$. It can be proven that $\nabla X_{h,0}^0 \subset K_h$. However, equality can not be proven in general. We conjecture that if there are vertices between patches that lie on the interior of Γ_{int}, the dimension of the discrete kernel is larger than the space (4.5) by the number $\#Z_{\Gamma_{\text{int}}}$ of these internal vertices, where $Z_{\Gamma_{\text{int}}}$ denotes the set of interior vertices, i.e.,

$$\dim X_{h,0}^0 \leq \dim K_h = \dim X_{h,0}^0 + \#Z_{\Gamma_{\text{int}}}, \tag{4.6}$$

where $\dim X_{h,0}^0 = \dim \nabla X_{h,0}^0$, due to the homogeneous Dirichlet BCs. Details about this conjecture and a more rigorous discussion can be found in [95]. Here, we will motivate that (4.6) holds using numerical tests. As numerical examples to test this, we solve the Maxwell eigenvalue problem (2.21) for three differ-

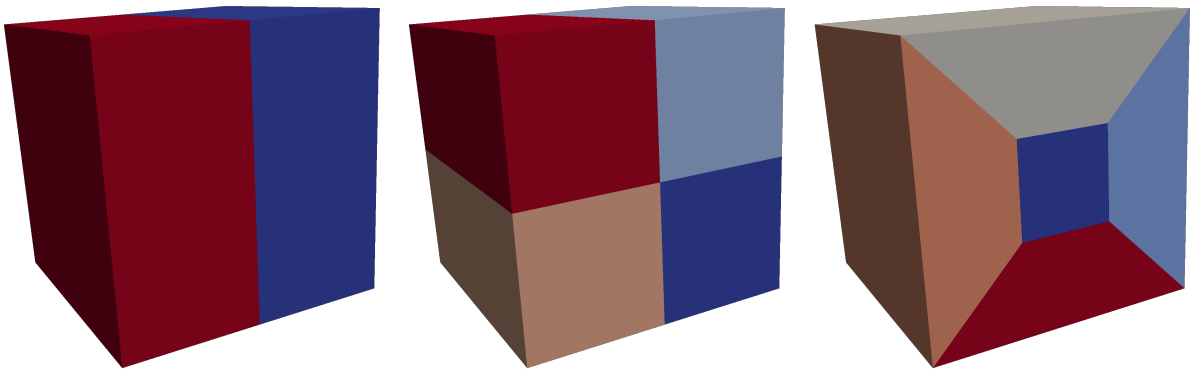

Figure 4.2: Three geometry configurations of the unit cube with two (left), four (center) and five (right) patches. The side facing front is Γ_{int} where the Dirichlet boundary condition is imposed weakly. Taken from [95].

Table 4.1: Dimension of $X^0_{h,0}$ and dimension of the discrete kernel K_h using the spaces M_h and $\widetilde{M}_h$, for the three geometry configurations of Fig. 4.2.

p	h	2 patches			4 patches			5 patches		
		dim $X^0_{h,0}$	dim K_h		dim $X^0_{h,0}$	dim K_h		dim $X^0_{h,0}$	dim K_h	
			M_h	$\widetilde{M}_h$		M_h	$\widetilde{M}_h$		M_h	$\widetilde{M}_h$
2	$1/2$	20	20	20	50	51	50	80	84	80
	$1/3$	63	63	63	147	148	147	219	223	219
3	$1/2$	144	144	144	324	325	324	464	468	464
	$1/3$	468	468	468	1014	1015	1014	1392	1396	1392

ent discretizations within the unit cube, where the analytical solution is known. Here, the homogeneous Dirichlet BCs are imposed weakly on one side, that we will also call Γ_{int}, using mortaring and strongly on all other boundaries. The three configurations of the unit cube are shown in Fig. 4.2. The first geometry (on the left) consists of two patches, such that there are no interior vertices on Γ_{int}, the second one (in the center) consists of four patches and has $\#Z_{\Gamma_{\text{int}}} = 1$ internal vertex and the third configuration (on the right) consists of five patches such that there are $\#Z_{\Gamma_{\text{int}}} = 4$ internal vertices. Table 4.1 shows the dimension of the discrete kernel K_h of the system using the Lagrange multiplier space M_h, which is equal to the number of zero-eigenvalues obtained from the eigenvalue problem, and the expected dimension of the kernel, i.e., dim $X^0_{h,0}$ for the three configurations with two different basis function degrees and refinement levels. We can see that the dimensions of the discrete kernel coincide with the expected dimension for the two-patch case without interior vertices on Γ_{int} and differ by $\#Z_{\Gamma_{\text{int}}}$ for the four- and five-patch configurations according to (4.6), independent of degree and mesh size. The zero eigenvalues and corresponding eigenmodes belonging to $X^0_{h,0}$ can be identified using Kikuchi's mixed formulation [19, 97]. The remaining zero-eigenmodes are the ones introduced by using the multiplier space M_h. Some examples of these spurious modes are visualized in Fig. 4.3. All these spurious modes have oscillations on Γ_{int} which have their maxima on one interior vertex. Since each of the internal vertices of $Z_{\Gamma_{\text{int}}}$ coincides with exactly one control point of the control mesh which has a function associated to it, these spurious modes can be avoided by enriching the space of Lagrange multipliers by the gradients of these functions. We denote by $\mathcal{B}_{Z_{\Gamma_{\text{int}}}} \subset X^0_h$ the basis functions associated to the interior vertices of $Z_{\Gamma_{\text{int}}}$ and by $G_h = \text{span}(\nabla_\Gamma \gamma^0_{\Gamma_{\text{int}}}(\mathcal{B}_{Z_{\Gamma_{\text{int}}}}))$

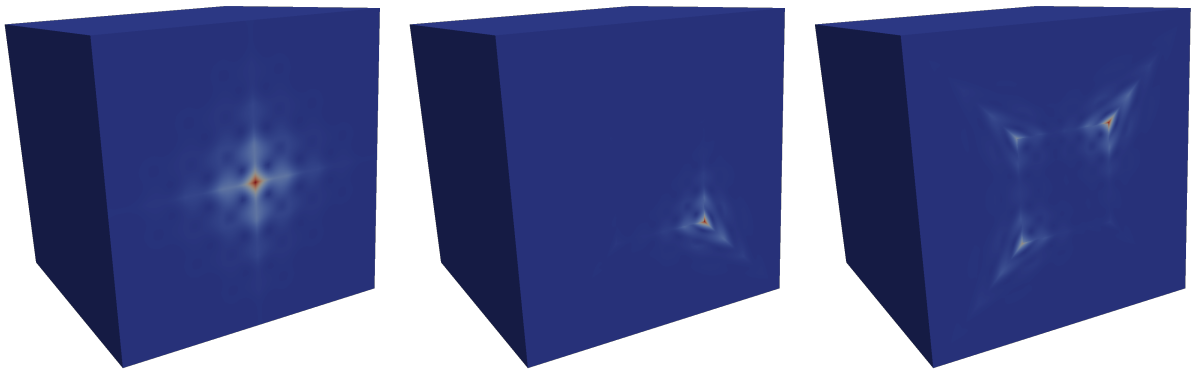

Figure 4.3: Visualization of qualitative magnitude of some functions in the discrete kernel K_h and not in $\nabla V^0_{h,0}$, for four patches (left) and five patches (center and right). Taken from [95].

the space of gradients of the functions of $\mathcal{B}_{Z_{\Gamma_{\text{int}}}}$ on Γ_{int}. The enriched Lagrange multiplier space is then given by

$$\widetilde{M}_h = M_h \oplus G_h, \tag{4.7}$$

with M_h defined in (4.1). The numerical test is repeated using the new, modified Lagrange multiplier space $\widetilde{M}_h$, instead of M_h and therefore also using the modified space in the definitions of X^1_h and K_h in (4.2) and (4.3). The results for the modified multiplier space is also given in Table 4.1. We observe that using the enriched space $\widetilde{M}_h$ we obtain the required equality $\dim(\nabla X^0_{h,0}) = \dim K_h$ for all configurations, independent of degree and mesh size. We therefore conjecture that with the modification (4.7), the discrete kernel is equal to the gradient space, i.e.,

$$\nabla X^0_{h,0} = K_h, \tag{4.8}$$

for details see [95, Appendix A].

4.1.2 Stability of the Harmonic Mortar Formulation

The harmonic coupling (or harmonic mortar) method described in Section 3.3.1.2 results in a saddlepoint system (3.88). It is well known that for this kind of problem the choice of the discrete approximation spaces determines whether or not the obtained system is stable [30, 133].

If the approximation space for the Lagrange multipliers is chosen too large, the system will not be stable, if it is chosen too small, the results might not be accurate enough. Following [64] we investigate and give a criterion for the inf-sup stability for the harmonic mortaring approach depending on the choice of basis functions.

We consider the problem described in Section 3.1.1, where we have two subdomains Ω_1 and Ω_2 representing stator and rotor, connected by the interface Γ_{int} in the air gap. The weak formulation of the problem is given in (3.84)–(3.86). For the sake of a shorter notation, we will use the standard nota-

tion for scalar products where we introduce the notation for a scalar product on the two subdomains as

$$(a,b)_{\Omega_1\cup\Omega_2} = \int_{\Omega_1} a\cdot b\,\mathrm{d}V + \int_{\Omega_2} a\cdot b\,\mathrm{d}V \tag{4.9}$$

for functions $a,b\in L^2(\Omega_1\cup\Omega_2)$ and the duality products $\langle a,b\rangle$ on the spaces $V_h\times V_h'$ and $M_h\times M_h'$, respectively, where V_h' and M_h' denote the dual spaces of V_h and M_h. Note that in (3.84)–(3.86) we used the notation $A_k = A_h|_{\Omega_k}\in V_h\left(\Omega_k\right)$ where $V_h = V_h|_{\Omega_1}\cup V_h|_{\Omega_2}$ meaning that the discrete functions restricted to one of the subdomains and extended by zero to the other belong to the space V_h. The problem then reads: Find $A_h\in V_h\subset H^1\left(\Omega_1\cup\Omega_2\right), \lambda\in M_h\subset H^{-1/2}\left(\Gamma_{\text{int}}\right)$, such that

$$\left(\nu\nabla A_h,\nabla v\right)_{\Omega_1\cup\Omega_2} + \left\langle\lambda,[v]\right\rangle_{\Gamma_{\text{int}}} = \left\langle J_{\text{src}},v\right\rangle_{\Omega_1\cup\Omega_2} + \left\langle\mathbf{M}^{\perp},\nabla v\right\rangle_{\Omega_1\cup\Omega_2} \tag{4.10}$$

$$\left\langle\left[A_h\right],\mu\right\rangle_{\Gamma_{\text{int}}} = 0 \tag{4.11}$$

for all $v\in V_h,\mu\in M_h$. Here, $[v]=v_1-v_2$ denotes the jump of any field v across the interface Γ_{int}.

The problem (4.10) and (4.11) has a unique solution for $J_{\text{src}}\in L^2\left(\Omega\right)$ and $\mathbf{M}^{\perp}\in L^2\left(\Omega\right)^2$ and there is a constant C that is independent of A_h, λ, J_{src} and $\mathbf{M}^{\perp}$, such that

$$\|A_h\|_{H^1\left(\Omega_1\cup\Omega_2\right)} + \|\lambda\|_{H^{-1/2}(\Gamma_{\text{int}})} \le C\left(\|J_{\text{src}}\|_{L^2\left(\Omega_1\cup\Omega_2\right)} + \|\mathbf{M}^{\perp}\|_{L^2\left(\Omega_1\cup\Omega_2\right)}\right) \tag{4.12}$$

holds, where C only depends on the geometry of the domain and the upper and lower bounds of the reluctivity ν. As mentioned before, λ is the tangential, i.e., angular component of the magnetic field strength $\mathbf{H}$ on the interface.

The discrete inf-sup stability condition, or LBB condition, see [9, 28, 30], reads

$$\inf_{\mu\in M_h}\sup_{v\in V_h}\frac{\left\langle\mu,[v]\right\rangle_{\Gamma_{\text{int}}}}{\|\mu\|_{H^{-1/2}(\Gamma_{\text{int}})}\|v\|_{H^1(\Omega_1\cup\Omega_2)}} \ge \beta > 0. \tag{4.13}$$

Using the Galerkin orthogonality we can obtain the error estimate [29, 30]

$$\begin{aligned}\|A-A_h\|_{H^1(\Omega_1\cup\Omega_2)} + \|\lambda-\lambda_N\|_{H^{-1/2}(\Gamma_{\text{int}})}&\\ \le C\left(\inf_{v_h\in V_h}\|A-v_h\|_{H^1(\Omega_1\cup\Omega_2)} + \inf_{\mu_N\in M_N}\|\lambda-\mu_N\|_{H^{-1/2}(\Gamma_{\text{int}})}\right).&\end{aligned} \tag{4.14}$$

We assume M_h to be the space of trigonometric polynomials of degree $\le N$ given in (3.90) and V_h to be the space of piecewise polynomials of degree $\le p$, e.g., B-splines, defined on a mesh that can be based on rectangles (as explained in Section 3.2.1) or triangles (as in the classical FEM) with characteristic size h. To fulfill the discrete inf-sup condition we require the following assumption. We assume that there is a linear projection operator $\Pi_h : V|_{\Omega_1}\to V_h|_{\Omega_1}$ such that

$$\|\Pi_h v_1\|_{H^1(\Omega_1)} \le c_1\|v_1\|_{H^1(\Omega_1)}, \tag{4.15}$$

$$\Pi_h v_1 = \pi_h v_1 \qquad \text{on } \Gamma_{\text{int}}, \tag{4.16}$$

$$\|v-\pi_h v\|_{H^{-1/2}(\Gamma_{\text{int}})} \le c_2\frac{h}{k}\|v\|_{H^{1/2}(\Gamma_{\text{int}})}, \tag{4.17}$$

with the L_2 projection on the interface $\pi_h : L_2(\Gamma_{\text{int}}) \to V_h|_{\Omega_1 \cap \Gamma_{\text{int}}}$. Given these conditions, there exists a constant $0 < \epsilon < 1$ which is exclusively dependent on c_1 and c_2, such that the discrete inf-sup condition (4.13) holds, with the inf-sup constant given by $\beta = \beta(\epsilon)$. This will hold if the degree N of trigonometric polynomials for the Lagrange multipliers and the size of the mesh h are chosen such that

$$Nh/p \leq 1 - \epsilon, \tag{4.18}$$

with the polynomial degree p. The proof can be found in [64]. The operator Π_h can be constructed following [42, 148] or [34]. This condition holds for various discretization methods, including IGA or FEM. In summary, the harmonic coupling method achieves stability if the number of degrees of freedom of the polynomial discretization located at the interface $N \sim p/h$ exceeds the number of harmonic basis functions employed for the coupling to a certain degree. Examples and numerical tests are given in Section 6.4.1.

4.2 Tree-Cotree Gauging for Isogeometric Analysis

The tree-cotree gauging [1, 119] introduced in Section 3.4 for lowest order FEM using Nédélec edge elements can be employed to obtain a uniquely solvable system. As we use IGA for the discretization, we will propose an extension of the tree-cotree gauging method to be applicable in this context based on [95]. In the case of IGA with lowest degree $p = 1$ basis functions in S_p^1, the DoFs can be directly interpreted as line integrals on edges of the (control) mesh, as in the classical FEM with Nédélec elements [117] and are thus associated to these edges in the control mesh. Similarly, basis functions of the spline spaces S_p^0, S_p^2 and S_p^3 are associated to vertices, facets and cells of the control mesh, respectively. As explained in [95], there exists an isomorphism of the spaces S_p^k to the lowest order spaces defined on the control mesh for $k = 0, 1, 2$ and 3. These isomorphisms commute with the differential operators [14, 36], such that a spline function is in the kernel of a differential operator, in particular the curl operator, if and only if its image in the lowest order spline space defined on the same control mesh is in the kernel of the operator. Therefore, filtering out the basis functions spanning the discrete kernel in the lowest order space is equivalent to filtering out the kernel in higher order spline spaces. This means that it is sufficient to build the tree on the control mesh (as in the lowest order case for the actual mesh) and then to identify the corresponding B-spline basis functions. Removing those from our system is a correct way of gauging and can be applied for any degree of B-spline basis functions. This allows to reuse existing algorithms for the low-order case for the tree-cotree gauging in IGA without the need to alter them. The generation of a tree in IGA is even simpler than for classical tetrahedral FE due to the hexahedral structure of the control mesh. Note that, for higher order classical FE, the application of tree-cotree gauging is not as straightforward as it is for the B-splines, see, e.g., [135, 145].

4.2.1 Tree-Cotree Gauging for Isogeometric Mortaring

For the computation of rotating machines in three dimensions, we require mortaring as well as a gauging method that works in combination with mortaring. We want to use isogeometric mortaring as explained in Section 3.3.1.1 and use tree-cotree gauging explained in Section 3.4. For multi-patch geometries, the construction of the tree is straightforward due to the conformity of the patches and their control mesh at the interfaces. Therefore, the tree can be built on the whole multi-patch model using the same algorithm

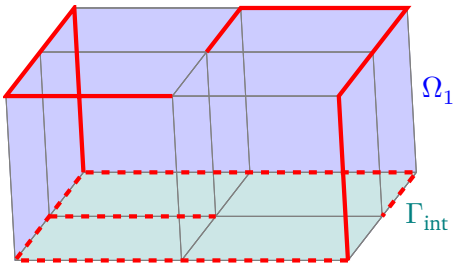

Figure 4.4: Visualization of the tree in the dependent domain Ω_1. The tree is shown in red. Dashed lines represent the edges that are built on the interface Γ_{int} but are then removed from the tree. Taken from [95].

as for single-patch geometries, see Algorithm 1. However, for mortared domains it is not obvious how to apply tree-cotree gauging, as the subdomains have non-conforming interfaces, and independent and dependent domains have to be treated differently. The Lagrange multiplier can be interpreted as leaving the solution free on the interface Γ_{int} for the independent subdomain while constraining it on Γ_{int} for the dependent subdomain. Therefore, for the construction of the tree, the interface on the independent subdomain Ω_2 can be treated as a Neumann BC. Thus, to build the tree for the independent subdomain we can use Algorithm 1 replacing Γ_{dir} by $\partial\Omega_2 \cap \Gamma_{\text{dir}}$, and Γ_{neu} by $\partial\Omega_2 \cap (\Gamma_{\text{neu}} \cup \Gamma_{\text{int}})$. The interface on the dependent domain Ω_1 on the other hand has to be treated more similarly to a Dirichlet side. However, since the values of the DoFs are not imposed in a strong way but via Lagrange multipliers, all edges of the interface have to be added to the cotree (i.e., removed from the tree) again. This is visualized in Fig. 4.4. The modified algorithm for the construction of the tree in the dependent subdomain can then be written as:

Algorithm 2 ***Modified Tree-Cotree Decomposition***

1. *Build a spanning tree on the subgraph associated to* $\partial\Omega_1 \cap \Gamma_{\text{int}}$.
2. *Grow the tree on the Dirichlet boundary* $\partial\Omega_1 \cap (\Gamma_{\text{dir}} \setminus \Gamma_{\text{int}})$.
3. *From the vertices on* $\partial\Omega_1 \cap (\Gamma_{\text{dir}} \cup \Gamma_{\text{int}})$*, grow the tree on* $\partial\Omega_1 \cap \Gamma_{\text{neu}}$.
4. *Grow the tree on the remaining graph in the interior of* Ω_1.
5. *Restore all edges supported on* Γ_{int} *as cotree DoFs.*

As explained in Section 3.4 for the single domain case, we set the tree-DoFs to zero and thus, obtain the linear system for mortaring that we have to solve for the cotree-DoFs

$$\begin{bmatrix} \mathbf{K}^1_{CC} & \mathbf{0} & \mathbf{G}^1_C \\ \mathbf{0} & \mathbf{K}^2_{CC} & \mathbf{G}^2_C \\ (\mathbf{G}^1_C)^\top & (\mathbf{G}^2_C)^\top & \mathbf{0} \end{bmatrix} \begin{bmatrix} \mathbf{a}^1_C \\ \mathbf{a}^2_C \\ \boldsymbol{\mu} \end{bmatrix} = \begin{bmatrix} \mathbf{f}^1_C \\ \mathbf{f}^2_C \\ \mathbf{0} \end{bmatrix}, \tag{4.19}$$

where the subscripts T and C indicate the affiliation to tree/cotree and the superscript refers to the respective subdomain. Note that the Dirichlet BCs are imposed before the solution of the system, such that the edges on $\partial\Omega_1 \cap \Gamma_{\text{dir}}$ are not part of the final cotree for which the system is solved.

Since the Lagrange multipliers impose the continuity across the interface in a weak sense by weakly constraining the dependent subdomain, the obtained problem is very similar to imposing the Dirichlet BCs

weakly as we did in Section 4.1.1. Therefore, according to our conjecture, applying the tree-cotree gauge using Algorithm 2 with the multiplier space M_h would not result in a correctly gauged problem. In fact, only the gradient functions that vanish on $\partial\Omega_1 \cap (\Gamma_{\text{dir}} \cup \Gamma_{\text{int}})$ (analogous to ∇X_h^0 in Section 4.1.1) are filtered out. Thus, using the space M_h for the Lagrange multipliers would leave $\#Z_{\Gamma_{\text{int}}}$ gradient functions in the kernel, where $\#Z_{\Gamma_{\text{int}}}$ is the number of interior vertices on the interface Γ_{int}. However, these gradient functions can be correctly filtered out by using the modified multiplier space $\widetilde{M}_h$ we introduced in (4.7). Thus, with the modified multiplier space and tree-cotree gauging, we obtain the uniquely solvable problem (4.19).

4.3 Torque Computation

The magnetic torque is one of the KPIs of electric machines. Torque computation has been a topic of research and various strategies have been proposed, for instance, the use of the Maxwell stress tensor or virtual displacements, see [83, 85]. In the classical FEM, most coupling methods share the problem of geometric mismatch at the interface, see Figure 3.5. This may lead to numerical noise which is particular cumbersome when analyzing cogging torque. It is reported in the literature that classical FEM computations of the torque, e.g., using Nédélec elements, often suffer from inaccuracies [6]. These accuracy issues are particularly noticeable in the tangential component of the magnetic field which is computed using numerical derivation, leading to an amplification of errors in the vector potential. Errors due to mesh mismatch can be mitigated by mesh adaptation, see [99, Section 5.4] and similarly [157, Section 5.2.3]. The geometry error can be avoided when using IGA. In this section, we introduce some approaches for torque computation of electric machines discretized with IGA based on [116].

4.3.1 Via Maxwell Stress Tensor

The Maxwell stress tensor (2.43) introduced in Section 2.3.3 can be applied to compute the torque in electric machines using (2.44). In the context of rotating electric machines, the torque we are interested in is usually the one acting on the rotor around its central axis. The integration surface for its calculation is typically chosen as a (cylindrical) surface in the air gap between stator and rotor. Effects on the base surfaces of the cylinder can usually be neglected, leading to a simplified integral for torque calculation given by

$$T_z = \int_0^{l_z} \int_0^{2\pi} B_r H_\theta R^2 \, \mathrm{d}\theta \, \mathrm{d}z, \tag{4.20}$$

where we used a cylindrical coordinate system, denoting the radial and angular components of the **B**- and **H**-field by B_r and H_θ, respectively. R denotes the radius of the integration surface and l_z is the length of the electric machine. For two-dimensional models, the integral in (4.20) reduces to a line integral over a circle in the air gap

$$T_z = l_z \int_0^{2\pi} B_r H_\theta R^2 \, \mathrm{d}\theta. \tag{4.21}$$

4.3.2 Arkkio's Method

For an exact solution of the magnetic field, the torque remains independent of the integration radius within the air gap. However, due to inaccuracies in computed field components, the integral tends to be sensitive to the radius of the integration surface. Such inaccuracies are further amplified in the classical FE formulation due to the numerical differentiation of the magnetic vector potential, especially in normal direction which is carried out to obtain the tangential component of the magnetic field. According to [6], these inaccuracies can cause the torque to vary by up to $50\,\%$ of the average value for a classical FE mesh. To address these problems, Arkkio introduced a method for the calculation of the torque, based on the principle of virtual work. This method calculates the torque for a two-dimensional model using an integral over a torque-free region, such as the air gap, rather than a one-dimensional line-integral as (4.21). The integral is then averaged to determine the torque, thereby mitigating the impact of the numerical inaccuracies caused by the choice of the integration radius. The torque is then obtained using the Arkkio method as

$$T_z = \frac{l_z}{\delta} \int_0^{\delta} \int_0^{2\pi} B_r H_\theta (R + r)^2 \, \mathrm{d}\theta \, \mathrm{d}r, \tag{4.22}$$

where δ represents the thickness of the integration surface in the air gap. For the computation in the three-dimensional case, this can be done similarly using

$$T_z = \frac{1}{\delta} \int_0^{l_z} \int_0^{\delta} \int_0^{2\pi} B_r H_\theta (R + r)^2 \, \mathrm{d}\theta \, \mathrm{d}r \, \mathrm{d}z, \tag{4.23}$$

where again, the integration volume lies in the air gap. While Arkkio's method performs the integration on a (discretized) annulus/cylinder shell within the air gap of electric machines, a slightly more general approach is the eggshell method [84, 85]. In the eggshell method any integration surface/volume in the air surrounding the rotor can be chosen, in particular one along the (unstructured) FE mesh.

4.3.3 Lagrange Multiplier Method

In our mortaring setting detailed in Section 3.3.1, using (3.67), it can be easily verified that the third component of the Lagrange multiplier $\lambda_3 = -H_\theta$ can be identified with the negative angular component of the magnetic field. Therefore, the torque can be computed without explicitly calculating H_θ, using the Lagrange multiplier [50, 116] via

$$T_z = -\int_0^{l_z} \int_0^{2\pi} B_r \lambda_3 R^2 \, \mathrm{d}\theta \, \mathrm{d}z. \tag{4.24}$$

Here, $B_r = \mathrm{curl}(\mathbf{A}) \cdot \mathbf{n}_\Gamma$ is evaluated either on the boundary of Ω_1 (stator) or Ω_2 (rotor).

Special Case: Harmonic Mortaring In the two-dimensional case, the torque can also be computed using the Lagrange multiplier as done in (4.24), where in this case $H_\theta = -\lambda$. However, in the case of harmonic mortaring we can take advantage of the dependence on the rotation angle α. Based on [63], we will

derive a formulation of the torque based on the energy in the system. Due to the coupling conditions (3.80) and (3.81), the solution (A_1, A_2, λ) implicitly depends on the rotation angle. To highlight this, we denote the dependence of a function u on the rotation angle by $u(\star;\alpha)$. Further, the derivative with respect to α will be denoted by

$$u'(\star;\alpha) := \frac{\mathrm{d}}{\mathrm{d}\alpha} u(\star;\alpha) := \lim_{\varepsilon\to 0} \frac{1}{\varepsilon}(u(\star;\alpha+\varepsilon) - u(\star;\alpha)). \tag{4.25}$$

By differentiation of (3.80) using the chain rule, we obtain

$$A_1'(\mathbf{x}_\theta;\alpha) = A_2'(\tilde{\mathbf{x}}_{\theta-\alpha};\alpha) + \frac{\mathrm{d}}{\mathrm{d}\theta} A_2(\tilde{\mathbf{x}}_{\theta-\alpha};\alpha) \qquad \mathbf{x}_\theta \in \Gamma_{\text{int}}, \tag{4.26}$$

where a point in the rotated coordinate system of Ω_2 is denoted by $\tilde{\mathbf{x}}_{\theta-\alpha} = \rho_{-\alpha}(\mathbf{x}_\theta)$ and corresponds to the point $\mathbf{x}_\theta = (r_\Gamma \cos(\theta), r_\Gamma \sin(\theta))$ on the interface with radius r_Γ in the global coordinate system, see Fig. 3.6 for a visualization. Therefore, by differentiating, the weak coupling condition, (3.86) can be rephrased as

$$\langle A_2' \circ \rho_{-\alpha} - A_1', \mu\rangle_{\Gamma_{\text{int}}} = -\langle \frac{\mathrm{d}}{\mathrm{d}\theta} A_2 \circ \rho_{-\alpha}, \mu\rangle_{\Gamma_{\text{int}}}. \tag{4.27}$$

This will be used in the following derivation of the torque. The magnetic energy stored in the domains for linear material relations is given by

$$E(A_1, A_2) = \int_{\Omega_1} \left(\frac{\nu}{2}|\nabla A_1|^2 + \mathbf{M}^\perp \nabla A_1\right) \mathrm{d}\Omega + \int_{\Omega_2} \left(\frac{\nu}{2}|\nabla A_2|^2 + \mathbf{M}^\perp \nabla A_2\right) \mathrm{d}\Omega. \tag{4.28}$$

Due to the dependence of A_1 and A_2 on the rotation angle, the energy also implicitly depends on α. Differentiating this energy with respect to the rotation angle α and using the variational identities (3.84) and (3.85), where we set $v_1 = A_1'$ and $v_2 = A_2'$, yields

$$\begin{aligned} \frac{\mathrm{d}}{\mathrm{d}\alpha} E(A_1, A_2) &= (\nu \nabla A_1, \nabla A_1')_{\Omega_1} + (\mathbf{M}^\perp, \nabla A_1')_{\Omega_1} \\ &\quad + (\nu \nabla A_2, \nabla A_2')_{\Omega_2} + (\mathbf{M}^\perp, \nabla A_2')_{\Omega_2} \\ &= (J_{\text{src}}, A_1')_{\Omega_1} + (J_{\text{src}}, A_2')_{\Omega_2} + \langle \lambda, A_1'\rangle_{\Gamma_{\text{int}}} - \langle \lambda, A_2' \circ \rho_{-\alpha}\rangle_{\Gamma_{\text{int}}}. \end{aligned} \tag{4.29}$$

Exploiting (4.27), we can express the derivative of the energy as

$$\frac{\mathrm{d}}{\mathrm{d}\alpha} E(A_1, A_2) = (J_{\text{src}}, A_1')_{\Omega_1} + (J_{\text{src}}, A_2')_{\Omega_2} + \langle \lambda, \frac{\mathrm{d}}{\mathrm{d}\theta} A_2 \circ \rho_{-\alpha}\rangle_{\Gamma_{\text{int}}}. \tag{4.30}$$

Here, the energy required to maintain the electric source current in the windings during an infinitesimal rotor rotation is given by the first two terms. The last term represents the mechanical energy needed to rotate the rotor by an infinitesimal angle, denoted as $\frac{\mathrm{d}E_{\text{mech}}}{\mathrm{d}\alpha}$. As the work E_{mech} required for a rotation between the angles α_1 and α_2 is given by the integral of the torque, we can write

$$0 = E_{\text{mech}} + \int_{\alpha_1}^{\alpha_2} T_z(\alpha)\, \mathrm{d}\alpha, \tag{4.31}$$

with the torque $T_z(\alpha)$. This can then be rewritten using (4.30) to obtain the torque as

$$T_z(\alpha) = -\frac{\mathrm{d}}{\mathrm{d}\alpha} E_{\text{mech}}(A_1, A_2) = -\langle \lambda, \frac{\mathrm{d}}{\mathrm{d}\theta} A_2 \circ \rho_{-\alpha} \rangle_{\Gamma_{\text{int}}}. \tag{4.32}$$

Note that as we only considered the two-dimensional model where we assumed a unit length L of the machine, the energy and torque have to be scaled by the actual length of the machine to obtain the correct physical quantities.

Using integration by parts and exploiting the symmetry of the machine, we can rewrite (4.32) as

$$T_z(\alpha) = \langle \frac{\mathrm{d}}{\mathrm{d}\theta} \lambda \circ \rho_{\alpha}, A_2 \rangle_{\Gamma_{\text{int}}}. \tag{4.33}$$

This formula is particularly useful when discretizing with harmonic mortaring. This is because the Lagrange multiplier functions λ, i.e., trigonometric polynomials, can be easily differentiated and evaluated at a point rotated around the origin.

These energy-based considerations can be conducted analogously for the discretized fields. By abuse of notation where $(A_1, A_2, \lambda) \in V_{h,1} \times V_{h,1} \times M_N$ is a solution of the discrete problem, we can see that the discrete energy balance (4.30) also holds on the discrete level. This is obtained from the discretized approximation of the torque using (4.32) or (4.33), provided that the Lagrange multipliers are sufficiently smooth. For a more in-depth analysis of the discretized problem, including well-posedness, we refer to [63].

For the computation of the torque, it is sufficient to solve a low-dimensional interface problem (3.95), as detailed in Section 3.3.1.2, for each rotation angle. This approach results in a highly efficient method for torque computation.

Algebraically, using the discretization described in Section 3.1.1, we can express (4.30) as

$$\begin{aligned} \frac{\mathrm{d}}{\mathrm{d}\alpha} E &= (\mathbf{K}_1 \mathbf{u}_1, \mathbf{u}_1') + (\mathbf{f}_{M,1}, \mathbf{u}_1') + (\mathbf{K}_2 \mathbf{u}_2, \mathbf{u}_2') + (\mathbf{f}_{M,2}, \mathbf{u}_2') \\ &= (\mathbf{f}_{\text{src},1}, \mathbf{u}_1') + (\mathbf{f}_{\text{src},2}, \mathbf{u}_2') + (\mathbf{G}_1^\top \boldsymbol{\lambda}, \mathbf{u}_1') - (\mathbf{G}_2^\top \boldsymbol{\lambda}, \mathbf{u}_2') \\ &= (\mathbf{f}_{\text{src},1}, \mathbf{u}_1') + (\mathbf{f}_{\text{src},2}, \mathbf{u}_2') + (\mathbf{G}_1 \mathbf{u}_1' - \mathbf{G}_2 \mathbf{u}_2', \boldsymbol{\lambda}) \\ &= (\mathbf{f}_{\text{src},1}, \mathbf{u}_1') + (\mathbf{f}_{\text{src},2}, \mathbf{u}_2') + (\mathbf{G}_2' \mathbf{u}_2, \boldsymbol{\lambda}), \end{aligned} \tag{4.34}$$

where $\mathbf{f}_{\text{src}}$ and $\mathbf{f}_M$ denote the contributions of $\mathbf{f}$ due to the source currents and the permanent magnets, respectively, and we utilize the common notation $(\star, \star)$ for scalar products. Note that using (3.93), the derivative of the coupling matrix $\mathbf{G}_2(\alpha)$ can be expressed as $\mathbf{G}_2'(\alpha) = \mathbf{G}_2(0)\mathbf{R}'(\alpha)$. Thus, the discrete torque can be easily computed from the discrete solution using

$$T_z(\alpha) = -(\mathbf{G}_2' \mathbf{u}_2, \boldsymbol{\lambda}) = -\boldsymbol{\lambda}^\top(\alpha)\, \mathbf{G}_2'(\alpha) \mathbf{u}_2(\alpha). \tag{4.35}$$

4.4 Geometric Modeling of the Winding Functions

One of the advantages of IGA is that it allows to directly use geometries obtained from CAD software. However, in practice, they are usually given in their boundary representation. In classical IGA, we require

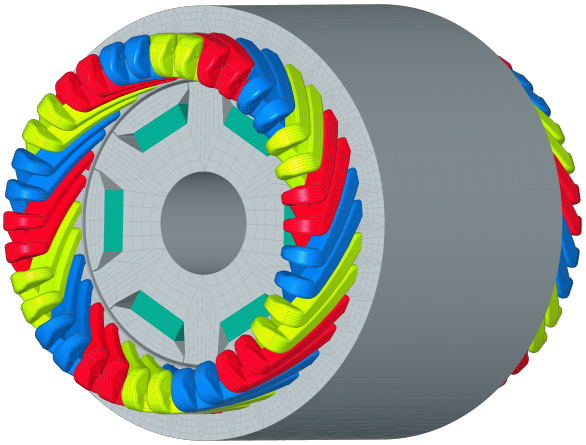

Figure 4.5: Trivariate machine model of a PMSM created using IRIT [65].

the geometry in a trivariate B-spline or NURBS representation. Furthermore, the patches need to be described as regular transformations, prohibiting most boolean operations on the geometry, e.g., union or subtraction of intersecting geometries, which are often used in CAD models. To build multi-patch models for the simulation of electric machines which fulfill these requirements, we can use volumetric CAD kernels, e.g., IRIT [65]. A multi-patch electric machine model has been created using IRIT, including the winding heads. The model uses the common stranded conductor approximation [146] of the actual machine geometry as is does not resolve the wires inside the windings and neglects the connecting wires between the windings. The trivariate NURBS discretization created with IRIT is shown in Fig. 4.5

However, in electromagnetics, the air region also needs to be discretized. It can easily be seen that in the machine model the discretization of the air region around the winding heads is complicated and a decomposition into (curved) hexahedral elements is not straightforward. Instead of actually modeling the winding heads as separate patches for the computation of the fields in the machine, we propose to treat them geometrically as air and to impress the excitation current only as a right-hand side. This does not resolve the jump of the current density correctly. It results in a smearing of the right-hand side due to the regularity of the basis functions inside the patches and of the solution. In practice, this means the basis functions on the patches containing the winding heads (but not modeling them as a separate patch) should be refined and the number of quadrature nodes needs to be increased to approximate the right-hand side integrals sufficiently well.

Typically, the right-hand side is not given in closed form as a winding function. One way to approximate of the current in the windings is to use the model of one winding for a computation of the electric current distribution inside the winding. The obtained current distribution can then be used for the right-hand side in (3.13). To determine the current distribution in the windings [146], we solve a stationary current problem (2.40)–(2.41) in the coil domain Ω_c of the form

$$-\nabla \cdot \sigma \nabla \Phi = 0 \qquad \text{in } \Omega_c, \tag{4.36}$$

$$\Phi_1 = 0 \quad \text{and} \quad \Phi_2 = 1 \qquad \text{in } \Gamma_{\text{dir},1}, \Gamma_{\text{dir},2}, \tag{4.37}$$

$$\mathbf{n} \cdot (\sigma \nabla \Phi) = 0 \qquad \text{in } \Gamma_{\text{neu}}, \tag{4.38}$$

where the Dirichlet BC is set by cutting the winding and applying the voltages Φ_1 and Φ_2 on both ends of the windings $\Gamma_{\text{dir},1}$ and $\Gamma_{\text{dir},2}$, see Fig. 4.7a. All other boundaries are Neumann boundaries. Note, that for the solution, (2.40)–(2.41) can be solved treated as an electroquasistatic problem if an appropriate stabilization is employed, see, e.g. [10]. The source current density required for the right-hand side of (3.13) in Ω is then given by

$$\mathbf{J}_{\text{src}}(\mathbf{x}) = \boldsymbol{\chi}(\mathbf{x})\, i = -\sigma \nabla \Phi(\mathbf{x}). \tag{4.39}$$

Note, that we are solving (3.13) and (4.36)–(4.38) on different domains using different mappings, see Fig. 4.6. Therefore, we have to take special care in the implementation. The stationary current problem (4.36)–(4.38) is solved in the coil domain Ω_{c} which is given by the mapping

$$\mathbf{F}_{\text{c}} : \hat{\Omega} \to \Omega_{\text{c}}, \tag{4.40}$$

and $\Phi(\mathbf{x}_{\text{c}})$ depends on $\mathbf{x}_{\text{c}} \in \Omega_{\text{c}}$. The current density in the domain Ω where we solve (3.13) is therefore given by

$$\mathbf{J}_{\text{src}}(\mathbf{x}) \begin{cases} -\sigma \nabla \Phi(\mathbf{x}) & \mathbf{x} \in \Omega_{\text{c}}, \\ \mathbf{0} & \mathbf{x} \notin \Omega_{\text{c}}. \end{cases} \tag{4.41}$$

In IGA implementations, differentiation and integration of the basis functions are evaluated on the reference domain $\hat{\Omega}$. This means that the gradient is evaluated on the function $\hat{\Phi}$ in the reference domain $\hat{\Omega}$ and the gradient in the physical domain is obtained using the push-forward (3.45) as

$$\nabla \Phi(\mathbf{x}_{\text{c}}) = \left(\mathrm{d}\mathbf{F}_{\text{c}}\right)^{-\top} \nabla \hat{\Phi}\left(\mathbf{F}_{\text{c}}^{-1}\left(\mathbf{x}_{\text{c}}\right)\right) \qquad \mathbf{x}_{\text{c}} \in \Omega_{\text{c}} \tag{4.42}$$

In practice, we require the current distribution for the right-hand side (3.13) in the domain $\Omega = \mathbf{F}\left(\hat{\Omega}\right)$. Transforming the right-hand side integral to the reference domain and applying the push-forward (3.45) we obtain

$$\int_{\Omega} \mathbf{J}_{\text{src}}(\mathbf{x}) \cdot \mathbf{v}_i(\mathbf{x})\, \mathrm{d}\Omega = \int_{\hat{\Omega}} \mathbf{J}_{\text{src}}(\mathbf{F}(\hat{\mathbf{x}})) \cdot (\mathrm{d}\mathbf{F})^{-\top} \hat{\mathbf{v}}_i(\hat{\mathbf{x}}) \det(\mathrm{d}\mathbf{F})\, \mathrm{d}\hat{\Omega}, \tag{4.43}$$

$$= \int_{\hat{\Omega}} \sigma \left(\mathrm{d}\mathbf{F}_{\text{c}}\right)^{-\top} \nabla \hat{\Phi}\left(\mathbf{F}_{\text{c}}^{-1}\left(\mathbf{F}\left(\hat{\mathbf{x}}\right)\right)\right) \cdot (\mathrm{d}\mathbf{F})^{-\top} \hat{\mathbf{v}}_i(\hat{\mathbf{x}}) \det(\mathrm{d}\mathbf{F})\, \mathrm{d}\hat{\Omega}. \tag{4.44}$$

Employing this approach for the solution of the example domain shown in Fig. 4.6, we obtain the magnetic flux shown in Fig. 4.8b (a single-patch background domain). As a reference, the solution in the domain with discretized windings (multi-patch construction with 39 patches) is shown in Fig. 4.8a. Both results are in good agreement and the example shows that even in this simple case the geometric flexibility is significantly increased by not resolving the windings. The solution of (4.36)–(4.38) for the scalar potential in one of the windings of the machine shown in Fig. 4.5 is shown in Fig. 4.7. The solution of the stationary current problem in the winding is ready to be used as a right-hand side for a full machine simulation.

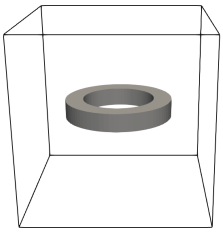

(a) Physical setup of complete domain including winding.

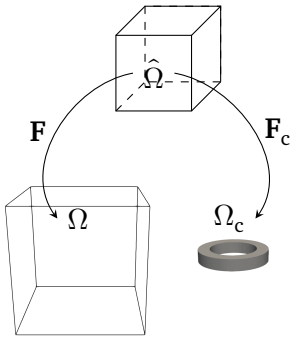

(b) Mappings from the reference domain $\hat{\Omega}$ to the discretized domains Ω and Ω_c.

Figure 4.6: Example of a domain including a winding. The domain is discretized using two mappings. Domain Ω is the domain without the winding. Domain Ω_c is only the winding.

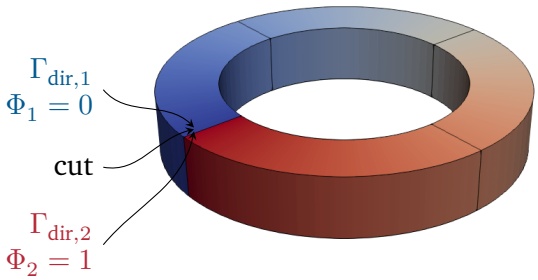

(a) Example winding.

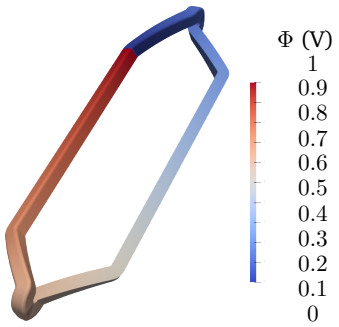

(b) Machine winding

Figure 4.7: Scalar potential computed as the solution of (4.36)–(4.38) in an annular cylinder-shaped winding and in one winding of the PMSM from Fig. 4.5.

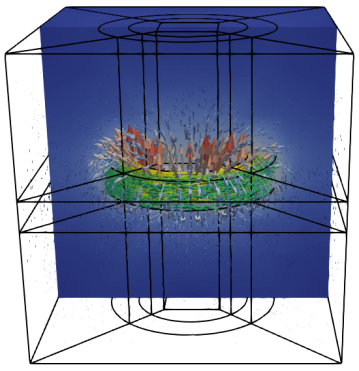

(a) Domain with resolved winding.

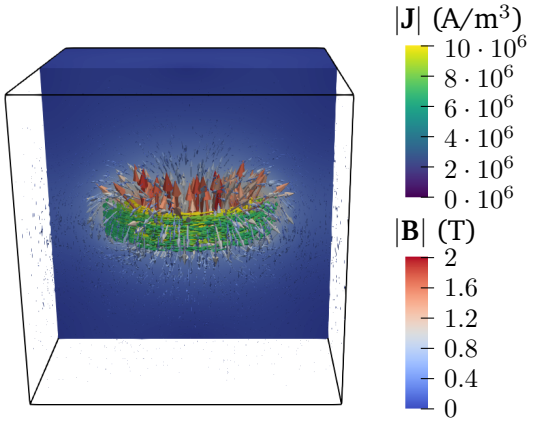

(b) Domain with unresolved windings.

Figure 4.8: Magnetic flux density as a solution of (3.13) in the domain with resolved (multi-patch) and unresolved (single-patch) winding.

4.5 Summary

In this chapter we have presented methods which facilitate efficient simulation of rotating electric machines based on isogeometric analysis. For the coupling of stator and rotor via the mortar method, we have extended the B-spline spaces for mortaring introduced in [32] such that the discrete kernel corresponds to the discretized continuous one. To solve the emerged mortar problem, a gauging condition is necessary. The application of tree-cotree gauging in the context of IGA is discussed. The method of tree-cotree gauging has been adapted to be compatible with non-conforming mortared subdomains, where a tree cannot be constructed on the entire domain. This newly adapted tree-cotree decomposition for mortaring has been demonstrated to yield spurious-free solutions for the Maxwell eigenvalue problem.

We have established a condition for the stability of the harmonic mortar formulation, which allows to automatize the choice of the discrete Lagrange multiplier space for the two-dimensional simulation of electric machines. Different methods for torque computation in electric machines have been presented, where we have introduced Lagrange multiplier-based formulations, allowing for an efficient computation.

Finally, we have proposed a method for the simulation of a full machine model. This approach avoids the cumbersome construction of patches which are conforming between the winding heads and air region. This chapter equips us with advanced tools necessary for an efficient simulation of electric machines using isogeometric analysis.

5 Shape Optimization

Different objectives might be pursued when optimizing electric machines, among others, a few of them are for example, efficiency, i.e., high power output for low power consumption, low cost, small size, high power density, reducing amount of rare earth materials or smoothness of the rotation. In industry, up to 20 key performance indicators are considered [124]. Structural optimization can generally be categorized into three types, see Fig. 5.1. The first, parameter optimization (Fig. 5.1a), aims to optimize geometrical parameters like different lengths, radii or angles to obtain an optimal machine. The second, topology optimization (Fig. 5.1b), is employed to find new geometrical setups, e.g., by assigning material density values to the structure, such that holes and different material distributions can be obtained. The third, shape optimization (Fig. 5.1c), involves manipulating the shape of the structure without changing its topology. Various optimization approaches have been studied in the past and are still an ongoing field of research. Originally, optimization methods based on lumped parameter or magnetic equivalent circuits have been used to improve the design. Over the past three decades, FE-based (or mathematically speaking PDE-constrained) optimization methods have been in focus [53, 60]. In the beginning, mainly gradient-based optimization methods have been used (see, e.g., [139, 151, 159]). However, also stochastic and population-based optimization methods have gained popularity [80, 103], e.g., genetic algorithms and particle swarm methods (see, e.g., [105]). These optimization methods are particularly interesting for multi-objective optimization (see, e.g., [12, 86]). For the optimization of electric machines, in particular PMSMs, stochastic algorithms are commonly used [11, 38, 149]. Promising improvements in the design and behavior of electrical machines have recently been achieved by means of parameter-based optimization methods for single- and multi-objective optimization problems (see, e.g., [21, 51, 156]). Deep-Learning has been demonstrated to be effective for the prediction of key performance indicators in the design process, reducing the computational cost and allowing for a simultaneous optimization in multi-topology scenarios [124, 125]. Robust designs can be obtained when considering uncertainties in the parameters during the optimization process. For robust machine optimization methods, see, e.g., [22, 25, 102]. In [87] an efficient method for the consideration of uncertain parameters is introduced, which

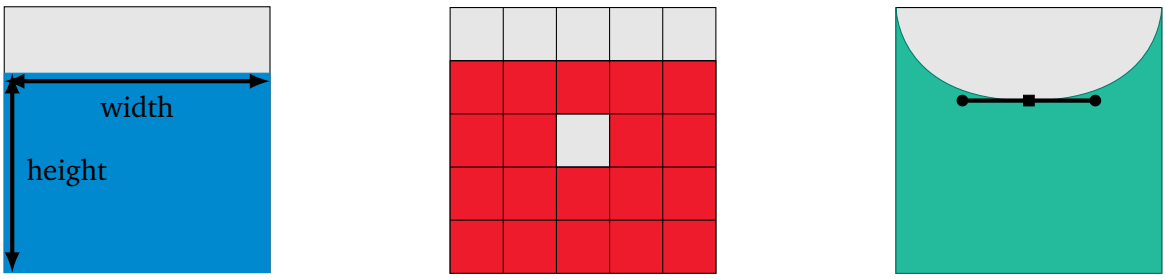

(a) Parameter optimization **(b)** Topology optimization **(c)** Shape optimization

Figure 5.1: Types of structural optimization based on [104]. Taken from [162].

uses a surrogate model based on Gaussian process regression for the approximation of the quantities of interest. Recently, gradient based freeform shape optimization based on shape calculus has been investigated for the (multi-objective) optimization of electric machines [70], where automated shape differentiation [74, 166] can be applied. In this chapter, we introduce a method for freeform shape optimization using IGA.

5.1 Shape Optimization with Isogeometric Analysis

Since in the case of IGA, the shape of a geometry can easily and smoothly be transformed as explained in Section 3.2.2, it is highly suitable for shape optimization [73, 114]. Moving the control points allows for a straightforward modification of the shape, eliminating the need for remeshing. For gradient-based shape optimization, there are two basic approaches: *discretize first – optimize then* and *optimize first – discretize then* [69]. The *discretize first* approach obtains the shape sensitivities by differentiation of the objective function on a discretized level with respect to the control points, see, e.g. [81, 129]. This approach has been applied in [162], where a rotating magnetocaloric cooling device, discretized with IGA is optimized, based on differentiation with respect to the control points. In the *optimize first* approach, the sensitivity with respect to a given transformation is computed on a continuous level using shape calculus [52, 69]. While in the context of shape optimization, the shape derivative is employed to find a shape gradient, i.e., a descent direction, a related approach has been used in [166], where the sensitivity with respect to a given transformation is used to compute derivatives of the discrete system matrices to facilitate mode tracking [92] for electromagnetic cavities. In [69] it has been shown that, in the case of IGA for certain assumptions, the two approaches yield the same (discretized) derivatives. In this chapter, following [114], we aim to optimize the shape of rotating electric machines discretized with IGA, using freeform shape optimization based on shape calculus, i.e., we use the *optimize first* approach. Shape sensitivity analysis is used to obtain the shape derivative of an objective function which quantifies the local sensitivity of that objective with respect to a change of the geometry. The shape derivative can then be used to perform a gradient-based freeform shape optimization.

5.2 Shape Sensitivity Analysis

The sensitivity of a functional $\mathcal{J} = \mathcal{J}(\Omega^S)$ depending on the shape Ω^S of the domain with respect of a perturbation of the shape Ω^S in the direction of a vector field $\mathbf{W}$ is described by the shape derivative $d\mathcal{J}(\Omega^S; \mathbf{W})$. Formally, the shape derivative can be defined as

$$d\mathcal{J}(\Omega^S; \mathbf{W}) = \lim_{\delta \searrow 0} \frac{\mathcal{J}(T_\delta^{\mathbf{W}}(\Omega^S)) - \mathcal{J}(\Omega^S)}{\delta}, \tag{5.1}$$

if this limit exists and the mapping $\mathbf{W} \mapsto d\mathcal{J}(\Omega^S; \mathbf{W})$ is linear and continuous on the space of smooth vector fields. Here, $T_\delta^{\mathbf{W}}(\mathbf{x}) = \mathbf{x} + \delta\mathbf{W}(\mathbf{x})$ describes a transformation that moves every point $\mathbf{x}$ in the direction of the vector field $\mathbf{W}$ by a small distance $\delta > 0$. If this shape derivative of the objective function is known, it can be used to find a vector field $\mathbf{W}$ to manipulate the geometry in order to minimize the value of the objective function and, therefore, leads to an optimized geometry.

To derive the shape derivative of an objective function $\mathcal{J}(\Omega^S)$, we first have to define our optimization problem.

5.2.1 Optimization Problem

For the optimization of electric machines, we restrict ourselves to the two-dimensional approximation, as this drastically reduces the computational effort when solving the numerical problem in comparison to the three-dimensional problem. As objective of the optimization, we choose to minimize the THD of the EMF introduced in Section 2.3.3. We will apply this optimization to the three-phase interior permanent magnet synchronous machine (IPMSM) that will be described in detail in Section 6.1. The periodicity of the stator windings allows us to only optimize the EMF in one of the three phase windings. We will therefore denote $\mathcal{E} := \mathcal{E}_1$ and $\chi = \chi_1$ in the following. Note that the EMF implicitly depends on the shape Ω^S as it depends on the solution of (2.33)–(2.35), which in turn depends on the shape. The solution of (2.33)–(2.35) also always depends on the rotor angle α, which depends on the time t, e.g., by the equation of motion. Thus, we obtain the dependencies $\mathcal{E} = \mathcal{E}(A(\alpha(t), \Omega^S))$, where A is the z-component of the magnetic vector potential. The optimization problem can then be stated as

$$\min_{\Omega^S \in \mathcal{A}} \mathcal{J}(\Omega^S) := \mathrm{THD}_{\mathcal{I}}(\mathcal{E}(A(t, \Omega^S))), \tag{5.2}$$

$$\text{s.t.} \quad c(\Omega^S) = 0, \tag{5.3}$$

where $\mathcal{A}$ is the set of admissible geometries, $c(\Omega^S)$ are physical constraints and the optimization problem (5.2) and (5.3) is constrained by the machine model (2.33)–(2.35). As explained in Section 3.1.1, the problem in its weak formulation for $t \in [0, T]$ with the electrical period length $T = 2\pi/\omega$ and electric angular frequency ω, reads: Find $A = A(\alpha(t)) \in U$ such that

$$\underbrace{\int_\Omega \nu_{\Omega^S}(\alpha(t)) \nabla A \cdot \nabla v \, \mathrm{d}\Omega}_{=: a[\alpha(t)](\Omega^S; A, v)} = \langle r(t, \alpha(t)), v \rangle \tag{5.4}$$

for all test functions $v \in V$, where we define the bilinear form $a[\alpha(t)](\Omega^S; A, v)$ and the right-hand side is given by

$$\langle r(t, \alpha(t)), v \rangle = \int_{\Omega_\mathrm{c}} \sum_{k=1}^{3} \chi_k(x, y) i_k(t) \, v(x, y) \, \mathrm{d}\Omega_\mathrm{c} + \int_{\Omega_{\mathrm{pm}}(\alpha(t))} \mathbf{M}^\perp \cdot \nabla v(x, y) \, \mathrm{d}\Omega_{\mathrm{pm}}(\alpha(t)) \tag{5.5}$$

and both A and v fulfill homogeneous BCs. The right-hand side (5.5) describes the excitation due to the magnetization of the permanent magnets in the permanent magnet region $\Omega_{\mathrm{pm}}(\alpha(t))$ which depends on the rotor angle and due to the currents in the windings in the coil region Ω_c. Here, for a more compact notation we used that the coils are only located in the stator and the permanent magnets are only located in the rotor for the considered machine type, but the formulation can easily be extended for other machine types.

As we want to consider rotating machines, we introduce a discretization into N_α points in time $\{t_1, \dots, t_{N_\alpha}\}$ and the corresponding rotor angles $\boldsymbol{\alpha} := (\alpha_1, \dots, \alpha_{N_\alpha})$. For a given shape Ω^S and $j \in \{1, \dots, N_\alpha\}$, we use the shortened notation $a_j(\Omega^S; \star, \star) := a[\alpha_j](\Omega^S; \star, \star)$ and $r_j := r(t_j, \alpha_j)$, using the definitions from (5.4)

and (5.5). Approximating $A(t, \Omega^S)$ for $t \in [0, T]$ by $\{A_1, \dots, A_{N_\alpha}\}$ and introducing the notation for the objective function as $\mathcal{J}(A_1, \dots, A_{N_\alpha}) \coloneqq \mathrm{THD}_{\mathcal{I}}(\mathcal{E}(A_1, \dots, A_{N_\alpha}))$, after the discretization with respect to the rotor positions, problem (5.2)–(5.4) can be written as the optimization problem

$$\min_{\Omega^S} \mathcal{J}(A_1, \dots, A_{N_\alpha}) \tag{5.6}$$

$$\begin{cases} a_1(\Omega^S; A_1, v_1) = \langle r_1, v_1 \rangle \ \forall v_1, \\ \vdots \\ a_{N_\alpha}(\Omega^S; A_{N_\alpha}, v_{N_\alpha}) = \langle r_{N_\alpha}, v_{N_\alpha} \rangle \ \forall v_{N_\alpha}, \\ c(\Omega^S) = 0, \end{cases} \tag{5.7}$$

which is constrained by N_α boundary value problems corresponding to the N_α considered rotor positions.

5.2.2 Shape Derivative

The shape derivative $d\mathcal{J}(\Omega^S; \mathbf{W})$ for the optimization problem (5.6) and (5.7) can be calculated following the steps taken in [71]. For the derivation, we introduce the Lagrangian

$$\mathcal{L}(\Omega^S, \varphi_1, \dots, \varphi_{N_\alpha}, \psi_1, \dots, \psi_{N_\alpha}) \coloneqq \mathcal{J}(\varphi_1, \dots, \varphi_{N_\alpha}) + \sum_{k=1}^{N_\alpha} \left(a_k(\varphi_k, \psi_k) - \langle r_k, \psi_k \rangle \right). \tag{5.8}$$

For ease of notation, we will denote the dependencies $\mathbf{A} = (A_1, \dots, A_{N_\alpha})$, not to be confused with the 3D vector potential, and similar for other quantities. For each A_i satisfying the i-th PDE of (5.7), it holds that

$$\frac{\partial}{\partial \psi_i} \mathcal{L}(\Omega^S, \mathbf{A}, \boldsymbol{\psi})(q_i) = a_i(A_i, q_i) - \langle r_i, q_i \rangle = 0$$

for all test functions q_i. Similarly, we introduce the adjoint states p_i, $i = 1, \dots, N_\alpha$, as the solutions to the problem

$$0 = \frac{\partial}{\partial \varphi_i} \mathcal{L}(\Omega^S, \mathbf{A}, \mathbf{p})(v_i) = \frac{\partial \mathcal{J}}{\partial \varphi_i}(\mathbf{A})(v_i) + a_i(v_i, p_i) \tag{5.9}$$

for all test functions v_i.

We now consider the objective function $\mathcal{J}(A_1, \dots, A_{N_\alpha}) = \mathrm{THD}_{\mathcal{I}}(\mathcal{E}(A_1, \dots, A_{N_\alpha}))$ more closely. For the calculation of the THD of the EMF, we require the time-derivative of the flux linkage. Using the Fourier representation of the flux linkage

$$\Psi(A_1, \dots, A_{N_\alpha}) = \sum_{k=-\lfloor N_\alpha/2 \rfloor}^{\lfloor N_\alpha/2 \rfloor} \mathcal{C}_k e^{\imath k t}, \tag{5.10}$$

with the Fourier coefficients $(\mathcal{C}_k)_{k\in\mathcal{I}}$ and $\lfloor\star\rfloor$ denoting the floor function and by differentiating the Fourier series with respect to t, the EMF can be written according to (2.45) as

$$\mathcal{E}(A_1,\dots,A_{N_\alpha}) = \sum_{k=-\lfloor N_\alpha/2\rfloor}^{\lfloor N_\alpha/2\rfloor} \underbrace{\imath k \mathcal{C}_k}_{c_k} e^{\imath k t}, \tag{5.11}$$

where $(c_k)_{k\in\mathcal{I}}$ are the Fourier coefficients of the EMF $\mathcal{E}$. To compute the THD we choose the representation (2.49) using the coefficients in of the Fourier series in sin-cos-form [128]. The Fourier series (5.11) can be rewritten equivalently as

$$\mathcal{E}(A_1,\dots,A_{N_\alpha}) = \frac{\mathcal{A}_0}{2} + \sum_{k=1}^{\lfloor N_\alpha/2\rfloor} \mathcal{A}_k \cos(kt) + \mathcal{B}_k \sin(kt). \tag{5.12}$$

The coefficients $\mathcal{A}_k$ and $\mathcal{B}_k$ of the Fourier representation of $\mathcal{E} = \partial_t \Psi$ from (5.12) are obtained by Fourier transform and time derivation, which we will denote by

$$\mathcal{A}_k = [\mathcal{F}_a'(\Psi(u_1,\dots,u_{N_\alpha}))]_k \qquad \text{and} \qquad \mathcal{B}_k = [\mathcal{F}_b'(\Psi(u_1,\dots,u_{N_\alpha}))]_k, \tag{5.13}$$

respectively. The linearity of the discrete Fourier transform can be exploited to write the vectors of Fourier coefficients in terms of transformation matrices $\mathbf{M}_a = \mathcal{F}_a'(\mathbf{I})$ and $\mathbf{M}_b = \mathcal{F}_b'(\mathbf{I})$, where $\mathbf{I}$ is the identity matrix, i.e.,

$$\mathcal{A}_{k-1}(A_1,\dots,A_{N_\alpha}) = \sum_{j=1}^{N_\alpha} \left((\mathbf{M}_a)_{k,j} N_p L \int_\Omega \chi A_j \ \mathrm{d}\Omega \right), \tag{5.14}$$

$$\mathcal{B}_{k-1}(A_1,\dots,A_{N_\alpha}) = \sum_{j=1}^{N_\alpha} \left((\mathbf{M}_b)_{k,j} N_p L \int_\Omega \chi A_j \ \mathrm{d}\Omega \right), \tag{5.15}$$

where L is the length of the machine in z-direction.

To obtain the adjoint states by solving the adjoint state equation (5.9), the objective function $\mathcal{J} = \mathrm{THD}(\mathcal{E}(A_1,\dots,A_{N_\alpha}))$ has to be differentiated with respect to A_i for $i \in \{1,\dots,N_\alpha\}$. Using the definitions of the THD (2.51), we obtain

$$\begin{aligned} &\frac{\mathrm{d}\ \mathrm{THD}(\mathcal{E}(\mathbf{A}))}{\mathrm{d}A_i}(\mathbf{A})(v_i) = \\ &\frac{1}{\sqrt{\mathcal{A}_1^2+\mathcal{B}_1^2}} \frac{1}{\sqrt{\sum_{k\in\mathcal{I},k\neq 1} \mathcal{A}_k^2+\mathcal{B}_k^2}} \left(\sum_{k\in\mathcal{I},k\neq 1} \mathcal{A}_k\mathcal{A}_k' + \mathcal{B}_k\mathcal{B}_k' \right) \\ &- \frac{1}{(\mathcal{A}_1^2+\mathcal{B}_1^2)^{3/2}} \left(\sqrt{\sum_{k\in\mathcal{I},k\neq 1} \mathcal{A}_k^2+\mathcal{B}_k^2} \, (\mathcal{A}_1\mathcal{A}_1' + \mathcal{B}_1\mathcal{B}_1') \right), \end{aligned} \tag{5.16}$$

where we used the abbreviations $\mathcal{A}_k' := \frac{\mathrm{d}\mathcal{A}_k}{\mathrm{d}A_i}(\mathbf{A})(v_i)$ and $\mathcal{B}_k' := \frac{\mathrm{d}\mathcal{B}_k}{\mathrm{d}A_i}(\mathbf{A})(v_i)$. It can be seen from (5.14) and (5.15) that

$$\frac{\mathrm{d}\mathcal{A}_k}{\mathrm{d}A_i}(\mathbf{A})(v_i) = (\mathbf{M}_a)_{k,i} N_p L \int_\Omega \chi v_i \ \mathrm{d}\Omega, \tag{5.17}$$

$$\frac{\mathrm{d}\mathcal{B}_k}{\mathrm{d}A_i}(\mathbf{A})(v_i) = (\mathbf{M}_b)_{k,i} N_p L \int_\Omega \chi v_i \ \mathrm{d}\Omega. \tag{5.18}$$

Given the solutions to the forward problem (5.4) for all rotor positions $i \in \{1, \dots N_\alpha\}$, the adjoint problem (5.9) defining the adjoint variable at rotor position $i \in \{1, \dots N_\alpha\}$ is given as: Find p_i such that

$$a_i(v_i, p_i) = -\frac{\mathrm{d}\ \mathrm{THD}(\mathcal{E}(\mathbf{A}))}{\mathrm{d}A_i}(\mathbf{A})(v_i)$$

for all test functions v_i.

Similarly as proposed in [71], aim to allow shape deformations only within the rotor, excluding the permanent magnets. Therefore, we assume the deformation vector field $\mathbf{W}$ to vanish on the interface Γ_{int}, the permanent magnet region and in the stator. We then obtain the shape derivative in the direction of a smooth vector field $\mathbf{W}$ as

$$\begin{aligned} d\mathcal{J}(\Omega^S; \mathbf{W}) = &\sum_{l=1}^{N_\alpha} \int_{\Omega_{\text{pm}}} (\nabla \cdot \mathbf{W}\mathbf{I} - \mathrm{d}\mathbf{W}^\top)\nabla p_l \cdot \mathbf{M}^\perp \ \mathrm{d}\Omega \\ &+ \sum_{l=1}^{N_\alpha} \int_\Omega \nu(\nabla \cdot \mathbf{W}\,\mathbf{I} - \mathrm{d}\mathbf{W}^\top - \mathrm{d}\mathbf{W})\nabla u_l \cdot \nabla p_l \ \mathrm{d}\Omega. \end{aligned} \tag{5.19}$$

Here, $\mathbf{I} \in \mathbb{R}^{2\times 2}$ denotes the two-dimensional identity matrix and $\mathrm{d}\mathbf{W}$ denotes the Jacobian of the vector field $\mathbf{W}$.

5.2.3 Numerical Shape Optimization

For the optimization of the rotor shape according to problem (5.2) and (5.3) we propose to use a gradient-based optimization method, which involves the shape derivative (5.19). The augmented Lagrangian method [122, 147] can be used to incorporate constraints (5.3). This is achieved by means of augmenting the objective function by terms involving the constraint $c(\Omega^S)$ with suitably updated coefficients. A shape gradient $\mathbf{W}$ can be computed by solving the auxiliary boundary value problem

$$b(\mathbf{W}, \mathbf{Z}) = d\mathcal{J}(\Omega^S; \mathbf{Z}) \quad \forall \mathbf{Z} \tag{5.20}$$

where $b(\star, \star)$ is a positive definite bilinear form satisfying $b(\mathbf{Z}, \mathbf{Z}) > 0$ for all vector fields $\mathbf{Z}$. Thus, the obtained shape gradient is also positive, i.e., $d\mathcal{J}(\Omega^S; \mathbf{W}) = b(\mathbf{W}, \mathbf{W}) > 0$ and due to the linearity of $d\mathcal{J}(\Omega^S; \mathbf{W})$, the negative shape gradient satisfies $d\mathcal{J}(\Omega^S; -\mathbf{W}) < 0$. Therefore, moving all control points of the geometry a small distance δ into the direction of $\mathbf{W}$ will increase the value of the objective function, whereas moving all control points in the direction of $-\mathbf{W}$ will lead to a decrease of the objective function. This is true for any positive definite bilinear form $b(\star, \star)$. The choice of the bilinear form affects the metric of the shape gradient, i.e., different choices for b lead to different shape gradients, which are all deformation vector fields that lead to a decrease of $\mathcal{J}$. The auxiliary boundary value problem (5.20) can also be interpreted as finding a Riesz representative $\mathbf{W}$ of the functional $d\mathcal{J}(\Omega^S, \cdot)$ with respect to the metric given by $b(\star, \star)$. For the bilinear form for the auxiliary problem (5.20) we choose

$$b(\mathbf{W}, \mathbf{Z}) = \int_\Omega \mathrm{d}\mathbf{W} : \mathrm{d}\mathbf{Z} + \mathbf{W} \cdot \mathbf{Z} \ \mathrm{d}\Omega, \tag{5.21}$$

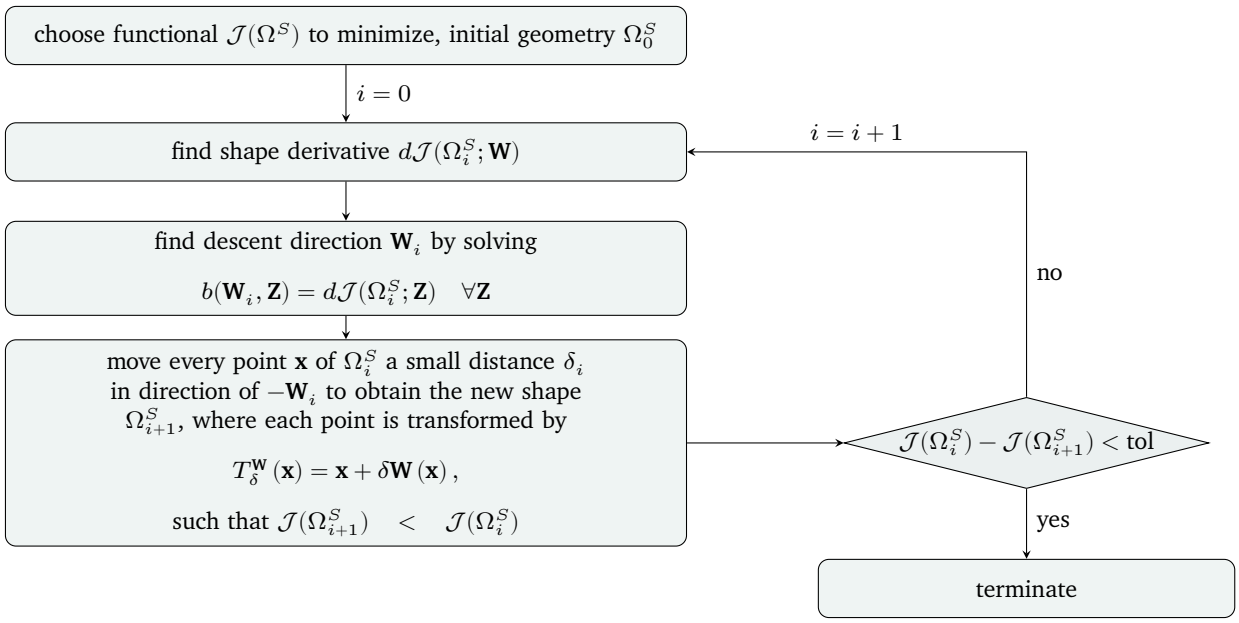

Figure 5.2: Overview of the unconstrained shape optimization algorithm. Taken from [114] ©2021 IEEE.

where we denote by $\mathbf{A} : \mathbf{B} = \sum_{i,j=1}^{n} A_{ij} B_{ij}$ the Frobenius inner product of two matrices $\mathbf{A}, \mathbf{B} \in \mathbb{R}^{n \times n}$ and d$\mathbf{W}$, d$\mathbf{Z}$ denote the Jacobians of $\mathbf{W}$, $\mathbf{Z}$, respectively.

The algorithm for the shape optimization can thus be outlined as follows: We iteratively compute a descent vector field by solving the auxiliary problem (5.20) where the bilinear form $b(\star, \star)$ is given by (5.21). The obtained descent direction is then used to move all control points of the geometry by a small distance δ in the obtained direction. An appropriate step size δ can be found, e.g., by a line search. In our case we choose δ as the maximum of the set $\{1, 1/2, 1/4, \dots\}$ such that, no intersections of the geometry patches occur and the value of the objective function is decreased. This procedure is repeated until no further improvement can be achieved. In this case, the algorithm terminates. An overview of the algorithm is visualized in Fig. 5.2. It can straightforwardly be incorporated into existing CAD workflows thanks to the capability of IGA to operate directly on CAD geometries and the fact that the output of the optimization process is also given as a CAD model. The post-processing can then be carried out directly on the optimized machine. An illustration of the incorporation of the proposed shape optimization workflow into the design process of electric machines is shown in Fig. 5.3.

5.3 Summary

In this chapter, we proposed a method for the gradient-based optimization of the shape of an electric machine using the concept of shape sensitivity analysis. We have formally stated the optimization problem, which is constrained by the partial differential equation (PDE) that characterizes the machine. As an objective function that we aim to minimize, we choose the total harmonic distortion (THD) of the electromotive force (EMF). This objective function takes rotation of the machine into account such that efficient methods for the simulation of rotating machines, such as the methods presented in the previous chapter, become crucial.

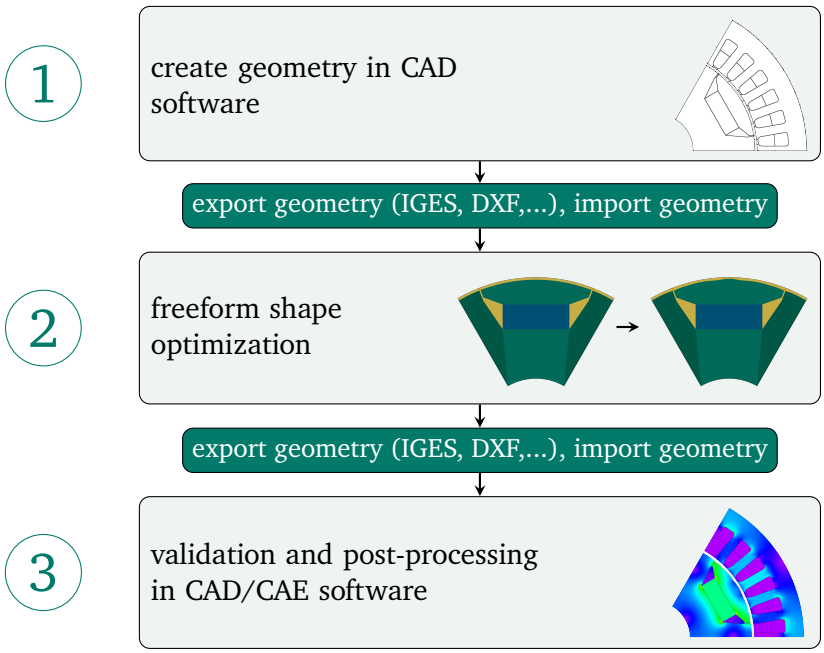

Figure 5.3: Incorporation of IGA freeform shape optimization into the design workflow of electric machines.

We derived the shape derivative of the objective function based on the adjoint problem. The shape derivative can be employed to determine a shape gradient, i.e., a descent direction given as a vector field in the geometry. By adjusting the shape towards the obtained descent direction, the objective function can be decreased. Modifying the shape in a given direction can be easily achieved in isogeometric analysis (IGA) by moving the control points of the geometry. This makes isogeometric analysis (IGA) particularly well-suited for this method of shape optimization.

Finally, we presented an algorithm that can be used for the numerical shape optimization combining the aforementioned findings. This approach is straightforwardly incorporated in the CAD-based design workflow and offers a to be promising method for optimizing the shape of electric machines. The method can be applied for other optimization objectives by deriving the shape derivative of the respective function.

6 Numerical Applications and Results

The methods described for the simulation and optimization in this work are applied to a six-pole IPMSM. All computations are carried out in Octave/Matlab® [62, 108] using the GeoPDEs package [155] as an IGA implementation for the discretization and solution. We start by introducing a toy problem (unit cube) and more realistic IPMSM model (2D and 3D) before we discuss the application of the various methods and their results in the subsequent sections.

6.1 Models

Unit Cube with Manufactured Solution For the investigation of convergence of the proposed methods, we use a test problem with a known closed-form solution. We solve the magnetostatic source problem (see Section 2.3.1) on the domains shown in Fig. 6.3 with periodic BCs in x-direction and homogeneous Dirichlet BCs on all other boundaries. The excitation is chosen such that we obtain the manufactured solution

$$\mathbf{A}_{\text{src}}(x,y,z) = \begin{bmatrix} \sin(y)\sin\left(\frac{z}{2}\right) \\ \sin(x)\sin\left(\frac{z}{2}\right) \\ \sin(x)\sin(y) \end{bmatrix}. \tag{6.1}$$

This magnetic vector potential leads to the magnetic flux density

$$\mathbf{B}_{\text{ana}}(x,y,z) = \begin{bmatrix} \sin(x)\cos(y) - \frac{1}{2}\left(\sin(x)\cos\left(\frac{z}{2}\right)\right) \\ -\cos(x)\sin(y) + \frac{1}{2}\left(\sin(y)\cos\left(\frac{z}{2}\right)\right) \\ \cos(x)\sin\left(\frac{z}{2}\right) - \cos(y)\sin\left(\frac{z}{2}\right) \end{bmatrix}, \tag{6.2}$$

which is independent of the gauging and is induced by the electric current density and magnetization

$$\mathbf{J}_{\text{src}}(x,y,z) = \begin{bmatrix} \frac{5}{4}\sin(y)\sin\left(\frac{z}{2}\right) \\ \frac{5}{4}\sin(x)\sin\left(\frac{z}{2}\right) \\ 2\sin(x)\sin(y) \end{bmatrix}, \tag{6.3}$$

$$\mathbf{M}(x,y,z) = \mathbf{0}. \tag{6.4}$$

The magnetic flux density (6.2) in the conforming and non-conforming configurations is visualized in Fig. 6.1. For the investigation of the convergence, we compute the relative error

$$\epsilon = \frac{\sqrt{\int_\Omega |\mathbf{B}_{\text{num}} - \mathbf{B}_{\text{ana}}|^2 \,\mathrm{d}\,V}}{\sqrt{\int_\Omega |\mathbf{B}_{\text{ana}}|^2 \,\mathrm{d}\,V}} \tag{6.5}$$

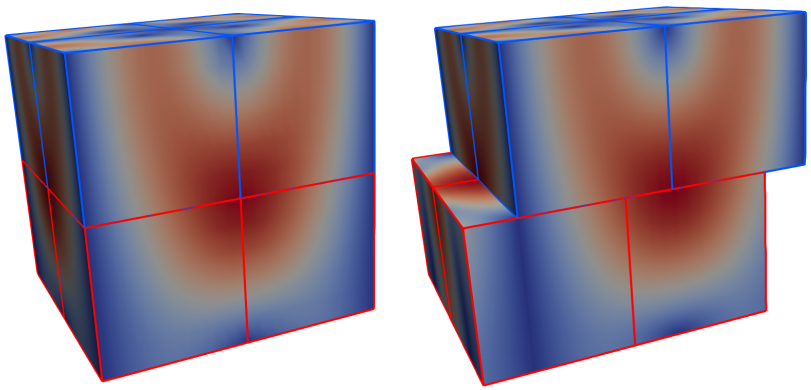

Figure 6.1: Magnitude $|\mathbf{B}|$ of the magnetic flux density of the test problem, normalized for the visualization.

in the domain $\Omega = \overline{\Omega}_1 \cup \overline{\Omega}_2$ of the numerically computed magnetic flux density $\mathbf{B}_{\text{num}}$ for the conforming and non-conforming discretizations.

Machine Model The machine consists of a rotor with 3 pole pairs with embedded permanent magnets and a stator that has 36 slots for the windings with three electrical phases. The design is derived from a machine that was originally designed as part of a tool machine [123, page 124]. The parameters for the geometry and materials of the machine have been taken from [22, Chapter V.A] and the most important parameters are given in Section 8.2. A visualization of the machine is given in Fig. 6.2. The CAD description of the machine is freely available in IGES format in [113]. Due to the symmetry of the machine, it is sufficient to only consider one pole of the machine with antiperiodic boundary conditions. On the remaining boundaries we set homogeneous Dirichlet BCs.

6.2 Tree-Cotree Gauging for Mortaring

To test the modified Lagrange multiplier space introduced in Section 4.1.1 and the tree-cotree gauging method for mortared spaces, we consider the Maxwell eigenvalue problem (2.21) and the magnetostatic source problem (3.68)–(3.70) for the domains shown in Fig. 6.3.

6.2.1 Inf-sup Stability Condition

The stability of the saddle point problem arising from isogeometric mortaring has been proven to be stable for the Lagrange multiplier space M_h in [32]. In Section 4.1.1, we have introduced the modified multiplier space $\widetilde{M}_h$. To investigate the stability of the problem using this modified space for the Lagrange multipliers, we numerically evaluate the inf-sup constant β for different mesh refinement levels with mesh size h in the parametric domain. The inf-sup constant is evaluated for the domains Fig. 6.3a and Fig. 6.3b with homogeneous Dirichlet BCs on the whole boundary $\partial\Omega$. The inf-sup constant is computed for both the Lagrange multiplier space M_h introduced in [32] and the modified multiplier space $\widetilde{M}_h$ introduced in Section 4.1.1 for different degrees p of the $H(\text{curl};\Omega)$basis functions in the domain. The results are

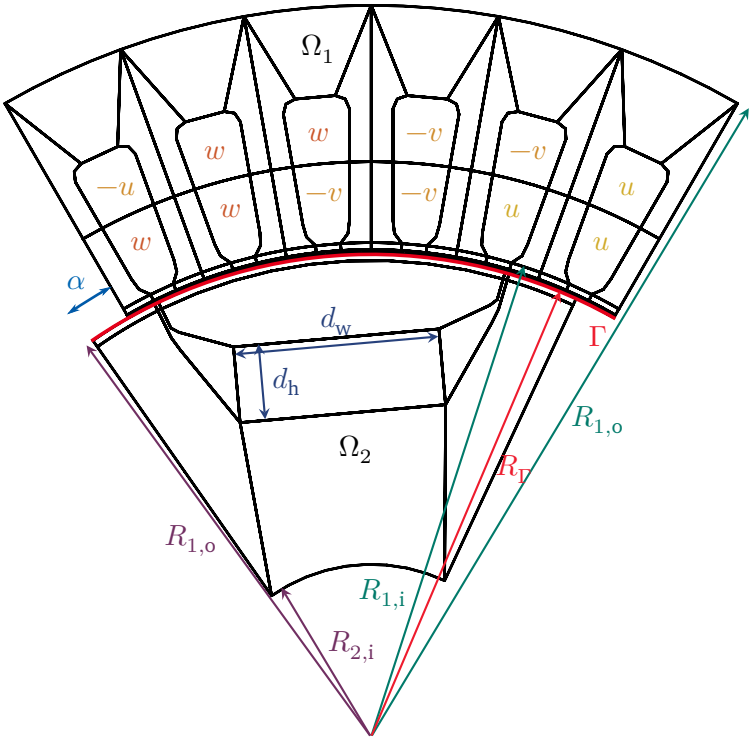

Figure 6.2: Visualization of one pole of the interior permanent magnet synchronous machine (IPMSM) used for the computations. The parameters for the geometry and materials of the machine have been taken from [22, Chapter V.A].

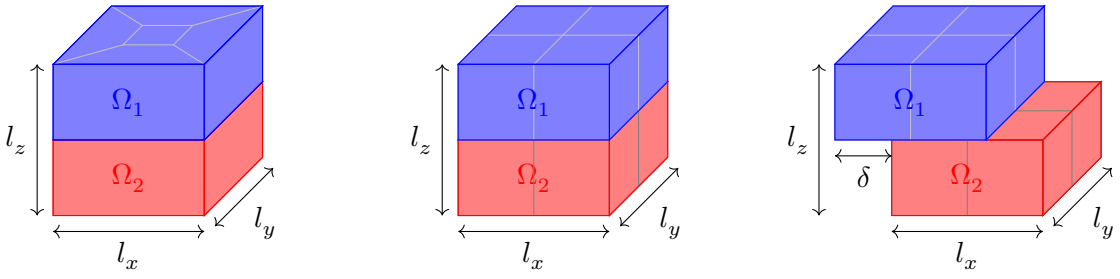

(a) $N_\mathrm{patch} = 5$, conforming patches **(b)** $N_\mathrm{patch} = 4$, conforming patches **(c)** $N_\mathrm{patch} = 4$, non-conforming patches

Figure 6.3: Domain of the test problem with N_patch patches both in Ω_1 and Ω_2 with conforming patches (a,b) and with non-conforming patches (c) where Ω_2 is shifted by δ in x-direction. The parameters of the domain are $l_x = \pi$, $l_y = \pi$, $l_z = \pi$. Taken from [95].

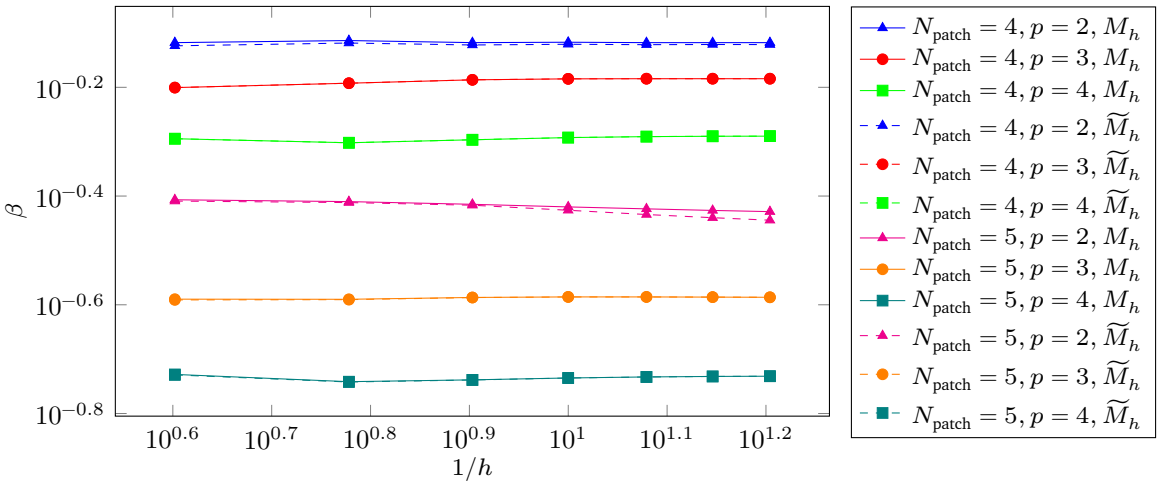

Figure 6.4: Inf-sup constant β for the multi-patch mortaring of the unit cube shown in Fig. 6.3 with N_{patch} patches in each subdomain using M_h and $\widetilde{M}_h$ as space for the Lagrange multipliers for different degree p. Taken from [95].

shown in Fig. 6.4, where we can observe that for both multiplier spaces, the inf-sup constant remains constant and bounded away from zero for increasing refinement levels, confirming the stability of the new multiplier space $\widetilde{M}_h$.

6.2.2 Maxwell Eigenvalue Problem

To numerically confirm that the modified Lagrange multiplier space $\widetilde{M}_h$ is the appropriate choice for mortaring, we investigate the eigenvalues of (2.21) in the domain Fig. 6.3b with Dirichlet BCs, where the eigenvalues are known analytically. The domain contains one internal node on the interface, resulting in one spurious mode when using the original Lagrange multiplier space M_h. When using the modified multiplier space $\widetilde{M}_h$, the computed eigenvalues correspond to those of the exact solution. As an example, for B-spline degree $p = 4$ in both stator and rotor domain Ω_1 and Ω_2, with a discretization consisting of 64 elements gauged using a tree-cotree decomposition [106], the computed eigenvalues are shown in Fig. 6.5 using both, M_h and $\widetilde{M}_h$ as space for the Lagrange multipliers. Here, the spurious eigenvalue which does not correspond to the analytical solution, is marked by a red circle. A few examples of correct eigenmodes of the problem are visualized in Fig. 6.6. An example of a spurious mode that is introduced when using M_h as Lagrange multiplier space is visualized in Fig. 6.7. When using $\widetilde{M}_h$ for the coupling, no spurious modes are introduced. When using isogeometric mortaring with the Lagrange multiplier space M_h, the same number of spurious eigenvalues is introduced as there are interior nodes on the coupling interface of the dependent domain. This is also confirmed when solving the Maxwell eigenvalue problem on the domain Fig. 6.3a, where four spurious modes are introduced.

6.2.3 Magnetostatic Source Problem

To analyze the convergence of the isogeometric mortar method combined with tree-cotree gauging, we solve the magnetostatic source problem (3.68)–(3.70) on the model described in Section 6.1.

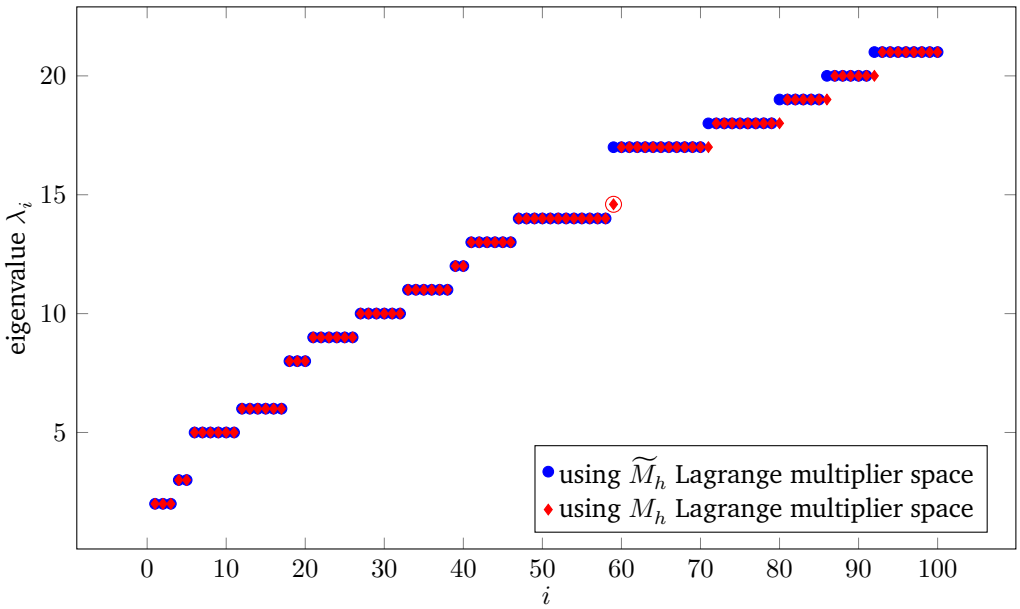

Figure 6.5: Smallest 100 eigenvalues $\lambda_i, i = 1, \dots, 100$ of the Maxwell eigenvalue problem computed with M_h and $\widetilde{M}_h$. The spurious mode is marked with a red circle. The exact eigenvalues are not shown as they correspond to the ones computed with $\widetilde{M}_h$. Taken from [95].

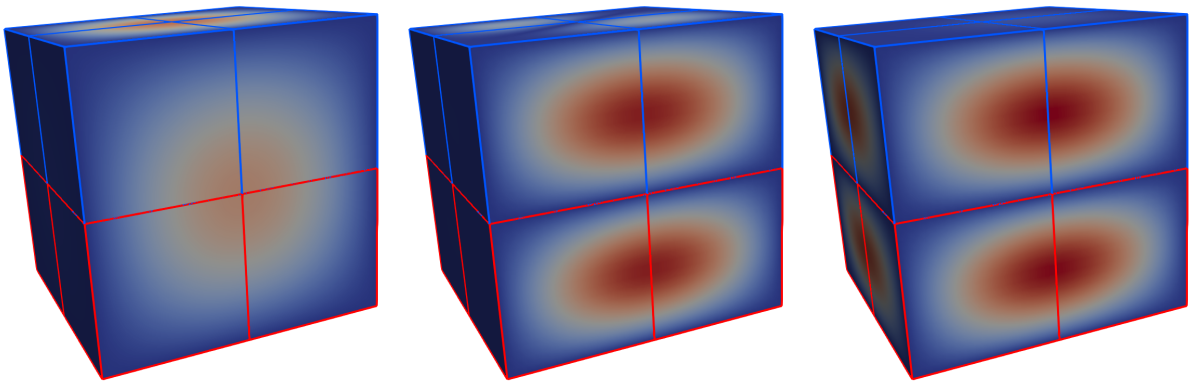

Figure 6.6: Visualization of some eigenmodes of the Maxwell eigenvalue problem.

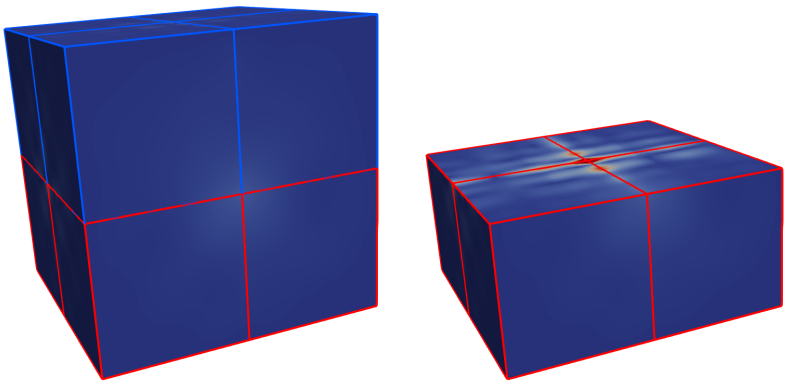

Figure 6.7: Spurious mode introduced when using M_h as space for the Lagrange multiplier.

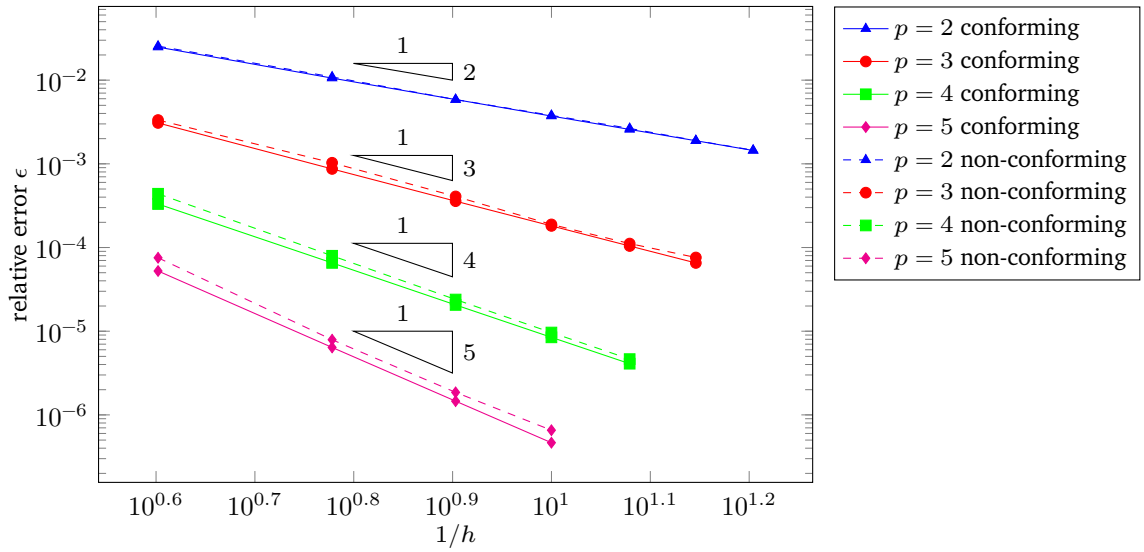

Figure 6.8: Convergence of the relative error ϵ of the magnetic flux density.

The relative error (6.5) from the analytical solution is evaluated for different degrees p of the B-spline basis functions for a conforming and a non-conforming discretization. The results are shown in Fig. 6.8. Here, we use isogeometric mortaring with the modified Lagrange multiplier space $\widetilde{M}_h$ gauged by tree-cotree gauging. For the conforming discretization, we use the multi-patch model shown in Fig. 6.3b. We obtain the non-conforming discretization by shifting Ω_2 by $\delta = 1$ in x-direction, as visualized in Fig. 6.3c.

For both the conforming and non-conforming configurations, we observe that the solution converges with order p, where p is the degree of the $S^1_p(\Omega) \subset H(\text{curl}; \Omega)$ basis functions in the domains Ω_1 and Ω_2.

6.2.4 Electric Machine

Finally, using the isogeometric mortar method described in Section 3.3.1.1 with the enriched Lagrange multiplier space $\widetilde{M}_h$ introduced in Section 4.1.1 and gauging by means of a tree-cotree decomposition for

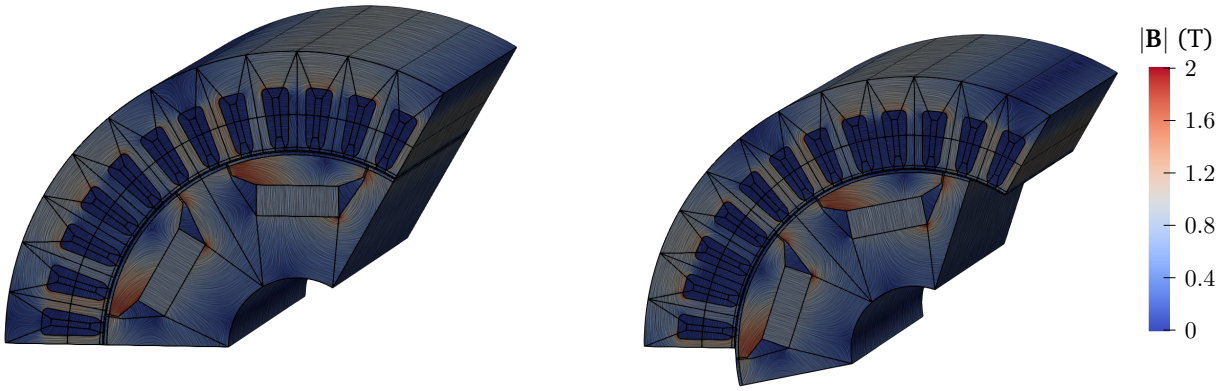

(a) rotation angle $\alpha = 0$ **(b)** rotation angle $\alpha = 13°$

Figure 6.9: Magnetic flux density in two poles of a six pole permanent magnet synchronous machine for different rotation angles. Taken from [95].

mortared spaced as described in Section 4.2.1, we can simulate the full 3D model of an electric machine for arbitrary rotation angles. We apply the previously mentioned methods to the three-dimensional six-pole with the three electric phases u, v, and w PMSM described in Section 6.1. Note that the proposed method is not limited to this application and could also be employed for the simulation of other machine types, e.g., linear motors or axial flux machines or different applications, e.g., eddy current brakes or magnetocaloric cooling devices [162]. The discretization of one pole pair with 24 rotor patches and 228 stator patches leads to a linear system with a total number of $N_{\text{dof}} = 50330$ DoFs, after application of the tree-cotree gauging. Only the coupling matrices $\mathbf{G}$ depend on the rotation angle α. Their assembly only takes about $5\,\%$ of the computational time, and thus, this method allows for a very efficient computation of rotating machines. The creation of the tree and the cotree can be done very efficiently, e.g., with the open source implementation available at [93], which takes less than $2\,\%$ of the computational time. The results of the computation of the magnetic flux density for two different rotation angles is shown in Fig. 6.9.

6.3 Convergence of the Isogeometric Nitsche Coupling

To analyze the convergence and sensitivity of the solution with respect to the Nitsche penalty factor γ of the isogeometric Nitsche-type coupling described in Section 3.3.2, we solve the Nitsche formulation (3.100) on the model problem with a manufactured solution introduced in Section 6.1.

As a first test, we evaluate the relative error of the solution for varying Nitsche penalty factors. We evaluate the error for both the conforming and the non-conforming configurations for basis functions of degree $p = 2, 3, 4$. The result is shown in Fig. 6.10. Our aim is to identify an optimal penalty factor that maximizes the effectiveness of the method without deteriorating the condition of the system or the solution quality. We observe that the Nitsche coupling method works well for a wide range of γ, meaning we have a robust optimal penalty factor.

In the convergence analysis, we set the Nitsche penalty factor to $\gamma = 1 \cdot 10^6$. Here, we observe that the solution converges with the degree of the basis function. The convergence results are depicted in Fig. 6.11.

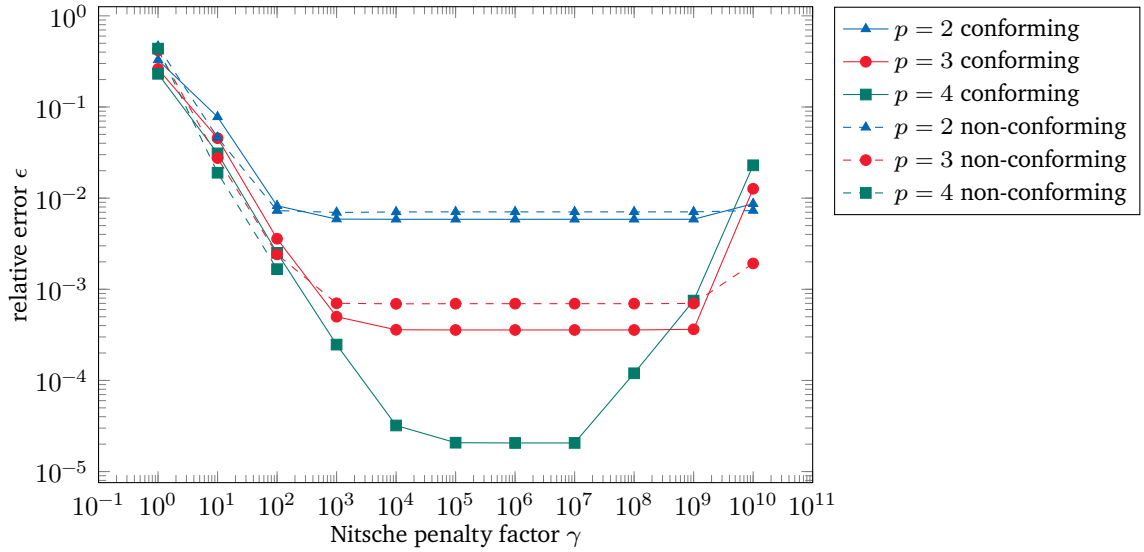

Figure 6.10: Relative error ϵ of the magnetic flux density in the unit cube model for varying Nitsche penalty factor γ.

In this test, we do not observe the loss of one order of convergence that was reported for non-conforming classical FE in [37]. However, one of the disadvantages of the Nitsche mortar method is that the discrete kernel of the resulting system is not yet analyzed. While simple problems can be easily regularized by introducing a small virtual conductivity, this becomes unfeasible for complicated geometries like the full electric machine model, see for example [54]. The investigation of the discrete kernel of the Nitsche system presents an interesting topic for further research.

6.4 Analysis of the Harmonic Coupling Formulation

To illustrate the theoretical results given in Section 4.1.2, the harmonic coupling method described in Section 3.3.1.2 is investigated numerically in terms of inf-sup stability, based on [64]. The reduction to an interface problem is investigated for the case of a rotating machine and the computational time of the full and the reduced problem are compared.

6.4.1 Inf-sup Stability

We use the inf-sup condition (4.13) and following the arguments from [64], we obtain

$$\sup_{v\in V} \frac{\langle \mu, [v] \rangle_{\Gamma_{\text{int}}}}{\|v\|_{H^1(\Omega_1\cup\Omega_2)}} \geq \sup_{z_1\in V_1} \frac{\langle \mu, z_1 \rangle_{\Gamma_{\text{int}}}}{\|z_1\|_{H^1(\Omega_1)}} \geq \beta \|\mu\|_{H^{-1/2}(\Gamma_{\text{int}})}, \tag{6.6}$$

where the spaces are given by $V = \{v \in H^1(\Omega_1 \cup \Omega_2) : v|_{(\partial\Omega_1\cup\partial\Omega_2)\setminus\Gamma_{\text{int}}} = 0\}$ and $V_1 = \{v \in H^1(\Omega_1) : v|_{\partial\Omega_1\setminus\Gamma_{\text{int}}} = 0\}$, and $z_1 \in V_1$ is the weak solution of the mixed boundary value problem

$$-\Delta z_1 = 0 \quad \text{in } \Omega_1 \quad \text{with} \quad z_1 = 0 \quad \text{on } \partial\Omega_1 \setminus \Gamma_{\text{int}} \quad \text{and} \quad \nu \nabla z_1 \cdot \mathbf{n}_\Gamma = \mu \quad \text{on } \Gamma_{\text{int}}. \tag{6.7}$$

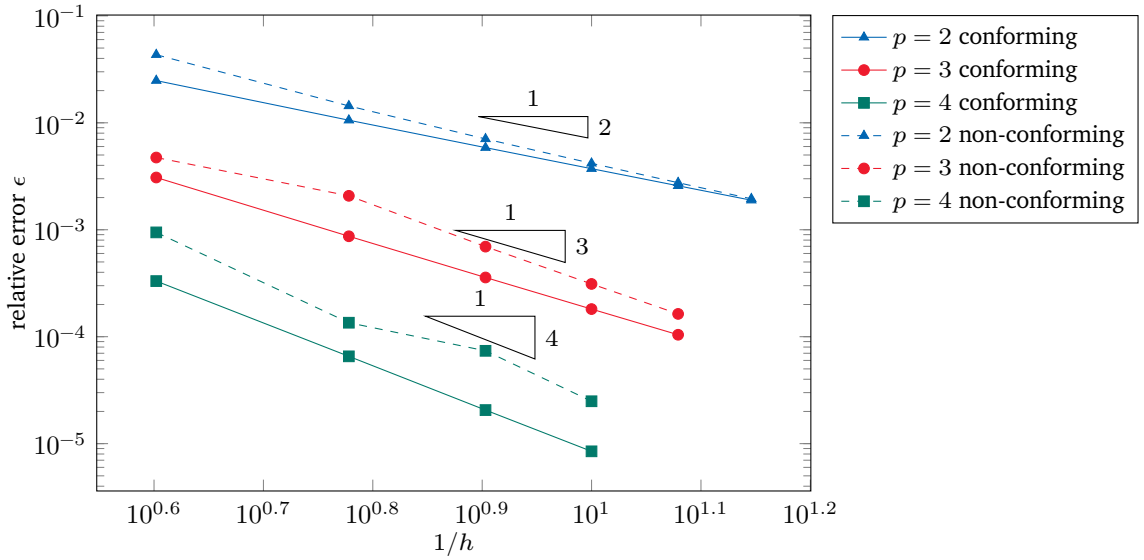

Figure 6.11: Convergence of the relative error ϵ of the magnetic flux density in the unit cube model for the Nitsche method.

Due to the homogeneous Dirichlet BC on $\partial\Omega_1 \setminus \Gamma_{\text{int}}$ the norm on V_1 can be chosen as $\|v_1\|_{H^1(\Omega_1)} = \|\nabla v_1\|_{L^2(\Omega_1)}$ which can be used to show that (6.6) holds for z_1 obtained from (6.7).

For our numerical tests, we use the two-dimensional geometry and patch-discretization of the machine model Fig. 6.2 to compute the inf-sup constant β using (6.6), i.e., on the stator domain Ω_1. The material is assumed constant, i.e., $\nu = 1\,\mathrm{A\,m\,V^{-1}\,s^{-1}}$ on Ω_1, meaning that the domain corresponds to a simple annulus with inner radius $R_1 = 0.0447\,\mathrm{m}$ and outer radius $R_1 = 0.0675\,\mathrm{m}$. For this setting, the solution of (6.7) can be computed analytically and represented by a Fourier series. By defining $S_1\mu := v_1|_{\Gamma_{\text{int}}}$, the largest possible constant β for which the second estimate in (6.6) holds can then be computed as the smallest eigenvalue β of the eigenvalue problem

$$\langle \mu, S_1\tilde{\mu}\rangle_{H^{-1/2}(\Gamma_{\text{int}})\times H^{1/2}(\Gamma_{\text{int}})} = \beta^2(\mu,\tilde{\mu})^2_{H^{-1/2}(\Gamma_{\text{int}})} \qquad \forall \tilde{\mu} \in H^{-1/2}(\Gamma_{\text{int}}). \tag{6.8}$$

For the annulus, β can be computed analytically as

$$\beta = \sqrt{R_1 \ln(R_2/R_1)} \approx 0.13573.$$

In the discrete case, the inf-sup constant is computed by conducting the classical inf-sup test, see, e.g. [39]. As a first test, we solve the corresponding eigenvalue problem for linear basis functions of the solution, i.e., polynomial degree $p = 1$. We start from the coarsest refinement level $\ell = 1$ where we have $n = 144$ polynomial DoFs on the interface Γ_{int} and harmonic order $\leq N$ for the Lagrange multipliers, i.e., the space of harmonic basis functions has the dimension $\dim(M_N) = 2N + 1$. When increasing the refinement level, the number of polynomial DoFs on Γ_{int} is given by $n = 144\ell$. We denote the ratio of harmonic functions and polynomials at the interface by $c = N/n$. For $c = 1/2$ it then holds that

$$\dim(M_N) = 2N + 1 = n + 1 > n, \tag{6.9}$$

thus violating the discrete inf-sup stability condition, cf. (4.18). The numerical results for this test are shown in Table 6.1. The numerical results are in excellent accordance with the theoretical results from

Table 6.1: Discrete inf-sup constants obtained for n polynomial DoFs at the interface Γ_{int} and harmonic order $N = cn$ of the Lagrange multipliers for different refinement levels ℓ and scaling parameters c. The reluctivity is assumed to be $\nu = 1\,\mathrm{A\,m\,V^{-1}\,s^{-1}}$ in the whole domain. Adapted from [64].

	$\ell = 1$	$\ell = 2$	$\ell = 3$	$\ell = 4$
$c = 1/4$	$0.135\,237$	$0.135\,556$	$0.135\,676$	$0.135\,693$
$c = 1/3$	$0.135\,237$	$0.135\,556$	$0.135\,661$	$0.135\,684$
$c = 3/8$	$0.135\,237$	$0.135\,536$	$0.135\,611$	$0.135\,684$
$c = 1/2$	$3.526 \cdot 10^{-8}$	$2.532 \cdot 10^{-8}$	$2.401 \cdot 10^{-8}$	$2.401 \cdot 10^{-8}$

Table 6.2: Discrete inf-sup constants for n spline degrees of freedom on the interface Γ_{int} and harmonic order $N = cn$ of the Lagrange multipliers for polynomial degree k and scaling parameter c. The reluctivity is assumed to be $\nu = 1\,\mathrm{A\,m\,V^{-1}\,s^{-1}}$ in the whole domain. Adapted from [64].

	$p = 2$	$p = 3$	$p = 4$	$p = 5$
$c = 1/4$	$0.135\,721$	$0.135\,723$	$0.135\,723$	$0.135\,723$
$c = 1/3$	$0.135\,721$	$0.135\,722$	$0.135\,723$	$0.135\,723$
$c = 3/8$	$0.135\,720$	$0.135\,723$	$0.135\,723$	$0.135\,723$
$c = 1/2$	$3.652 \cdot 10^{-8}$	0	$8.082 \cdot 10^{-8}$	$1.825 \cdot 10^{-8}$

Section 4.1.2, see (4.18).

In a second test, we vary the polynomial degree p at fixed refinement level $\ell = 2$. Note that n increases with an increase of p, thus for a fixed c, the harmonic order is also increased. The results of this test are summarized in For the scaling parameter $c = 1/2$, the number of Lagrange multipliers again exceeds the number of DoFs on Γ_{int}, violating the discrete inf-sup stability. Again, the results shown in Table 6.2 agree perfectly with the theoretical considerations. As the representation of the test results of Table 6.1 and Table 6.2 might not be apparent, a more obvious representation of the results with more data points is visualized in Fig. 6.12. Here, the x-axis shows the number n of spline DoFs at the interface, whereas the y-axis shows dimension of the Lagrange multiplier space $\dim(M_N)$. Note that (6.9) holds for $\dim(M_N) = n + 1$, thus violating the inf-sup stability condition. We can see that this is supported by the results shown in Fig. 6.12 as the inf-sup constant quickly deteriorates when the dimension of the multiplier space exceeds the dimension of the spline-space at the interface. In Fig. 6.12a, the number of spline DoFs n is increased by refinement, thus corresponding to the results of Table 6.1, whereas the increase of n in Fig. 6.12b is due to an increase to the spline degree, thus corresponding to the results of Table 6.2.

The results shown in Table 6.1 and Table 6.2 were obtained by setting the reluctivity in the whole domain to $\nu = 1\,\mathrm{A\,m\,V^{-1}\,s^{-1}}$. In reality, the stator model consists of air, copper and iron parts. The condition number cannot be computed analytically in this case. However, we can compute the inf-sup constant for an annulus filled completely with air as

$$\beta_{\text{air}} = \sqrt{R_1 \ln(R_2/R_1)/\nu_{\text{air}}} \approx 1.5216 \cdot 10^{-4},$$

and for an annulus filled with iron as

$$\beta_{\text{iron}} = \sqrt{R_1 \ln(R_2/R_1)/\nu_{\text{iron}}} \approx 3.4023 \cdot 10^{-3},$$

where ν_{air} and ν_{iron} are the reluctivities for air and iron, respectively. Assuming air and iron in the whole domain Ω_1 leads to results qualitatively identical to the results above. For the material distribution given in Fig. 6.2, the discrete results for the inf-sup constant for a fixed spline degree $p = 1$ and varying refinement

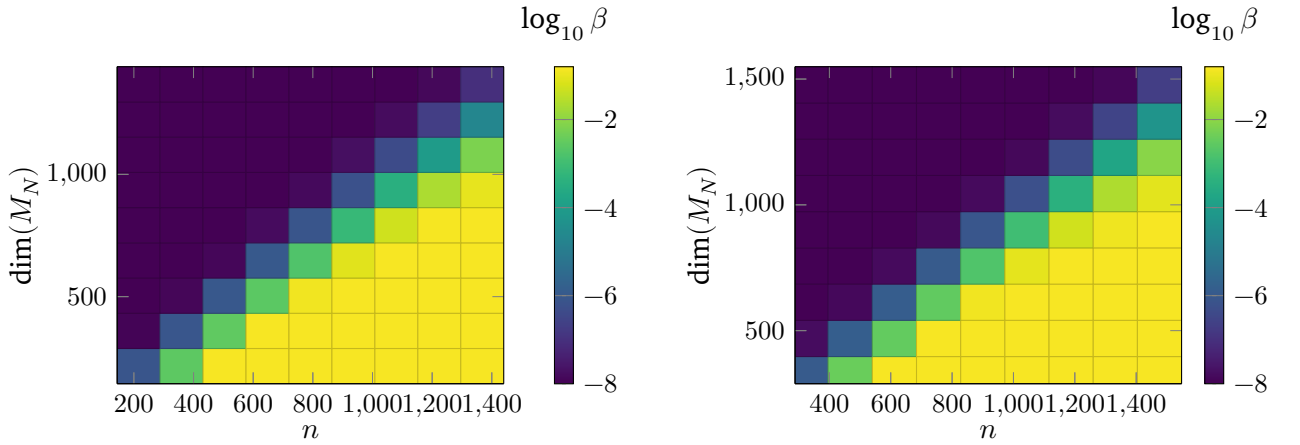

(a) Fixed spline degree $p = 2$, refinement level is increased.

(b) Fixed refinement level $\ell = 2$, spline degree is increased.

Figure 6.12: Discrete inf-sup constant for the annulus with homogeneous material distribution depending on the number of spline DoFs on Γ_{int} and the harmonic order N, where $\dim(M_N) = 2N+1$. The increase of n is due to h-refinement in Fig. 6.12a and p-refinement in Fig. 6.12b.

Table 6.3: Discrete inf-sup constants obtained for n polynomial DoFs at the interface Γ_{int} and harmonic order $N = cn$ of the Lagrange multipliers for different refinement levels ℓ and scaling parameters c. The material distribution is according to Fig. 6.2.

	$\ell = 1$	$\ell = 2$	$\ell = 3$	$\ell = 4$
$c = 1/4$	$1.1729 \cdot 10^{-3}$	$1.1828 \cdot 10^{-3}$	$1.1061 \cdot 10^{-3}$	$1.0875 \cdot 10^{-3}$
$c = 1/3$	$1.0990 \cdot 10^{-3}$	$8.8930 \cdot 10^{-4}$	$7.6250 \cdot 10^{-4}$	$9.6184 \cdot 10^{-4}$
$c = 3/8$	$6.3052 \cdot 10^{-4}$	$4.7592 \cdot 10^{-4}$	$3.7803 \cdot 10^{-4}$	$3.0506 \cdot 10^{-4}$
$c = 1/2$	$1.7443 \cdot 10^{-10}$	$1.7955 \cdot 10^{-10}$	$3.4576 \cdot 10^{-10}$	$1.6688 \cdot 10^{-10}$

Table 6.4: Discrete inf-sup constants for n spline degrees of freedom on the interface Γ_{int} and harmonic order $N = cn$ of the Lagrange multipliers for polynomial degree k and scaling parameter c. The material distribution is according to Fig. 6.2.

	$p = 2$	$p = 3$	$p = 4$	$p = 5$
$c = 1/4$	$1.1599 \cdot 10^{-3}$	$1.1326 \cdot 10^{-3}$	$1.1005 \cdot 10^{-3}$	$1.0745 \cdot 10^{-3}$
$c = 1/3$	$1.0093 \cdot 10^{-3}$	$8.4682 \cdot 10^{-4}$	$7.3828 \cdot 10^{-4}$	$6.1888 \cdot 10^{-4}$
$c = 3/8$	$7.2690 \cdot 10^{-4}$	$5.8481 \cdot 10^{-4}$	$4.6038 \cdot 10^{-4}$	$3.4868 \cdot 10^{-4}$
$c = 1/2$	$1.8049 \cdot 10^{-10}$	$2.3879 \cdot 10^{-10}$	$4.0332 \cdot 10^{-10}$	$2.6105 \cdot 10^{-10}$

levels are shown in Table 6.3. Again, also for the realistic machine model, we can observe that the inf-sup constant deteriorates when the number of harmonics of the Lagrange multiplier space exceeds the number spline DoFs at Γ_{int}. The second test case, where we vary the spline degree p for a fixed refinement level $\ell = 2$, is also conducted with the given material distribution and summarized in Table 6.4. As in the case with a homogeneous material distribution, we can observe that the inf-sup constant goes to zero if the dimension of the Lagrange multiplier space exceeds the number of spline DoFs at the interface. This shows that the theory also holds for the case of our motor geometry. Again, a more obvious visualization of the results with more data points is visualized in Fig. 6.13. The x-axis shows the number n of spline DoFs at the interface, whereas the y-axis shows dimension of the Lagrange multiplier space $\dim(M_N)$. We can see that also for the motor geometry, the inf-sup constant quickly deteriorates when the dimension of

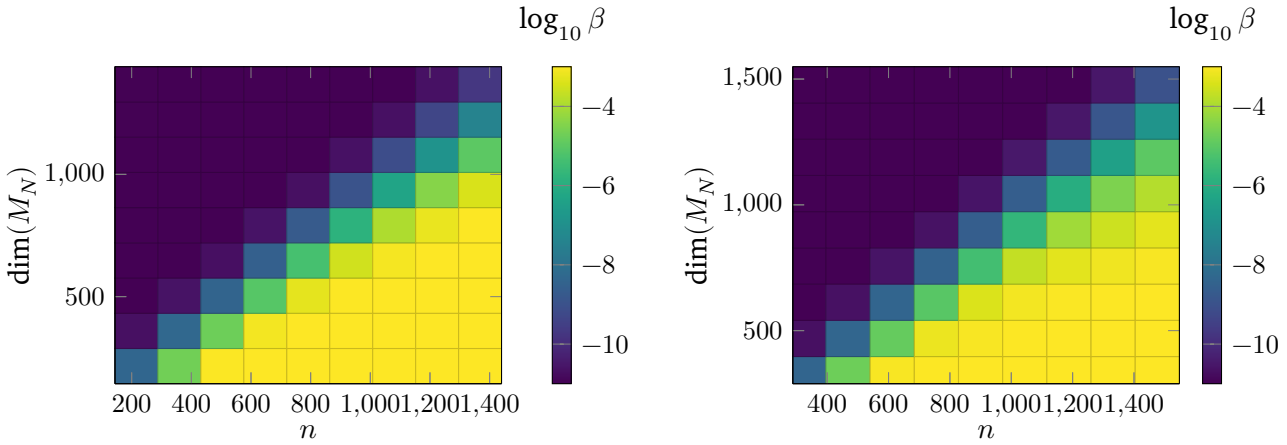

(a) Fixed spline degree $p = 2$, refinement level is increased.

(b) Fixed refinement level $\ell = 2$, spline degree is increased.

Figure 6.13: Discrete inf-sup constant for the motor geometry with inhomogeneous material distribution depending on the number of spline DoFs on Γ_{int} and the harmonic order N, where $\dim(M_N) = 2N + 1$. The increase of n is due to h-refinement in Fig. 6.13a and p-refinement in Fig. 6.13b.

the multiplier space exceeds the dimension of the spline-space at the interface. In Fig. 6.13a, the number of spline DoFs n is increased by refinement, thus corresponding to the results of Table 6.3, whereas the increase of n in Fig. 6.13b is due to an increase to the spline degree, thus corresponding to the results of Table 6.4.

6.4.2 Computational Time for the Interface Problem

When simulating the machine for multiple rotation angles, it can be advantageous to use a Schur complement to obtain a low-dimensional interface problem, as explained in Section 3.3.1.2. To quantify the speedup of solving the interface problem instead over the full problem, we simulate the rotation of a PMSM. We compare the computational cost of simulating a rotor rotation of $120°$, discretized into $N_\alpha = 120$ points in time, using the interface problem to the computational cost of using the full system in Fig. 6.14. As expected, we observe that the computational time required to solve the full system (3.88) depends on the number of the IGA DoFs, whereas the computational time necessary to solve the interface problem (3.95) is nearly independent of the number of IGA DoFs and instead, depends on the number of harmonics used for the coupling. In total, by reducing the system using a Schur complement, the computational time is significantly reduced by a factor of more than two orders of magnitude.

6.5 Torque Computation

In this section, we apply different methods for torque computation to the two- and three-dimensional machine model described in Section 6.1. For our numeric tests, we compute the cogging torque in the

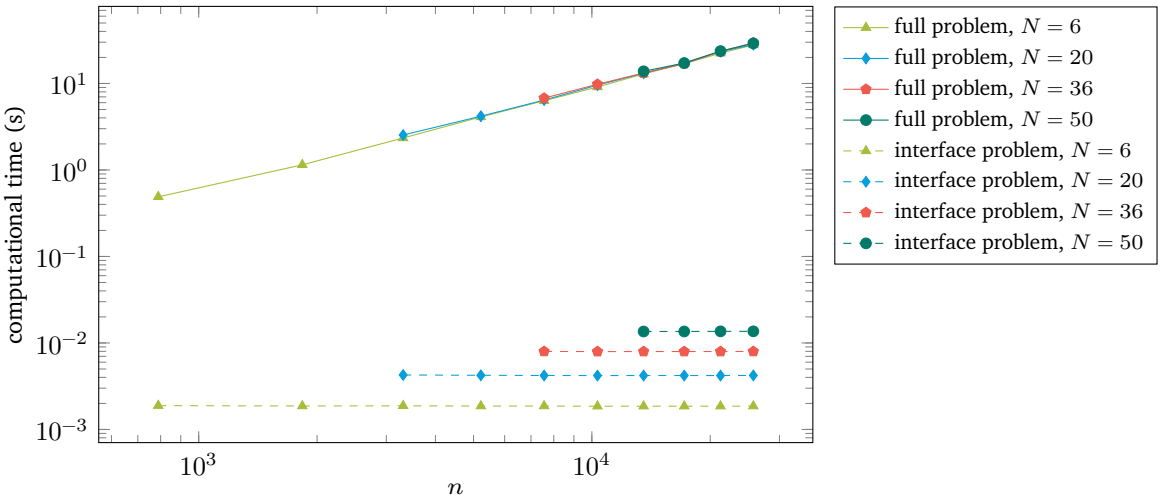

Figure 6.14: Comparison of the computational time of the simulation of a rotating machine by solving the interface problem (3.95) compared to the computational time of the simulation solving the full system (3.88). The rotor is rotated $120°$ using $N_\alpha = 120$ time steps. The simulation is carried out for different spatial refinements and for different trigonometric degrees N for the coupling. The preprocessing, i.e., computing the inverses in (3.96) and (3.97), took at most $0.678\,\mathrm{s}$ in the case of $N = 50$ and $n = 25746$ IGA DoFs and the postprocessing, i.e., (3.98) and (3.99), took at most $1.3012\,\mathrm{s}$. The computation is is repeated 100 times and the computational time is averaged. The computation is carried out in Matlab R2019a on a 6-core machine (Intel® Core™ i7-5820K CPU) with $16\,\mathrm{GB}$ RAM.

absence of excitation currents. The results are compared to an independent reference solution obtained with JMAG® using a finite element discretization.

6.5.1 Torque of the 2D Machine Computed with Harmonic Mortaring

The torque of the PMSM is computed using the explicit formulation (4.35) described in Section 4.3.3, using the coupling matrices and solution vectors obtained from the solution of (3.88). This alleviates the need to evaluate the magnetic field or flux density explicitly by differentiation. Due to the machine length of $L = 0.1\,\mathrm{m}$, the torque has to be scaled by L as mentioned in Section 4.3.3. The computations are carried out on the full machine model which consists of 72 rotor patches and 684 stator patches using B-spline basis functions of degree $p = 1$ and degree $p = 2$. The degree $p = 1$ basis functions correspond to a standard FEM discretization and will be referred to as the FEM solution in the following. However, note that for the geometry mapping, we use the exact NURBS geometry. The B-spline basis functions of degree $p = 2$ with C^1-continuity within the patches and C^0-continuity across patch borders (allowing material discontinuities) will be called the IGA solution in this section. For a better comparability of the solutions for different degrees, we adapt the refinement such that the number of DoFs is comparable for $p = 1$ and $p = 2$. The number of DoFs for $p = 1$ (the FEM case) is $N_{\mathrm{DoF},1} = 39528$ in the stator domain and $N_{\mathrm{DoF},2} = 26532$ in the rotor domain. For $p = 2$ (the IGA case) the number of DoFs is given by $N_{\mathrm{DoF},1} = 37764$ in the stator domain and $N_{\mathrm{DoF},2} = 25140$ in the rotor domain. The IGA reference solution is computed with degree $p = 2$ on a refined mesh leading to $N_{\mathrm{DoF},1} = 128664$ and $N_{\mathrm{DoF},2} = 93360$ degrees of freedom in stator and rotor domain, respectively, and with trigonometric degree $N = 200$. To compute

Table 6.5: Relevant and irrelevant Fourier modes of the Lagrange multipliers of an IGA simulation result for a rotation angle of $\alpha = 7°$, here $|\mathcal{C}_n| = \sqrt{\mathcal{A}_n^2 + \mathcal{B}_n^2}$ is the total amplitude. Taken from [63].

$\lvert\mathcal{C}_3\rvert$	$\lvert\mathcal{C}_9\rvert$	$\lvert\mathcal{C}_{15}\rvert$	$\sum_{n\notin\mathcal{N}}\lvert\mathcal{C}_n\rvert$
$9.2621 \cdot 10^3$	$1.6651 \cdot 10^3$	$5.5848 \cdot 10^3$	$4.9720 \cdot 10^{-6}$

an independent reference solution for the torque, we use JMAG® using a finite element discretization of order $p = 1$ with 1084517 elements. The saddlepoint problem (3.88) is solved efficiently using the Schur complement method described in Section 3.3.1.2.

6.5.1.1 Symmetry of the Solution

As mentioned above, the machine exhibits a $60°$ anti-symmetry. Due to this symmetry, for the Lagrange multiplier

$$\lambda_N(\theta) = \frac{\mathcal{A}_0}{2} + \sum_{n=1}^{N} \mathcal{A}_n \cos(n\theta) + \mathcal{B}_n \sin(n\theta), \tag{6.10}$$

only the coefficients $\mathcal{A}_n$, $\mathcal{B}_n$ with index $n \in \mathcal{N} = \{3, 9, 15, ...\}$ are non-zero. By constructing the mesh such that the symmetry is also preserved on a discrete level, this behavior is also observed for the numerical solution. In Table 6.5 we show the numerically computed Fourier modes for an IGA simulation, where we can see that the sum of all irrelevant modes is negligible compared to the relevant modes and is non-zero only due to numerical errors. In practice, we can reduce the computational cost drastically by only considering one pole of the machine with anti-periodic BCs. For our machine model, this results in a reduction of the number of DoFs by a factor of six. Exploiting the knowledge of the irrelevant Fourier modes additionally allows us to eliminate most of the Lagrange multipliers before the assembly of the coupling matrice, leading to more efficient computations, especially when using the Schur complement formulation to compute the solution for an interface problem as explained in Section 3.3.1.2.

6.5.1.2 Discrete Torque

The torque is computed using (4.35) with FEM, i.e., $p = 1$ and with IGA, i.e., $p = 2$ for different harmonic orders of the Lagrange multiplier basis functions. Due to the $10°$ symmetry of the stator in the absence of excitation currents, which is also reflected in the mesh, the cogging torque of the machine also exhibits a $10°$-periodic behavior. The results can be seen in Fig. 6.15. It can be observed that the torque converges towards the reference solution for an increasing harmonic order N of the Lagrange multiplier basis functions, where the number of relevant Fourier modes is denoted by N_{eff}. Note that as discussed in Sections 4.1.2 and 6.4.1, the dimension of the Lagrange multiplier space must not exceed the number of DoFs of the solution associated to the interface such that the computation does not become unstable.

Using similar considerations for the periodicity of the stator geometry as before, the cogging torque can also be approximated by a Fourier series

$$T_{h,N}^{M}(\alpha) = \frac{\hat{c}_0}{2} + \sum_{m=1}^{M} \hat{c}_m \cos(m\alpha) + \hat{d}_m \sin(m\alpha) \tag{6.11}$$

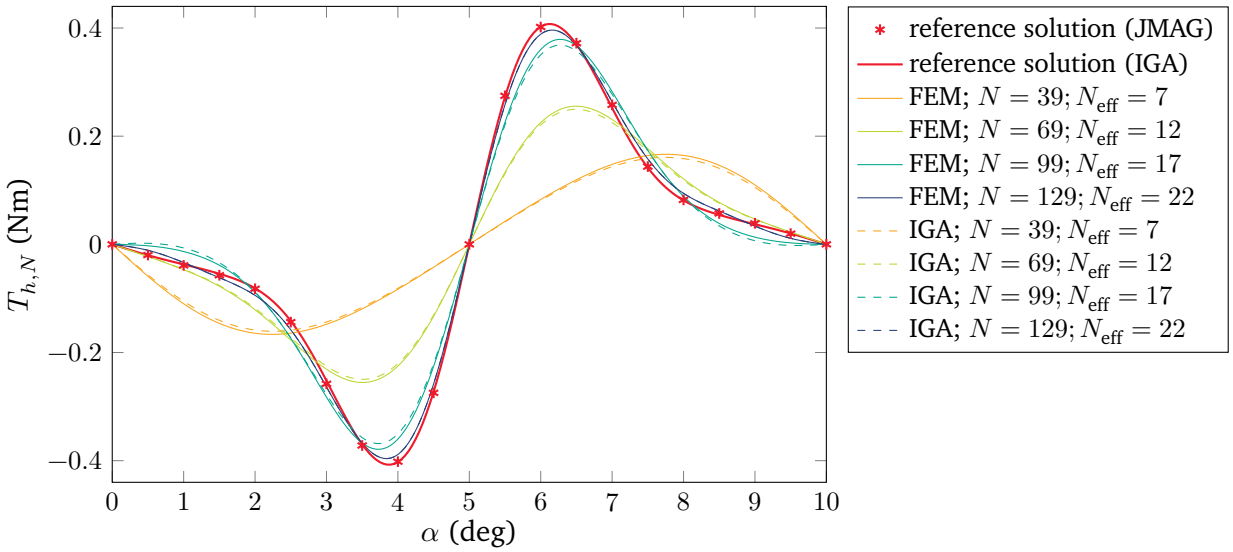

Figure 6.15: Cogging torque of the machine. Computed using trigonometric polynomials of degree N as basis for the Lagrange multiplier space. Computed with FEM and IGA using basis functions of degree $p = 1, 2$. Taken from [63].

Table 6.6: Relevant and irrelevant Fourier modes of the torque of an IGA simulation result for a full rotation of the machine. Taken from [63].

$\lvert\hat{d}_{36}\rvert$	$\lvert\hat{d}_{72}\rvert$	$\lvert\hat{d}_{108}\rvert$	$\sum_{m} \lvert\hat{c}_m\rvert$	$\sum_{m \notin \mathcal{M}} \lvert\hat{d}_m\rvert$
$2.293 \cdot 10^{-1}$	$1.784 \cdot 10^{-1}$	$9.17 \cdot 10^{-2}$	$6.2079 \cdot 10^{-11}$	$51.7843 \cdot 10^{-11}$

with coefficients $\hat{c}_m, \hat{d}_m \in \mathbb{R}$. By the symmetry properties discussed above, one can see that only the coefficients $\hat{d}_m$ with $m \in \mathcal{M} = \{36, 72, 108, ...\}$ are non-zero, while $\hat{d}_m = 0$ for all $m \notin \mathcal{M}$ and $\hat{c}_m = 0$ for all m. The corresponding results of our computations are shown in Table 6.6 confirming these considerations.

6.5.2 Torque of the 3D Machine

We use isogeometric mortaring with tree-cotree gauging described in Sections 4.1.1 and 4.2.1 to compute the magnetic field in the 3D model of the PMSM described in Section 6.1. We use degree $p = 2$ for the discrete spaces $V_{h,1}$ and $V_{h,2}$ and degree $q = 1$ for the Lagrange multiplier space M_h which we define on the interface mesh of Ω_1. For the computation we consider one pole pair with periodic BC. The stator domain consists of 228 patches and the rotor domain consists of 24 patches. The discretization of the stator leads to 270336 elements, resulting in 1058880 cotree DoFs and 601392 eliminated tree DoFs whereas the discretization of the rotor leads to 147456 elements, resulting in 540353 cotree DoFs and 309663 eliminated tree DoFs. The Lagrange multiplier space adds another 3912 DoFs.

We use the Arkkio's method (4.23) and the Lagrange multipliers (4.24) on both stator Ω_1 and rotor Ω_2 to compute the cogging torque in the machine for one period of the torque. We choose the whole part of the air gap $\Omega_{\text{air},1}$ and $\Omega_{\text{air},2}$, contained in Ω_1 and Ω_2, respectively, as integration volume in Arkkio's method. The results for the torque are shown in Fig. 6.16. They are compared to a 2D reference solution

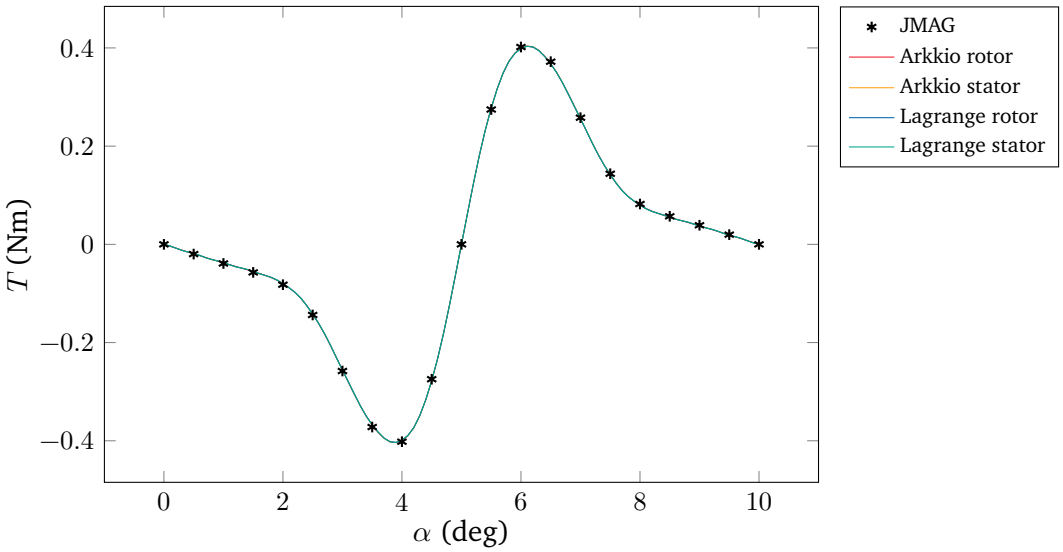

Figure 6.16: Torque computations via reference 2D FE solution (JMAG), Arkkio's method (4.23) on rotor and stator side (Arkkio rotor/stator), Lagrange multipliers method (4.24) on rotor and stator side (Lagrange rotor/stator). Taken from [116] ©2022 IEEE.

computed using JMAG® with a finite element discretization of order $p = 1$ with 1618173 elements. The torque curves for the different methods are in excellent agreement and all lie on top of each other. The deviation of the torque computed with the IGA approaches from the JMAG reference solution is visualized in Fig. 6.17. Furthermore, using these approaches, we do not observe the inaccuracies that are often reported for the evaluation of the line/surface integrals in torque computation. In our approach using IGA, the cylindrical geometry of the machine is exactly represented and the angular component of the magnetic field can be directly obtained from the Lagrange multipliers, alleviating the need to compute it numerically by differentiation of the magnetic vector potential. It is worth mentioning that in our computations, the approach using the Lagrange multipliers for the torque computation via (4.24) is two orders of magnitude faster than using Arkkio's method (4.23) as it only requires the evaluation of a surface integral as opposed to a volume integral in Arkkio's method. Thus, isogeometric mortaring is very well suited for the computation of the torque. Other quantities of interest can be evaluated similarly. However, the Lagrange multiplier approach is especially convenient when evaluating quantities which require the evaluation of the angular component of the magnetic field.

6.6 Shape Optimization

The shape optimization method described in Chapter 5 is used to minimize the THD of the EMF in the two-dimensional electric machine model described in Section 6.1. We optimize the rotor shape of the six-pole PMSM in generator mode under no load condition without additional constraints. We fix the shape and position of the permanent magnets in the machine.

The magnetic vector potential in the machine is discretized by $N_{\text{dof}} = 4354$ DoFs using B-splines of degree $p = 2$. The refinement level for the basis functions of the solution is chosen such that the relative error of the magnetic vector potential A is smaller than $1 \cdot 10^{-3}$. The coupling of stator and rotor domain is realized using the harmonic mortar method described in Section 4.3.3 with harmonic basis functions up

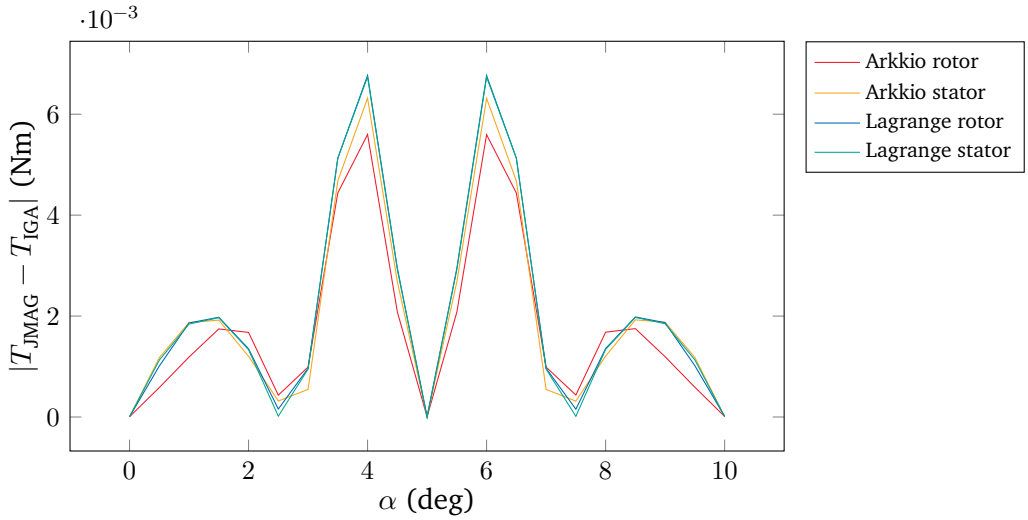

Figure 6.17: Absolute difference between the torque computed via reference 2D FE solution (JMAG) and the torque computed with IGA using Arkkio's method (4.23) on rotor and stator side (Arkkio rotor/stator), Lagrange multipliers method (4.24) on rotor and stator side (Lagrange rotor/stator). Taken from [116] ©2022 IEEE.

to trigonometric degree $N = 36$. As for the computation of the THD of the EMF we need to consider a rotating machine, we simulate a rotation of the machine of $120°$ which corresponds to one period of the electric phase. We discretize the rotation by considering $N_\alpha = 120$ points in time. Even though the original machine geometry can be exactly represented by NURBS with very few control points, we refine the geometry, allowing for a larger space of admissible geometries during the shape optimization. We choose the refinement level according to the refinement level of the discrete spaces of the solution, which facilitates moving the control points while optimizing.

The shape optimization of the rotor yields the optimized geometry shown in Fig. 6.18, where Fig. 6.18a shows the original rotor geometry whereas Fig. 6.18b shows the optimized rotor geometry. Due to the changes of the geometry not being easily visible, the changes are exaggerated by a factor 5 and shown in Fig. 6.18b as a black line. CAD representations of both original and optimized geometry are available as IGES files at [113]. The change of the geometry due to the shape optimization leads to a reduction of the THD of more than $75\,\%$. This reduction was achieved in 59 iterations. The THD during the iterations of the shape optimization algorithm outlined in Fig. 5.2 is visualized in Fig. 6.21. The EMF and its Fourier coefficients of the optimized machine are compared to the EMF and its Fourier coefficients of the original machine in Fig. 6.19. The machine is also optimized under full load condition incorporating the physical constraint

$$c(\Omega^S) = \tau(\Omega^S) - \tau_{\text{orig}} = 0, \tag{6.12}$$

where $\tau(\Omega^S)$ is the average torque for one rotation of the machine with the shape Ω^S and τ_{orig} is the average torque of the original machine design. The constraint (6.12) requires that the original torque is maintained. We incorporate this constraint using the augmented Lagrangian method [122], where we can derive the shape derivative of the torque analogously to Chapter 5. In this constrained optimization we achieve a reduction of the THD of the EMF by $44\,\%$ while maintaining the torque. The resulting geometry of the rotor is shown in Fig. 6.20 and the CAD description this optimized geometry is also available as an IGES file at [113].

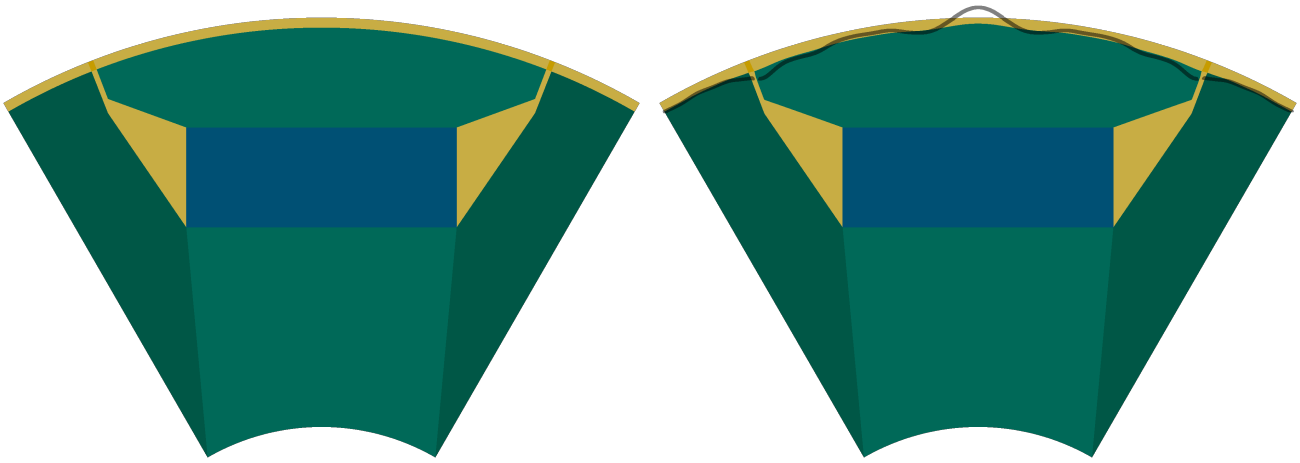

(a) Original design of the machine.

(b) Optimized design of the machine.

Figure 6.18: Results of shape optimization (5.2) in generator mode under no load condition. The shape of the rotor was optimized, minimizing the total harmonic distortion. Shape and position of the permanent magnet was fixed. Figure (a) shows the original design, figure (b) shows the optimized design. The black line shows the changes in the rotor amplified by a factor of 5. Taken from [114] ©2021 IEEE.

Table 6.7: Total harmonic distortion of the electromotive force $\mathcal{E}$ for original and the optimized rotor design computed with IGA and with JMAG® for linear and non-linear material laws. Taken from [114]. ©2021 IEEE

	THD($\mathcal{E}$) original design	THD($\mathcal{E}$) optimized design
IGA linear	0.099268	0.024793
JMAG linear	0.099754	0.02234
JMAG non-linear	0.10639	0.034106

6.6.1 Verification using JMAG

For the shape optimization algorithm, we employ the IGA solution with linear material laws, using the material parameters outlined in Section 6.1. Thanks to the representation of the geometry in NURBS, we can easily import the original and also the optimized geometries into computer aided engineering (CAE) software, e.g., using the IGES format. This allows an easy integration of this technology in existing workflows.

The results for the original and optimized geometries are verified using JMAG. The JMAG® model is discretized by 281198 elements of order 1. Here, we consider both linear material relations and, to investigate the impact of saturation on the result, also non-linear material relations. The results using linear material laws are in very good agreement with the results obtained from the IGA implementation. They are shown in Figs. 6.19 and 6.21 for the original and optimized machine. The main machine characteristics of the original and the optimized motor designs are given in Table 6.8. The cogging torque and the radial

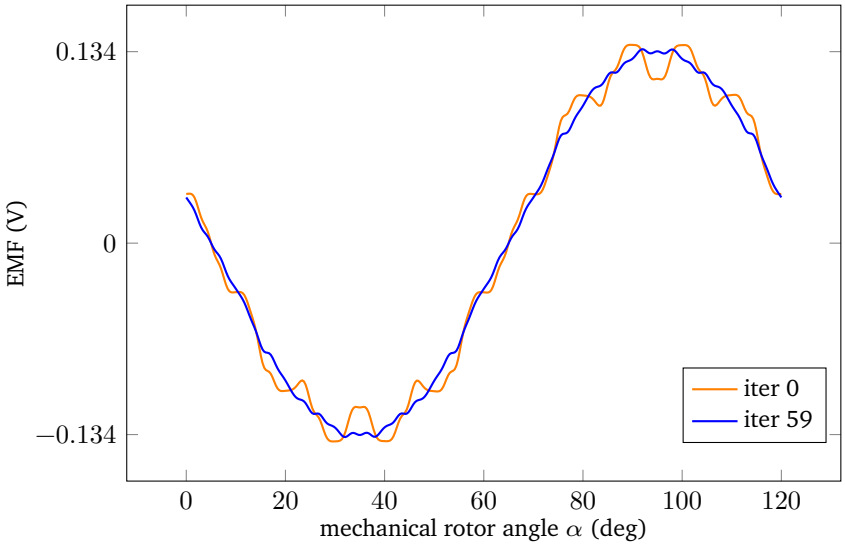

(a) Electromotive force for a rotation of the rotor.

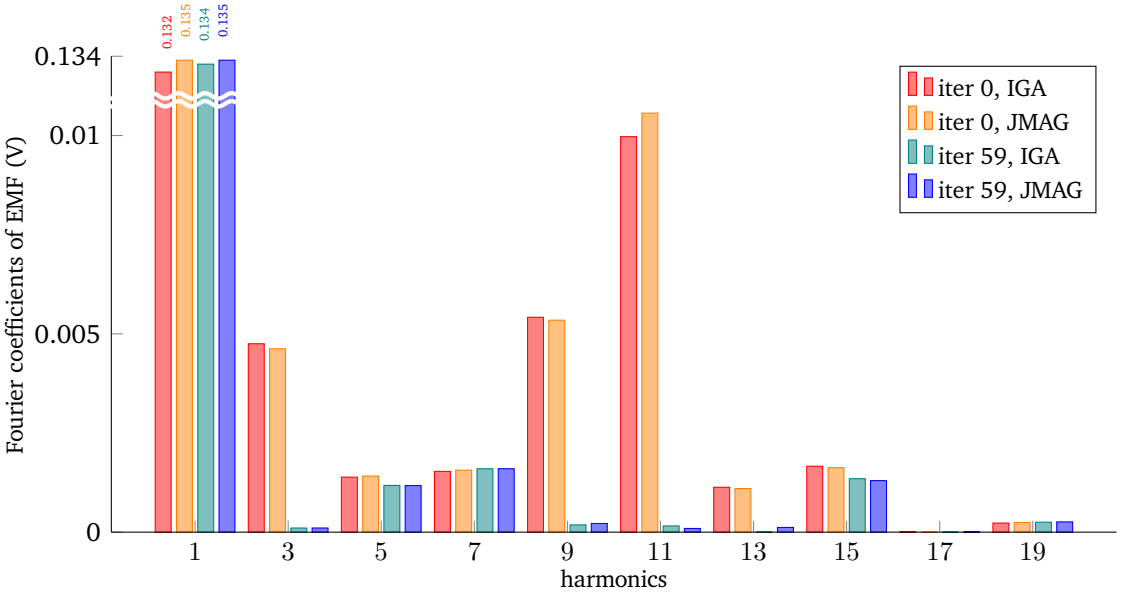

(b) Fourier coefficients of the electromotive force.

Figure 6.19: Electromotive force for the original design and for the optimized design after 59 iterations. Computed using linear material laws. Taken from [114] ©2021 IEEE.

Figure 6.20: Results of shape optimization (5.2)–(5.3) under full load condition. The shape of the rotor was optimized, minimizing the total harmonic distortion with the physical constraint (6.12) maintaining the average torque. Shape and position of the permanent magnet was fixed. Taken from [114]. ©2021 IEEE

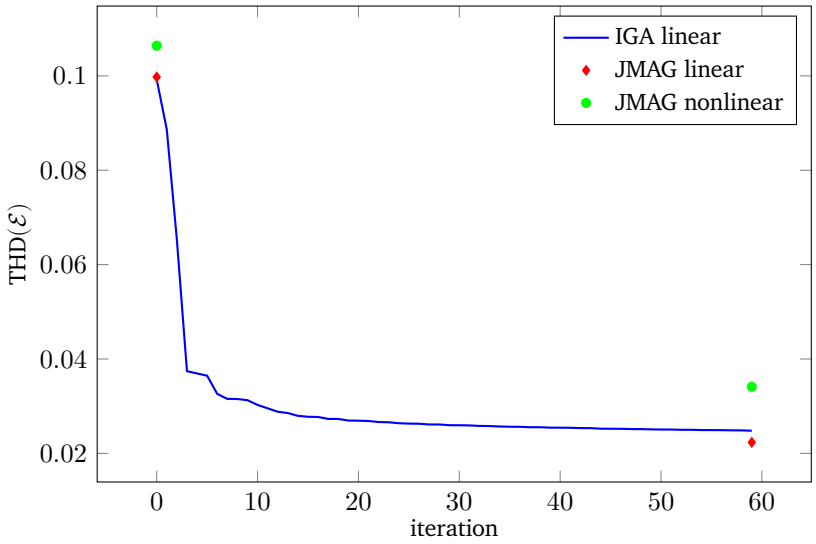

Figure 6.21: Total harmonic distortion of the electromotive force $\mathcal{E}$ for each iteration of the shape optimization (5.2) in generator mode under no load condition computed with IGA and with JMAG® as a reference. Taken from [114] ©2021 IEEE.

Table 6.8: Main characteristics of the original and the optimized rotor design computed with JMAG®. Taken from [114] ©2021 IEEE.

	original design	optimized design
Rated speed	1930 rpm	1930 rpm
Rated current I_{eff}	10.6 A	10.6 A
Torque τ	11.62 Nm	11.34 Nm
Power P	2349.0 W	2292.1 W
Open circuit voltage $\mathcal{E}$	57.76 V	57.72 V
Flux linkage Ψ	0.0953 Wb	0.0952 Wb

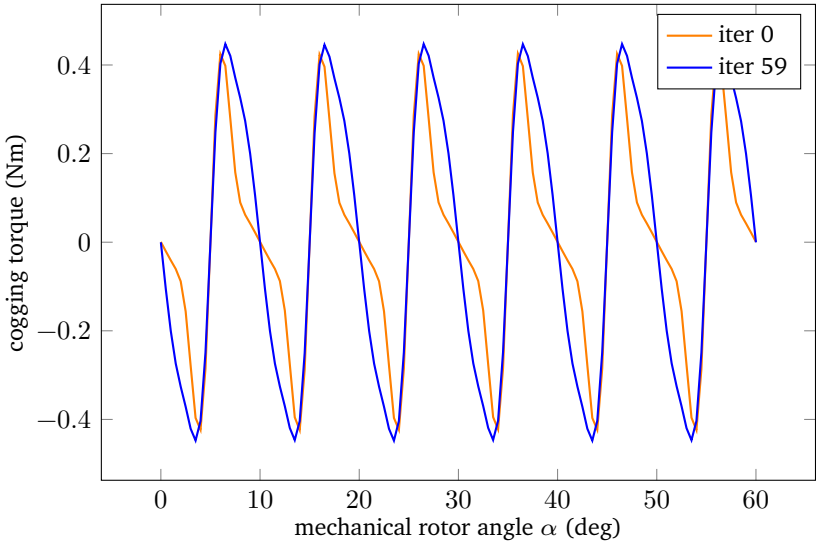

Figure 6.22: Cogging torque of the motor for the original design and for the optimized design after 59 iterations. Computed using linear material laws. Taken from [116] ©2022 IEEE.

component of the magnetic flux density in the air gap of original and optimized machine are compared in Figs. 6.22 and 6.23. Without the constraint that the torque is maintained, the optimization of the machine leads to a slight weakening of the torque. When operating the machine at full load, i.e., using an excitation current with effective value $I_{\text{eff}} = 10.6\,\text{A}$, the torque of the original machine design is $\tau_{\text{iter0}} = 11.62\,\text{Nm}$. The torque of the optimized design is $\tau_{\text{iter59}} = 11.34\,\text{Nm}$.

For considering non-linear material laws, we model iron in JMAG® by the material curve M530-50A. The results for the non-linear material laws can also be seen in Fig. 6.21 and Table 6.7, where still a reduction of $68\,\%$ in the THD is achieved. The comparison of the Fourier coefficients of the EMF in the case of non-linear material laws is shown in Fig. 6.24. Considering non-linear material laws for a partial load of $30\,\%$, the torque is slightly reduced from $\tau_{\text{iter0}} = 1.95\,\text{Nm}$ for the original design to $\tau_{\text{iter59}} = 1.90\,\text{Nm}$ for the optimized design. The THD of the EMF is reduced from $\text{THD}_{\text{iter0}} = 0.132$ for the original design to $\text{THD}_{\text{iter59}} = 0.098$ for the optimized design. This corresponds to a reduction by $26\,\%$. The consideration of non-linear material laws during the optimization process might lead to a lower THD. However, it would also lead to a significant increase of computational cost. Thus, we conclude that even though the consideration of fully non-linear material relations increases the THD, the optimization using the linear model is still effective.

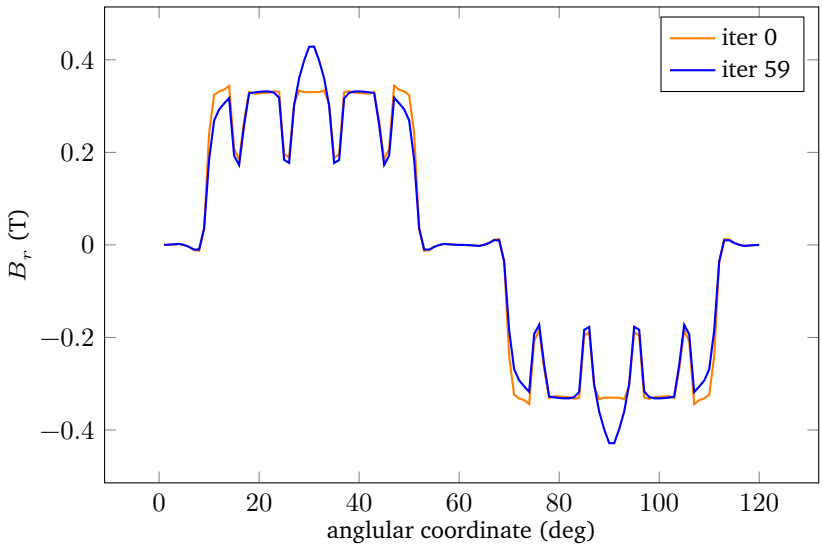

Figure 6.23: Radial component B_r of the magnetic flux density in the air gap of the motor for the original design and for the optimized design after 59 iterations. Taken from [116] ©2022 IEEE.

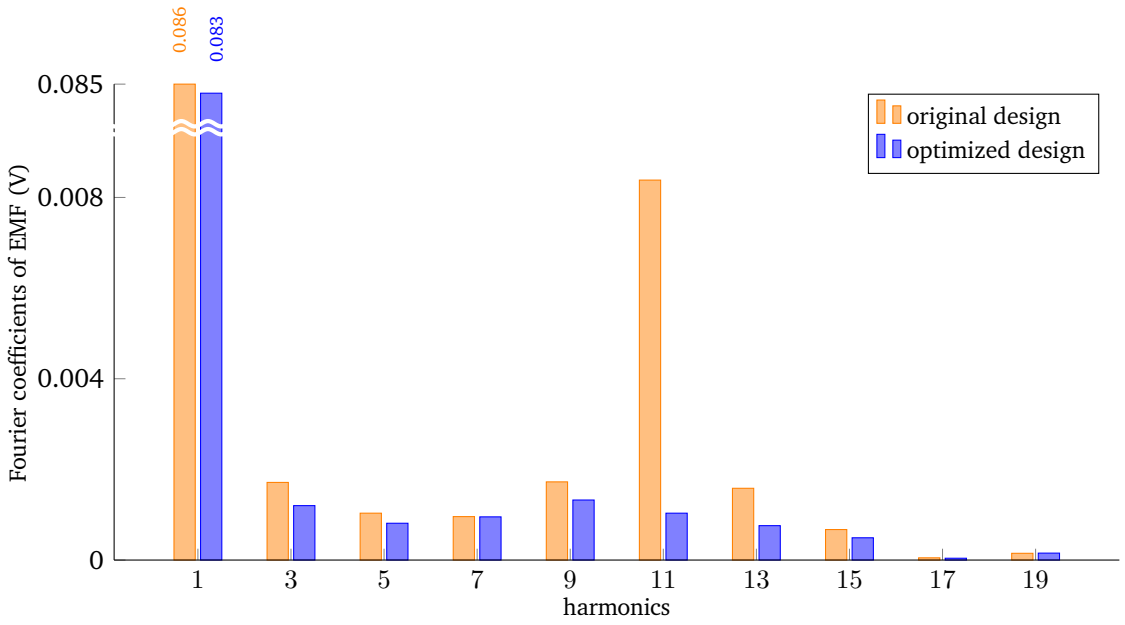

Figure 6.24: Fourier coefficients of the electromotive force for the original design and for the optimized design after 59 iterations considering non-linear material laws in stator and rotor core (i.e. electrical steel M530-50A), calculated using JMAG®. Taken from [114] ©2021 IEEE.

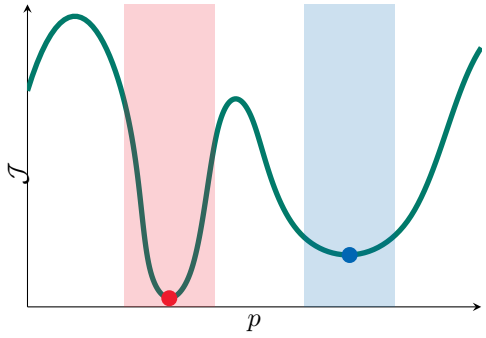

Figure 6.25: Schematic visualization of two local optima of the objective function $\mathcal{J}$ depending on the uncertain parameter p, the red optimum is not robust, the blue optimum is robust.

A three-dimensional simulation can be carried out to validate that the optimized machine model does in fact improve the quantity of interest. One could also carry out the optimization on a three-dimensional machine model to also take into account end winding effects that cannot be captured by the two-dimensional approximation. However, this would result in significantly larger systems and, therefore, would considerably increase the computational time as the machine model has to be evaluated many times during the optimization. Considering the prototyping character of the code, this would result in a prohibitively computationally expensive method and is therefore not investigated. Similarly, we did not consider non-linear material laws during the optimization process and only used a model with non-linear material laws during the validation of the optimization results. Non-linear material laws might be included during the optimization process, e.g., using a fix-point iteration. Methods to deal with high computational cost and long computation times for the solution of the machine model during optimization include, for example, the use of low-dimensional surrogate models, see, e.g., [87]. The optimization algorithm could also be extended to allow for a robust optimization. This means that the optimized solution should not be too sensitive to uncertain parameters of the machine, e.g., manufacturing uncertainties. When the optimized design is too sensitive, the objective function might suffer from a large increase when the machine geometry or material parameters slightly differ from the nominal design. In this case, the found minimum of the objective function is not robust. A schematic visualization of a robust minimum can be seen in Fig. 6.25. To obtain a robust optimum, the optimization could be carried out considering the uncertainty of the parameters, which would again increase the computational effort as deviations from the nominal design would also have to be considered and additionally, the periodicity of the machine could not be assumed anymore. For robust machine optimization methods, see, e.g., [22, 25, 87, 102].

6.7 Summary

In this chapter, we have applied the methods proposed in the previous chapters to a model problem with a known analytical solution and to an electric machine model in both two and three dimensions.

The application of the modified B-spline multiplier space for mortaring of multi-patch domains introduced in Section 4.1.1 resulted in spurious free solutions. Additionally, the adapted tree-cotree decomposition for mortared domains explained in Section 4.2.1 has also been shown to correctly remove the discrete kernel of the mortar problem.

For the three-dimensional coupling of stator and rotor, we have further investigated the Nitsche coupling method for isogeometric analysis. Here, we examined the sensitivity with respect to the Nitsche penalty factor, where we found the method to be feasible for a large range of penalty factors. The method was shown to converge with the degree of the basis functions, where the loss of one order of convergence reported in [37] could not be observed.

The stability of the harmonic mortar formulation was analyzed by means of the inf-sup constant. The stability condition proposed in Section 4.1.2 was confirmed by numerically evaluating the inf-sup constant in an annulus domain, where the analytical solution could be computed. The behavior of the inf-sup constant has also been examined for the two-dimensional machine model, where the stability condition for choosing an appropriate discrete Lagrange multiplier space (4.18) could also be verified.

Different methods for torque computation have been applied to the two- and three-dimensional machine models, including the Arkkio method and the methods proposed in Section 4.3 that exploit the Lagrange multiplier for the torque computation in two and three dimensions. The methods have been found to yield the correct torque, and the methods taking advantage of the Lagrange multipliers were found to require a computational time that is two orders of magnitude smaller.

Finally, the shape optimization method outlined in Chapter 5 was applied to optimize the two-dimensional model of a permanent magnet synchronous machine (PMSM), where a reduction of the total harmonic distortion of up to $75\,\%$ could be achieved. This considerable improvement of the objective function shows the effectiveness of isogeometric shape optimization which allows for straightforward modification of the geometry by simply moving the control points.

7 Conclusion and Prospects for Future Research

In this work, different methods for the simulation of electric machines based on isogeometric analysis (IGA) have been investigated. Several approaches incorporate rotation were discussed, and their integration with IGA was investigated. A method for the shape optimization of electric machines using shape calculus has been derived and employed for the minimization of the total harmonic distortion (THD) of the electromotive force (EMF) of an electric machine. The proposed methods have been applied to a permanent magnet synchronous machines (PMSMs) model. These methods, though discussed within the context of electric machines, are not limited to this domain. They could be employed for electromagnetic field computation in a variety of rotating applications, e.g., electrocaloric cooling devices [162].

The use of IGA in electric machine computations provides an exact representation of the machines' cylindrical structure. However, classical IGA requires a conforming patch-discretization of the geometry, making the implementation of rotation a complex task. To solve this problem, different methods for the coupling of non-conforming discretizations have been introduced in Chapter 3, including classical mortaring, harmonic coupling and Nitsche-type coupling. We also proposed a Schur complement-based reduction of the harmonic mortar system to a low-dimensional interface problem, which can significantly reduce computational costs when simulating rotating machines. In Chapter 4, we provided a condition for the selection of the Lagrange multiplier space to ensure the stability of the harmonic coupling system. Furthermore, we proposed a new, modified Lagrange multiplier space for the isogeometric mortar method, which guarantees the correctness of the solution and eliminates spurious modes when gauging. In Section 4.3, we introduced several methods for torque computation in an electric machine, including efficient strategies exploiting the Lagrange multipliers obtained from the isogeometric mortaring and the harmonic coupling method. In the two-dimensional case using the multipliers from the harmonic mortar is more efficient than employing the Arkkio method or the torque computation via the Maxwell stress tensor as no additional integration is necessary. In the three-dimensional case the Lagrange multiplier method also outperforms Arkkio's method as numerical integration is only required on surfaces rather than on volumes which are computationally more expensive.

One challenge in three-dimensional magnetostatic problem simulation using a magnetic vector potential approach is the non-uniqueness of the solution. In the finite element method (FEM), a tree-cotree decomposition can be used to remove the discrete kernel from the system matrix. An application of tree-cotree gauging to IGA has been proposed. As we compute electric machines using non-conforming methods, the application of a tree-cotree decomposition is not clear. In Chapter 4, a modified tree-cotree decomposition for mortared geometries has been developed. The construction of a conforming patch discretization surrounding the winding heads poses a challenge for the simulation of three-dimensional electric machines, which include the full windings. To address this, we proposed a two-step approach that does not require a full conforming patch discretization of the surrounding air. The first step involves calculating the current in the winding by solving a stationary current problem. The computed current is then used in the

second step as a right-hand side function in the air-region surrounding the machine without actual winding discretization in the geometry. This may introduce minor inaccuracies, which can be mitigated by refinement and increasing the accuracy of the quadrature, such that the obtained solution is sufficiently accurate.

In Chapter 5, shape calculus has been used to derive the shape derivative of the THD of the EMF in a machine. Using this shape derivative, a gradient-based shape optimization approach was developed for the minimization of the given objective function. In this method, the shape derivative is used to compute a descent direction, i.e., the negative shape gradient, such that the geometry of the machine can be modified according to the descent direction, yielding a decrease of the objective function. IGA is particularly suitable for this geometry modification, as the alteration can be easily achieved by moving the control points in the direction of the obtained negative shape gradient. The proposed shape optimization method has been employed to minimize the THD of the EMF of PMSM, where a reduction of $75\,\%$ was achieved. The introduction of constraints using an augmented Lagrangian method allowed for a THD reduction of $44\,\%$ under a fixed average torque. The results of the shape optimization and their effectiveness has been verified using commercial software.

We conclude that the proposed methods and theory pave the way for a new spline-based multiphysical design workflow for electric machines, including their optimization using IGA. They allow for an efficient and accurate simulation and optimization, saving time, cost and resources. The proposed approaches have already been applied for the computation of heat distribution in the windings of the machine in Fig. 4.5 due to the currents in [161].

In future works, the Nitsche-coupling method could be further examined in terms of the discrete kernel of the system to permit the application of tree-cotree gauging. The isogeometric mortar method could be applied between all patches, possibly employing an isogeometric tearing and interconnecting approach. This allows for local refinement and opens the possibility for parallelization. As an extension to shape optimization, the machine's topology might also be optimized, allowing the discovery of new machine designs with a novel material distribution. The use of IGA enables a direct application of the geometry in computer aided design (CAD), potentially for 3D printing of machine parts. This opens up possibilities for the manufacturability of new machine designs, e.g., in the topology of the windings. The shape optimization method can also be extended to allow for multi-objective optimization and for robust optimization, where uncertainties in certain parameters, such as manufacturing uncertainties or uncertain operating conditions, are taken into account. This way, robust machine designs can be found, which are not sensitive to the considered uncertain parameters. The incorporation of eddy current effects, non-linearities and hysteresis is expected to be simple in the sense that this does not differ from conventional finite elements. The simulation could be extended to allow for a multiphysical simulation, incorporating thermal and mechanical effects or even fluid dynamics, enabling Noise, Vibration, Harshness (NVH) studies. This allows the simulations in the multiphysical workflow in the design process, illustrated in Fig. 1.1, to be employed on the same CAD geometry for all design stages.

8 Appendix

8.1 Fourier Transformation of B-Splines

The coupling matrices (3.89) are computed using numerical quadrature. In special cases however, they can be computed using a closed-form formula, making the assembly of the coupling matrices very efficient. For the computation of the coupling matrices in the case of harmonic mortaring, we can apply the Fourier transformation of B-splines

$$\lambda_c(j,k,\Xi;y) = \int_{-\infty}^{\infty} B_j^k(x) e^{\imath y x} \,\mathrm{d}\, x \tag{8.1}$$

with knot vector Ξ. The obtained λ_c can then be used to easily obtain the entries of the coupling matrix, using the relation (2.50). In [120] Edward Neuman derives a closed form solution for the Fourier transformation of Curry-Schoenberg B-splines $M_j^k(x)$ with knots $\xi_j < \xi_{j+1} < \cdots < \xi_{j+k}$ which are defined by

$$M_j^k(x) = k[\xi_j, \xi_{j+1}, \dots, \xi_{j+k}] \cdot (-x)_+^{k+1}, \tag{8.2}$$

where $x_+^{k-1} = (\max\{0,x\})^{k-1}$ and $[\xi_j, \xi_{j+1}, \dots, \xi_{j+k}]f$ is the k-th divided difference for the function f in the points $\{\xi_j\}^{j+k}$ [8]. Neuman's closed form formula for Fourier transformations of Curry-Schoenberg B-splines for equidistant knots $\xi_j = a + jh$ is given by

$$\int_{-\infty}^{\infty} M_j^k(x) e^{\imath y x} \,\mathrm{d}\, x = e^{\imath y a} \left(\frac{e^{\imath h y} - 1}{\imath h y} \right)^k. \tag{8.3}$$

The B-splines we use can be expressed in terms of Curry-Schoenberg B-splines as

$$\begin{aligned} B_j^k(x) &= \left([\xi_{j+1}, \dots, \xi_{j+k}] - [\xi_j, \dots, \xi_{j+k+1}] \right) \cdot (-x)_+^{k-1} && (8.4) \\ &= \left(\xi_{j+k} - \xi_j \right) M_j^k(x)/k, && (8.5) \end{aligned}$$

(see [47]) which in the case of equidistant knots reduces to

$$B_j^k(x) = (a + (j+k)h - (a+jh))\, M_j^k(x)/k = h M_j^k(x). \tag{8.6}$$

Therefore, the Fourier transformation (8.1) is given in closed form by

$$\lambda(j,k,\Xi,y) = h e^{\imath y(\xi_j + 0.5h)} \left(\frac{e^{\imath h y} - 1}{\imath h y} \right)^k. \tag{8.7}$$

However in the classical multi-patch approach we only have C^0 continuity at path interfaces, i.e., open knot vectors are used. In the multi-patch machine model we use open knot vectors, i.e., the first and

last knot are repeated $k = p + 1$ times for a B-spline of order k (polynomial degree p). Thus the knot vector is not equidistant and (8.7) does not apply for the first and the last k basis functions at which are at the patch borders. For the computation of these Fourier transformations we have to use numerical quadrature. For all other, i.e., inner, basis functions we can use (8.7) for the computation of the Fourier transformations.

8.2 Parameters of the Used Permanent Magnet Synchronous Machine

The geometry and material parameters for the used model of the PMSM shown in Fig. 6.2 are listed Table 8.1 and Table 8.2, respectively. The parameters have been taken from [22, Chapter V.A]. The original design of the machine was proposed in [123, page 125]. The machine is three-phase winding six-pole PMSM. For more detailed parameters, see [22, Chapter V.A]. The CAD description of the machine is freely available in IGES format in [113].

Table 8.1: Geometry parameters used for the PMSM model. Parameters are taken from [22, Chapter V.A].

Stator		
Inner radius	$R_{1,\mathrm{i}}$	45 mm
Outer radius	$R_{1,\mathrm{o}}$	67.5 mm
Machine length	L_z	100 mm
Number of winding turns	N_{w}	12
Rotor		
Inner radius	$R_{2,\mathrm{i}}$	16 mm
Outer radius	$R_{2,\mathrm{o}}$	44 mm
Magnet width	d_{w}	19 mm
Magnet height	d_{h}	7 mm
Machine length	L_z	100 mm
Rotation angle	α	
Air gap		
Radius	R_Γ	44.7 mm

Table 8.2: Material properties used for the PMSM model. Parameters are taken from [22, Chapter V.A].

Material properties		
Relative permeability of iron	$\mu_{\mathrm{r},Fe}$	500
Relative permeability of permanent magnets	$\mu_{\mathrm{r},PM}$	1.05
Relative permeability of copper	$\mu_{\mathrm{r},Cu}$	1
Conductivity of iron	σ_{Fe}	$0\,\mathrm{S\,m^{-1}}$
Conductivity of permanent magnets	σ_{PM}	$0\,\mathrm{S\,m^{-1}}$
Conductivity of copper	σ_{Cu}	$0\,\mathrm{S\,m^{-1}}$
Remanent magnetic field of permanent magnets	$\mathbf{B}_{\mathrm{PM}}$	0.94 T

List of Acronyms

2D	two-dimensional
AC	alternating current
BC	boundary condition
BFS	breadth-first search
CAD	computer aided design
CAE	computer aided engineering
DC	direct current
DoF	degree of freedom
EMF	electromotive force
FE	finite element
FEM	finite element method
IGA	isogeometric analysis
IPMSM	interior permanent magnet synchronous machine
KPI	key performance indicator
LBB	Ladyzhenskaya–Babuška–Brezzi
NURBS	non-uniform rational B-splines
PDE	partial differential equation
PEC	perfect electric conductor
PMC	perfect magnetic conductor
PMSM	permanent magnet synchronous machine
THD	total harmonic distortion

Bibliography

[1] R. Albanese and G. Rubinacci, *Integral formulation for 3d eddy-current computation using edge elements*, *IEE Proceedings - Science, Measurement and Technology*, vol. 135, no. 7, pp. 457–462, 1988. DOI: 10.1049/ip-a-1:19880072.

[2] A. T. de Almeida, J. Fong, H. Falkner, and P. Bertoldi, *Policy options to promote energy efficient electric motors and drives in the EU*, *Renewable and Sustainable Energy Reviews*, vol. 74, pp. 1275–1286, 2017, ISSN: 1364-0321. DOI: 10.1016/j.rser.2017.01.112.

[3] A. Alonso Rodríguez and A. Valli, *Eddy Current Approximation of Maxwell Equations* (Modeling, Simulation and Applications). Heidelberg: Springer, 2010, vol. 4. DOI: 10.1007/978-88-470-1506-7.

[4] P. Alotto, A. Bertoni, I. Perugia, and D. Schötzau, *Discontinuous finite element methods for the simulation of rotating electrical machines*, *COMPEL: The International Journal for Computation and Mathematics in Electrical and Electronic Engineering*, vol. 20, no. 2, pp. 448–462, 2001, ISSN: 0332-1649. DOI: 10.1108/03321640110383320.

[5] A. Apostolatos, R. Schmidt, R. Wüchner, and K.-U. Bletzinger, *A Nitsche-type formulation and comparison of the most common domain decomposition methods in isogeometric analysis*, *International Journal for Numerical Methods in Engineering*, vol. 97, no. 7, pp. 473–504, 2013, ISSN: 0029-5981. DOI: 10.1002/nme.4568.

[6] A. Arkkio, *Analysis of induction motors based on the numerical solution of the magnetic field and circuit equations*, PhD Thesis, Helsinki University of Technology, 1987, ISBN: 951-22-6076-X. urn: urn:nbn:fi:tkk-001267.

[7] D. N. Arnold, *Finite Element Exterior Calculus*. SIAM, 2018, ISBN: 978-1-61197-553-6. DOI: 10.1137/1.9781611975543.

[8] H. B. Curry and I. J. Schoenberg, *On polya frequency functions iv: The fundamental spline functions and their limits*, vol. 17, pp. 71–107, 1966.

[9] I. Babuška, *The finite element method with Lagrangian multipliers*, *Numer. Math.*, vol. 20, pp. 179–192, 1973.

[10] D. Balian, M. Merkel, J. Ostrowski, H. De Gersem, and S. Schöps, *Low-frequency stabilization of dielectric simulation problems with conductors and insulators*, *IEEE Transactions on Dielectrics and Electrical Insulation*, 2023, ISSN: 1070-9878. DOI: 10.1109/TDEI.2023.3277414. arXiv: 2302.00313, inprint.

[11] M. L. Bash and S. D. Pekarek, *Modeling of salient-pole wound-rotor synchronous machines for population-based design*, *IEEE Transactions on Energy Conversion*, vol. 26, no. 2, pp. 381–392, 2011, ISSN: 0885-8969.

[12] U. Baumgartner, C. Magele, and W. Renhart, *Pareto optimality and particle swarm optimization*, *IEEE Transactions on Magnetics*, vol. 40, no. 2, p. 1172, 2004, ISSN: 0018-9464.

[13] Y. Bazilevs and T. J. R. Hughes, *Weak imposition of Dirichlet boundary conditions in fluid mechanics*, *Computers & Fluids*, vol. 36, no. 1, pp. 12–26, 2007, ISSN: 0045-7930. DOI: 10.1016/j.compfluid.2005.07.012.

[14] L. Beirão da Veiga, A. Buffa, G. Sangalli, and R. Vázquez, *Mathematical analysis of variational isogeometric methods*, *Acta Numerica*, vol. 23, pp. 157–287, 2014, ISSN: 1474-0508. DOI: 10.1017/s096249291400004x.

[15] C. Bernardi, Y. Maday, and A. T. Patera, *Domain decomposition by the mortar element method*, in *Asymptotic and Numerical Methods for Partial Differential Equations with Critical Parameters*, H. G. Kaper, M. Garbey, and G. W. Pieper, Eds. Dordrecht: Springer Netherlands, 1993, pp. 269–286, ISBN: 978-94-011-1810-1. DOI: 10.1007/978-94-011-1810-1_17.

[16] A. Binder, *Elektrische Maschinen und Antriebe*. Berlin Heidelberg: Springer, 2012, ISBN: 978-3-540-71850-5. DOI: 10.1007/978-3-540-71850-5.

[17] O. Bíró and K. Preis, *On the use of the magnetic vector potential in the finite-element analysis of three-dimensional eddy currents*, *IEEE Transactions on Magnetics*, vol. 25, no. 4, pp. 3145–3159, 1989, ISSN: 0018-9464. DOI: 10.1109/20.34388.

[18] O. Bíró and A. Valli, *The Coulomb gauged vector potential formulation for the eddy-current problem in general geometry: Well-posedness and numerical approximation*, *Computer Methods in Applied Mechanics and Engineering*, vol. 196, no. 13-16, pp. 1890–1904, 2007, ISSN: 0045-7825. DOI: 10.1016/j.cma.2006.10.008.

[19] D. Boffi, F. Brezzi, and M. Fortin, *Mixed Finite Element Methods and Applications*. Springer, Berlin-Heidelberg, 2013. DOI: 10.1007/978-3-642-36519-5.

[20] P. T. Boggs, A. Altshuler, A. R. Larzelere, E. J. Walsh, R. L. Clay, and M. F. Hardwick, *DART system analysis*, Sandia gi, Technical Report SAND2005-4647, 2005. DOI: 10.2172/876325.

[21] S. S. R. Bonthu, M. T. B. Tarek, and S. Choi, *Optimal torque ripple reduction technique for outer rotor permanent magnet synchronous reluctance motors*, *IEEE Transactions on Energy Conversion*, vol. 33, no. 3, pp. 1184–1192, 2018.

[22] Z. Bontinck, *Simulation and robust optimization for electric devices with uncertainties*, Dissertation, Technische Universität Darmstadt, Darmstadt, 2018. urn: urn:nbn:de:tuda-tuprints-83302.

[23] Z. Bontinck, J. Corno, H. De Gersem, S. Kurz, A. Pels, S. Schöps, F. Wolf, C. de Falco, J. Dölz, R. Vázquez, and U. Römer, *Recent advances of isogeometric analysis in computational electromagnetics*, *International Compumag Society Newsletter*, vol. 24, no. 3, pp. 5–16, 2017, ISSN: 1026-0854. arXiv: 1709.06004.

[24] Z. Bontinck, J. Corno, S. Schöps, and H. De Gersem, *Isogeometric analysis and harmonic stator-rotor coupling for simulating electric machines*, *Computer Methods in Applied Mechanics and Engineering*, vol. 334, pp. 40–55, 2018, ISSN: 0045-7825. DOI: 10.1016/j.cma.2018.01.047. arXiv: 1709.05301.

[25] Z. Bontinck, O. Lass, S. Schöps, H. De Gersem, S. Ulbrich, and O. Rain, *Robust optimization formulations for the design of an electric machine*, *IET Science, Measurement & Technology*, vol. 12, no. 8, pp. 939–948, 2018, ISSN: 1751-8822. DOI: 10.1049/iet-smt.2018.5235. arXiv: 1712.01536.

[26] A. Bossavit, *Computational Electromagnetism: Variational Formulations, Complementarity, Edge Elements*. San Diego, CA, USA: Academic Press, 1998, ISBN: 978-0-12-118710-1. DOI: 10.1016/B978-0-12-118710-1.X5000-4.

[27] F. Bouillault, A. Buffa, Y. Maday, and F. Rapetti, *The mortar edge element method in three dimensions: Applications to magnetostatics*, *SIAM Journal on Scientific Computing*, vol. 24, no. 4, pp. 1303–1327, 2001, ISSN: 1064-8275.

[28] D. Braess, *Finite Elemente*. Berlin: Springer, 2007, ISBN: 978-3540724490.

[29] D. Braess, W. Dahmen, and C. Wieners, *A multigrid algorithm for the mortar finite element method*, *SIAM J. Numer. Anal.*, vol. 37, pp. 48–69, 1999.

[30] F. Brezzi, *On the existence, uniqueness and approximation of saddle-point problems arising from Lagrangian multipliers*, *RAIRO Anal. Numer.*, vol. 8, pp. 129–151, 1974.

[31] E. Brivadis, A. Buffa, B. Wohlmuth, and L. Wunderlich, *Isogeometric mortar methods*, *Computer Methods in Applied Mechanics and Engineering*, vol. 284, pp. 292–319, 2015, ISSN: 0045-7825. DOI: 10.1016/j.cma.2014.09.012.

[32] A. Buffa, J. Corno, C. de Falco, S. Schöps, and R. Vázquez, *Isogeometric mortar coupling for electromagnetic problems*, *SIAM Journal on Scientific Computing*, vol. 42, no. 1, B80–B104, 2020, ISSN: 1064-8275. DOI: 10.1137/18M1235211. arXiv: 1901.00759.

[33] A. Buffa, J. Dölz, S. Kurz, S. Schöps, R. Vázquez, and F. Wolf, *Multipatch approximation of the de Rham sequence and its traces in isogeometric analysis*, *Numerische Mathematik*, vol. 144, no. 1, pp. 201–236, 2019, ISSN: 0029-599X. DOI: 10.1007/s00211-019-01079-x. arXiv: 1806.01062.

[34] A. Buffa, E. M. Garau, C. Giannelli, and G. Sangalli, *On quasi-interpolation operators in spline spaces*, in ser. Lect. Notes Comput. Sci. Eng. Vol. 114, Springer, 2016, pp. 73–91.

[35] A. Buffa, G. Sangalli, and R. Vázquez, *Isogeometric analysis in electromagnetics: B-splines approximation*, *Computer Methods in Applied Mechanics and Engineering*, vol. 199, pp. 1143–1152, 2010, ISSN: 0045-7825. DOI: 10.1016/j.cma.2009.12.002.

[36] A. Buffa, G. Sangalli, and R. Vázquez, *Isogeometric methods for computational electromagnetics: B-spline and t-spline discretizations*, *Journal of Computational Physics*, vol. 257, pp. 1291–1320, 2013, ISSN: 0021-9991. DOI: 10.1016/j.jcp.2013.08.015.

[37] R. Casagrande, C. Winkelmann, R. Hiptmair, and J. Ostrowski, *DG treatment of non-conforming interfaces in 3d curl-curl problems*, in *Scientific Computing in Electrical Engineering SCEE 2014*, A. Bartel, M. Clemens, M. Günther, and E. J. W. ter Maten, Eds., ser. Mathematics in Industry, Berlin: Springer, 2016, pp. 53–61, ISBN: 978-3-319-30399-4. DOI: 10.1007/978-3-319-30399-4_6.

[38] B. N. Cassimere and S. D. Sudhoff, *Population-based design of surface-mounted permanent-magnet synchronous machines*, *IEEE Transactions on Energy Conversion*, vol. 24, no. 2, pp. 338–346, 2009, ISSN: 0885-8969.

[39] D. Chapelle and K. Bathe, *The inf-sup test*, *Computers & Structures*, vol. 47, no. 4, pp. 537–545, 1993, ISSN: 0045-7949. DOI: https://doi.org/10.1016/0045-7949(93)90340-J.

[40] M. Clemens, *Large systems of equations in a discrete electromagnetism: Formulations and numerical algorithms*, *IEE Proceedings - Science, Measurement and Technology*, vol. 152, no. 2, pp. 50–72, 2005. DOI: 10.1049/ip-smt:20050849.

[41] M. Clemens and T. Weiland, *Regularization of eddy-current formulations using discrete grad-div operators*, *IEEE Transactions on Magnetics*, vol. 38, no. 2, pp. 569–572, 2002, ISSN: 0018-9464. DOI: 10.1109/20.996149.

[42] P. Clément, *Approximation by finite element functions using local regularization*, *RAIRO Anal. Numer.*, vol. 9, pp. 77–84, 1975.

[43] J. Corno, *Numerical methods for the estimation of the impact of geometric uncertainties on the performance of electromagnetic devices*, Dissertation, Technische Universität Darmstadt, Darmstadt, 2017. urn: urn:nbn:de:tuda-tuprints-70389.

[44] I. Cortes Garcia, *Mathematical analysis and simulation of field models in accelerator circuits*, Springer Theses: Recognizing Outstanding Ph.D. Research, Dissertation, Technische Universität Darmstadt, Darmstadt, 2020, ISBN: 978-3-030-63272-4. DOI: 10.1007/978-3-030-63273-1.

[45] J. A. Cottrell, T. J. R. Hughes, and Y. Bazilevs, *Isogeometric Analysis: Toward Integration of CAD and FEA*. Wiley, 2009, ISBN: 978-0470749098.

[46] B. Davat, Z. Ren, and M. Lajoie-Mazenc, *The movement in field modeling*, *IEEE Transactions on Magnetics*, vol. 21, no. 6, pp. 2296–2298, 1985, ISSN: 0018-9464.

[47] C. De Boor, *Splines as linear combinations of b-splines. a survey.*, Wisconsin Univ Madison Mathematics Research Center, Tech. Rep., 1976.

[48] H. De Gersem, J. Gyselinck, P. Dular, K. Hameyer, and T. Weiland, *Comparison of sliding-surface and moving-band techniques in frequency-domain finite-element models of rotating machines*, *COMPEL: The International Journal for Computation and Mathematics in Electrical and Electronic Engineering*, vol. 23, no. 4, pp. 1006–1014, 2004, ISSN: 0332-1649. DOI: 10.1108/03321640410553436.

[49] H. De Gersem, I. Munteanu, and T. Weiland, *Construction of differential material matrices for the orthogonal finite-integration technique with nonlinear materials*, *IEEE Transactions on Magnetics*, vol. 44, no. 6, pp. 710–713, 2008, ISSN: 0018-9464. DOI: 10.1109/TMAG.2007.915819.

[50] H. De Gersem and T. Weiland, *Harmonic weighting functions at the sliding interface of a finite-element machine model incorporating angular displacement*, *IEEE Transactions on Magnetics*, vol. 40, no. 2, pp. 545–548, 2004, ISSN: 0018-9464. DOI: 10.1109/TMAG.2004.824616.

[51] M. De Martin, F. Luise, S. Pieri, A. Tessarolo, and C. Poloni, *Numerical multi-objective optimization of a squirrel cage induction motor for industrial application*, in *2015 Intl Aegean Conference on Electrical Machines Power Electronics (ACEMP), 2015 Intl Conference on Optimization of Electrical Electronic Equipment (OPTIM) 2015 Intl Symposium on Advanced Electromechanical Motion Systems (ELECTROMOTION)*, 2015, pp. 170–175.

[52] M. Delfour and J.-P. Zolésio, *Shapes and Geometries: Metrics, Analysis, Differential Calculus, and Optimization* (Advances in Design and Control), 2nd ed. Philadelphia, PA, USA: SIAM, 2011. DOI: 10.1137/1.9780898719826.

[53] P. Di Barba, *Multiobjective Shape Design in Electricity and Magnetism* (Lecture Notes in Electrical Engineering). Springer, 2010.

[54] P. Dłotko, B. Kapidani, S. Pitassi, and R. Specogna, *Fake conductivity or cohomology: Which to use when solving eddy current problems with h-formulations?*, *IEEE Transactions on Magnetics*, vol. 55, no. 6, pp. 1–4, 2019, ISSN: 0018-9464. DOI: 10.1109/TMAG.2019.2906099.

[55] P. Dlotko, B. Kapidani, and R. Specogna, *Topoprocessor: An efficient computational topology toolbox for h-oriented eddy current formulations*, *IEEE Transactions on Magnetics*, vol. 53, no. 6, pp. 1–4, 2017, ISSN: 0018-9464. DOI: 10.1109/tmag.2017.2661480.

[56] P. Dłotko and R. Specogna, *Cohomology in 3d magneto-quasistatics modeling*, *Communications in Computational Physics*, vol. 14, no. 1, pp. 48–76, 2013. DOI: 10.4208/cicp.151111.180712a.

[57] P. Dłotko and R. Specogna, *Physics inspired algorithms for (co)homology computations of three-dimensional combinatorial manifolds with boundary*, *Computer Physics Communications*, vol. 184, no. 10, pp. 2257–2266, 2013, ISSN: 0010-4655. DOI: https://doi.org/10.1016/j.cpc.2013.05.006.

[58] J. Dölz, H. Harbrecht, S. Kurz, S. Schöps, and F. Wolf, *A fast isogeometric BEM for the three dimensional Laplace- and Helmholtz problems*, *Computer Methods in Applied Mechanics and Engineering*, vol. 330, pp. 83–101, 2018, ISSN: 0045-7825. DOI: 10.1016/j.cma.2017.10.020. arXiv: 1708.09162.

[59] X. Duan and Z. Yao, *Harmonic field in knotted space*, *Physical Review E*, vol. 97, p. 040 702, 4 2018, ISSN: 2470-0045. DOI: 10.1103/PhysRevE.97.040702.

[60] Y. Duan and D. M. Ionel, *A review of recent developments in electrical machine design optimization methods with a permanent-magnet synchronous motor benchmark study*, *IEEE Transactions on Industry Applications*, vol. 49, no. 3, pp. 1268–1275, 2013, ISSN: 0093-9994. DOI: 10.1109/TIA.2013.2252597.

[61] P. Dular, A. Nicolet, A. Genon, and W. Legros, *A discrete sequence associated with mixed finite elements and its gauge condition for vector potentials*, *IEEE Transactions on Magnetics*, vol. 31, no. 3, pp. 1356–1359, 1995, ISSN: 0018-9464. DOI: 10.1109/20.376278.

[62] J. W. Eaton, D. Bateman, S. Hauberg, and R. Wehbring, *GNU Octave 4.2 Reference Manual*. Samurai Media Limited, 2017, ISBN: 978-9888407071.

[63] H. Egger, M. Harutyunyan, R. Löscher, M. Merkel, and S. Schöps, *On torque computation in electric machine simulation by harmonic mortar methods*, *Journal of Mathematics in Industry*, vol. 12, no. 6, 2022, ISSN: 2190-5983. DOI: 10.1186/s13362-022-00121-2. arXiv: 2112.05572.

[64] H. Egger, M. Harutyunyan, M. Merkel, and S. Schöps, *On the stability of harmonic mortar methods with application to electric machines*, in *Scientific Computing in Electrical Engineering SCEE 2020*, M. van Beurden, N. Budko, and W. Schilders, Eds., ser. Mathematics in Industry, Berlin: Springer, 2021, ISBN: 978-3-030-81454-0. arXiv: 2005.12020.

[65] G. Elber, *IRIT ver. 12 user's manual*, www.cs.technion.ac.il/~irit, Technion, Israel Institute of Technology, Haifa, 2021.

[66] A. Embar, J. Dolbow, and I. Harari, *Imposing Dirichlet boundary conditions with Nitsche's method and spline-based finite elements*, *International Journal for Numerical Methods in Engineering*, vol. 83, no. 7, pp. 877–898, 2010, ISSN: 0029-5981. DOI: 10.1002/nme.2863.

[67] C. R. I. Emson and C. W. Trowbridge, *Transient 3d eddy currents using modified magnetic vector potentials and magnetic scalar potentials*, *IEEE Transactions on Magnetics*, vol. 24, no. 1, pp. 86–89, 1988, ISSN: 0018-9464. DOI: 10.1109/20.43862.

[68] L. A. J. Friedrich, *Isogeometric analysis of nonlinear eddy current problems*, Dissertation, Technische Universiteit Eindhoven, 2020. DOI: 10.6100/5074ed73-fcec-4a93-8a5c-699abcf6e896.

[69] D. Fußeder, B. Simeon, and A.-V. Vuong, *Fundamental aspects of shape optimization in the context of isogeometric analysis*, *Computer Methods in Applied Mechanics and Engineering*, vol. 286, pp. 313–331, 2015, ISSN: 0045-7825. DOI: 10.1016/j.cma.2014.12.028.

[70] P. Gangl, S. Köthe, C. Mellak, A. Cesarano, and A. Mütze, *Multi-objective free-form shape optimization of a synchronous reluctance machine*, 6, 2020, pp. 1849–1864. DOI: 10.1108/COMPEL-02-2021-0063.

[71] P. Gangl, U. Langer, A. Laurain, H. Meftahi, and K. Sturm, *Shape optimization of an electric motor subject to nonlinear magnetostatics*, *SIAM Journal on Scientific Computing*, vol. 37, no. 6, B1002–B1025, 2015, ISSN: 1064-8275. DOI: 10.1137/15100477x.

[72] P. Gangl, U. Langer, A. Mantzaflaris, and R. Schneckenleitner, *Isogeometric simulation and shape optimization with applications to electrical machines*, in *Scientific Computing in Electrical Engineering SCEE 2018*, V. R. Giuseppe Nicosia, Ed., ser. Mathematics in Industry, vol. 32, Berlin: Springer, 2020, pp. 35–44, ISBN: 978-3-030-44100-5. DOI: 10.1007/978-3-030-44101-2. arXiv: 1809.03377.

[73] P. Gangl, U. Langer, A. Mantzaflaris, and R. Schneckenleitner, *Isogeometric simulation and shape optimization with applications to electrical machines*, in *Scientific Computing in Electrical Engineering (SCEE 2018)*, G. Nicosia and V. Romano, Eds., vol. 32, Springer International Publishing, 2020, pp. 35–44. DOI: 10.1007/978-3-030-44101-2.

[74] P. Gangl, K. Sturm, M. Neunteufel, and J. Schöberl, *Fully and semi-automated shape differentiation in NGSolve*, *Structural and Multidisciplinary Optimization*, vol. 63, no. 3, pp. 1579–1607, 2020, ISSN: 1615-1488. DOI: 10.1007/s00158-020-02742-w. arXiv: 2004.06783.

[75] C. Geuzaine and J.-F. Remacle, *Gmsh: A 3-D finite element mesh generator with built-in pre- and post-processing facilities*, *International Journal for Numerical Methods in Engineering*, vol. 79, pp. 1309–1331, 2009, ISSN: 0029-5981. DOI: 10.1002/nme.2579.

[76] J. F. Gieras, *Advancements in Electric Machines*. Springer, 2008.

[77] M. van der Giet, *Analysis of electromagnetic acoustic noise excitations: A contribution to low-noise design and to the auralization of electrical machines*, Dissertation, RWTH Aachen, Aachen, Germany, 2011, ISBN: 978-3-8322-9973-6.

[78] D. F. Griffiths, *Introduction to Electrodynamics*, 4th ed. Glenview, IL, USA: Pearson, 2013, ISBN: 978-0-321-85656-2.

[79] J. Gyselinck, L. Vandevelde, P. Dular, C. Geuzaine, and W. Legros, *A general method for the frequency domain FE modeling of rotating electromagnetic devices*, *IEEE Transactions on Magnetics*, vol. 39, no. 3, pp. 1147–1150, 2003, ISSN: 0018-9464. DOI: 10.1109/TMAG.2003.810381.

[80] K. Hameyer and M. Kasper, *Shape optimization of a fractional horse-power DC-motor by stochastic methods*, in *Computer Aided Optimimum Design of Structures III: Optimization of Structural Systems and Applications*, S. Hernandez and C. Brebbia, Eds., 1993, pp. 15–30.

[81] J. Haslinger and R. A. E. Mäkinen, *Introduction to Shape Optimization: Theory, Approximation, and Computation* (Advances in Design and Control). Society for Industrial and Applied Mathematics, 2003, ISBN: 978-0898715361.

[82] O. Heaviside, *On the forces, stresses, and fluxes of energy in the electromagnetic field*, *Royal Society of London Proceedings Series I*, vol. 50, pp. 126–129, 1891.

[83] F. Henrotte and K. Hameyer, *Computation of electromagnetic force densities: Maxwell stress tensor vs. virtual work principle*, *J. Comput. Appl. Math.*, vol. 168, pp. 235–243, 2004.

[84] F. Henrotte, G. Deliége, and K. Hameyer, *The eggshell approach for the computation of electromagnetic forces in 2D and 3D*, *COMPEL: The International Journal for Computation and Mathematics in Electrical and Electronic Engineering*, vol. 23, no. 4, pp. 996–1005, 2004, ISSN: 0332-1649. DOI: 10.1108/03321640410553427.

[85] F. Henrotte, M. Felden, M. van der Giet, and K. Hameyer, *Electromagnetic force computation with the eggshell method*, in *14th International IGTE Symposium on Numerical Field Calculation in Electrical Engineering*, Graz, 2010.

[86] S. L. Ho, S. Yang, L. E. W. C. Ni Guangzheng, and H. C. Wong, *A particle swarm optimization-based method for multiobjective design optimizations*, *IEEE Transactions on Magnetics*, vol. 41, no. 5, pp. 1756–1759, 2005, ISSN: 0018-9464. DOI: 10.1109/TMAG.2005.846033.

[87] M. Huber, M. Fuhrländer, and S. Schöps, *Multi-objective yield optimization for electrical machines using Gaussian processes to learn faulty designs*, *IEEE Transactions on Industry Applications*, vol. 59, no. 2, pp. 1340–1350, 2022, ISSN: 0093-9994. DOI: 10.1109/TIA.2022.3211250. arXiv: 2204.04986.

[88] T. J. R. Hughes, J. A. Cottrell, and Y. Bazilevs, *Isogeometric analysis: CAD, finite elements, NURBS, exact geometry and mesh refinement*, *Computer Methods in Applied Mechanics and Engineering*, vol. 194, pp. 4135–4195, 2005, ISSN: 0045-7825. DOI: 10.1016/j.cma.2004.10.008.

[89] H. Igarashi, *On the property of the curl-curl matrix in finite element analysis with edge elements*, *IEEE Transactions on Magnetics*, vol. 37, no. 5, pp. 3129–3132, 2001, ISSN: 0018-9464. DOI: 10.1109/20.952559.

[90] International Energy Agency, *World Energy Outlook 2012*. Paris: OECD Publishing, 2022. DOI: 10.1787/20725302.

[91] J. D. Jackson, *Classical Electrodynamics*, 3rd. New York, NY, USA: Wiley & Sons, 1998, ISBN: 978-0-471-30932-1. DOI: 10.1017/CBO9780511760396.

[92] P. Jorkowski and R. Schuhmann, *Mode tracking for parametrized eigenvalue problems in computational electromagnetics*, in *2018 International Applied Computational Electromagnetics Society (ACES) Symposium*, B. M. Notaros, Ed., Denver, Colorado: IEEE, 2018, p. 17 803 096, ISBN: 978-0-9960078-7-0. DOI: 10.23919/ROPACES.2018.8364147.

[93] B. Kapidani, *Topoprocessor*, https://github.com/bkapidani/topoprocessor, 2021.

[94] B. Kapidani, M. Merkel, S. Schöps, and R. Vázquez, *Arbitrary order spline approximation of time harmonic eddy current problems and cohomology computation in the case of non simply connected conductors*, *Advances in Computational Mathematics*, in preparation.

[95] B. Kapidani, M. Merkel, S. Schöps, and R. Vázquez, *Tree-cotree decomposition of isogeometric mortared spaces in h(curl) on multi-patch domains*, *Computer Methods in Applied Mechanics and Engineering*, vol. 395, p. 114 949, 2022, ISSN: 0045-7825. DOI: 10.1016/j.cma.2022.114949. arXiv: 2110.15860.

[96] J. Al-Khalili, *The birth of the electric machines: A commentary on Faraday (1832) 'experimental researches in electricity'*, *Philosophical Transactions of the Royal Society A: Mathematical, Physical and Engineering Sciences A*, vol. 373, no. 2039, p. 20 140 208, 2015. DOI: 10.1098/rsta.2014.0208.

[97] F. Kikuchi, *Mixed and penalty formulations for finite element analysis of an eigenvalue problem in electromagnetism*, *Computer Methods in Applied Mechanics and Engineering*, vol. 64, pp. 509–521, 1987, ISSN: 0045-7825.

[98] I. Kulchytska-Ruchka, *Acceleration of FEM computations for induction machines*, Master's Thesis, Universität Hamburg, Hamburg, 2017.

[99] E. Lange, *Numerische Werkzeuge zur Simulation von nichtsinusförmig gespeisten geregelten elektrischen Maschinen im dynamischen Betrieb*, Dissertation, RWTH Aachen, Aachen, 2012.

[100] U. Langer and S. E. Moore, *Discontinuous Galerkin isogeometric analysis of elliptic PDEs on surfaces*, in *Domain Decomposition Methods in Science and Engineering XXIII*, C.-O. Lee, X.-C. Cai, D. E. Keyes, H. H. Kim, A. Klawonn, E.-J. Park, and O. B. Widlund, Eds., ser. Lecture Notes in Computational Science and Engineering, 2017, pp. 319–326. DOI: 10.1007/978-3-319-18827-0_31.

[101] W. Leal Filho, R. Kotter, P. G. Özuyar, I. R. Abubakar, J. H. P. P. Eustachio, and N. R. Matandirotya, *Understanding rare earth elements as critical raw materials*, *Sustainability*, vol. 15, no. 3, p. 1919, 2023.

[102] G. Lei, G. Bramerdorfer, C. Liu, Y. Guo, and J. Zhu, *Robust design optimization of electrical machines: A comparative study and space reduction strategy*, *IEEE Transactions on Energy Conversion*, vol. 36, no. 1, pp. 300–313, 2021, ISSN: 0885-8969. DOI: 10.1109/TEC.2020.2999482.

[103] C. L. Lok, B. Vengadaesvaran, and S. Ramesh, *Implementation of hybrid pattern search–genetic algorithm into optimizing axial-flux permanent magnet coreless generator (AFPMG)*, *Electrical Engineering (Archiv für Elektrotechnik)*, vol. 99, pp. 751–761, 2017, ISSN: 1432-0487. DOI: 10.1007/s00202-016-0443-9.

[104] B. Ma, J. Zheng, G. Lei, J. Zhu, P. Jin, and Y. Guo, *Topology optimization of ferromagnetic components in electrical machines*, *IEEE Transactions on Energy Conversion*, vol. 35, no. 2, pp. 786–798, 2020, ISSN: 0885-8969. DOI: 10.1109/tec.2019.2960519.

[105] C. Ma and L. Qu, *Multiobjective optimization of switched reluctance motors based on design of experiments and particle swarm optimization*, *IEEE Transactions on Energy Conversion*, vol. 30, no. 3, pp. 1144–1153, 2015, ISSN: 0885-8969.

[106] J. B. Manges and Z. J. Cendes, *A generalized tree-cotree gauge for magnetic field computation*, *IEEE Transactions on Magnetics*, vol. 31, no. 3, pp. 1342–1347, 1995, ISSN: 0018-9464. DOI: 10.1109/20.376275.

[107] W. S. Massey. New York, NY: Springer New York, 1991, pp. 305–322, ISBN: 978-1-4939-9063-4. DOI: 10.1007/978-1-4939-9063-4_12.

[108] Mathworks, *MATLAB getting started guide*, 9.8.0 (R2020a), 2020.

[109] J. C. Maxwell, *A dynamical theory of the electromagnetic field*, *Royal Society Transactions*, vol. 155, pp. 459–512, 1864.

[110] J. C. Maxwell, *A treatise on electricity and magnetism*. Oxford: Clarendon Press, 1873.

[111] J. C. Maxwell, *On physical lines of force*, *Philosophical Magazine and Journal of Science*, 1861.

[112] I. Mayergoyz, *Eddy current hysteresis and the Preisach model*, *IEEE Transactions on Magnetics*, vol. 34, no. 4, pp. 1261–1263, 1998. DOI: 10.1109/20.706515.

[113] M. Merkel, P. Gangl, and S. Schöps, *Results of the shape optimization of rotating electric machines using isogeometric analysis*, 2020. DOI: 10.5281/zenodo.3688478.

[114] M. Merkel, P. Gangl, and S. Schöps, *Shape optimization of rotating electric machines using isogeometric analysis*, *IEEE Transactions on Energy Conversion*, vol. 36, no. 4, 2021, ISSN: 0885-8969. DOI: 10.1109/TEC.2021.3061271. arXiv: 1908.06009.

[115] M. Merkel, A. Gschwentner, K. Roppert, and S. Schöps, *Non-conforming isogeometric Nitsche formulation for the simulation of electric motors*, in preparation.

[116] M. Merkel, B. Kapidani, S. Schöps, and R. Vázquez, *Torque computation with the isogeometric mortar method for the simulation of electric machines*, *IEEE Transactions on Magnetics*, vol. 58, no. 9, 2022, ISSN: 0018-9464. DOI: 10.1109/TMAG.2022.3186247. arXiv: 2202.05771.

[117] P. Monk, *Finite Element Methods for Maxwell's Equations*. Oxford: Oxford University Press, 2003.

[118] J. Munkres, *Elements Of Algebraic Topology*. Boca Raton: CRC Press, 1984. DOI: 10.1201/9780429493911.

[119] I. Munteanu, *Tree-cotree condensation properties*, *International Compumag Society Newsletter*, vol. 9, pp. 10–14, 2002, ISSN: 1026-0854.

[120] E. Neuman, *Moments and Fourier transforms of b-splines*, *Journal of Computational and Applied Mathematics*, vol. 7, no. 1, pp. 51–62, 1981, ISSN: 0377-0427. DOI: 10.1016/0771-050x(81)90008-5.

[121] J. Nitsche, *Über ein Variationsprinzip zur Lösung von Dirichlet-Problemen bei Verwendung von Teilräumen, die keinen Randbedingungen unterworfen sind*, *Abhandlungen aus dem Mathematischen Seminar der Universität Hamburg*, vol. 36, pp. 9–15, 1971. DOI: 10.1007/BF02995904.

[122] J. Nocedal and S. J. Wright, *Numerical optimization* (Springer Series in Operations Research and Financial Engineering), 2nd ed. New York: Springer, 2006, ISBN: 978-0-387-40065-5.

[123] U. Pahner, *A general design tool for the numerical optimisation of electromagnetic energy transducers*, PhD Thesis, KU Leuven, Leuven, 1998.

[124] V. Parekh, D. Flore, and S. Schöps, *Deep learning-based prediction of key performance indicators for electrical machine*, *IEEE Access*, vol. 9, 2021, ISSN: 2169-3536. DOI: 10.1109/ACCESS.2021.3053856. arXiv: 2012.11299.

[125] V. Parekh, D. Flore, and S. Schöps, *Variational autoencoder based metamodeling for multi-objective topology optimization of electrical machines*, *IEEE Transactions on Magnetics*, vol. 58, no. 9, 2022, ISSN: 0018-9464. DOI: 10.1109/TMAG.2022.3163972. arXiv: 2201.08877.

[126] L. Piegl and W. Tiller, *The NURBS Book*, 2nd ed. Springer, 1997, ISBN: 3540615458.

[127] R. Plato, *Numerische Mathematik kompakt*. Vieweg, 2006, ISBN: 978-3-8348-0277-4.

[128] G. Plonka, D. Potts, G. Steidl, and M. Tasche, *Numerical Fourier analysis* (Applied and Numerical Harmonic Analysis), J. J. Benedetto, Ed. Birkhäuser, 2018. DOI: 10.1007/978-3-030-04306-3.

[129] X. Qian, *Full analytical sensitivities in NURBS based isogeometric shape optimization*, *Computer Methods in Applied Mechanics and Engineering*, vol. 199, no. 29-32, pp. 2059–2071, 2010, ISSN: 0045-7825. DOI: 10.1016/j.cma.2010.03.005.

[130] A. Quarteroni and A. Valli, *Domain Decomposition Methods for Partial Differential Equations* (Numerical Mathematics and Scientific Computation). Oxford: Oxford University Press, 1999.

[131] V. Raisanen, S. Suuriniemi, S. Kurz, and L. Kettunen, *Subdomain reduction by Dirichlet-to-Neumann mappings in time-domain electrical machine modeling*, *IEEE Transactions on Energy Conversion*, vol. 30, no. 1, pp. 340–348, 2015, ISSN: 0885-8969. DOI: 10.1109/tec.2014.2333877.

[132] J. C. Rautio, *The long road to Maxwell's equations*, *IEEE Spectrum*, vol. 51, no. 12, pp. 36–56, 2014, ISSN: 0018-9235. DOI: 10.1109/MSPEC.2014.6964925.

[133] P. A. Raviart and J. M. Thomas, *Primal hybrid finite element methods of 2nd order elliptic equations*, *Math. Comp.*, vol. 31, pp. 391–413, 1977.

[134] D. Rodger, H. C. Lai, and P. J. Leonard, *Coupled elements for problems involving movement*, *IEEE Transactions on Magnetics*, vol. 26, no. 2, pp. 548–550, 1990, ISSN: 0018-9464.

[135] A. A. Rodriguez and F. Rapetti, *Small trees for high order whitney elements*, in *Spectral and High Order Methods for Partial Differential Equations ICOSAHOM 2018*, S. J. Sherwin, D. Moxey, J. Peiró, P. E. Vincent, and C. Schwab, Eds., ser. Lecture Notes in Computational Science and Engineering, Springer International Publishing, 2020, pp. 587–597, ISBN: 978-3-030-39647-3. DOI: 10.1007/978-3-030-39647-3.

[136] K. Roppert, S. Schoder, F. Toth, and M. Kaltenbacher, *Non-conforming Nitsche interfaces for edge elements in curl–curl-type problems*, *IEEE Transactions on Magnetics*, vol. 56, no. 5, pp. 1–7, 2020, ISSN: 0018-9464. DOI: 10.1109/TMAG.2020.2980477.

[137] M. Rosu, P. Zhou, D. Lin, D. M. Ionel, M. Popescu, F. Blaabjerg, V. Rallabandi, and D. Staton, *Multiphysics Simulation by Design for Electrical Machines, Power Electronics and Drives*. Wiley-IEEE Press, 2017, ISBN: 978-1-119-10344-8.

[138] S. Russenschuck, *Field Computation for Accelerator Magnets: Analytical and Numerical Methods for Electromagnetic Design and Optimization*. Berlin: Wiley-VCH, 2010.

[139] S. Russenschuck, *Mathematical optimization techniques for the design of permanent magnet synchronous machines based on numerical field calculation*, *IEEE Transactions on Magnetics*, vol. 26, no. 2, pp. 638–641, 1990, ISSN: 0018-9464.

[140] Y. Saad, *Schur complement preconditioners for distributed general sparse linear systems*, in *Domain Decomposition Methods in Science and Engineering XVI*, O. B. Widlund and D. Keyes, Eds., Berlin: Springer, 2006, pp. 127–138, ISBN: 978-3-540-34468-1. DOI: 10.1007/978-3-540-34469-8_11.

[141] S. J. Salon, *Finite Element Analysis of Electrical Machines*. Kluwer, 1995.

[142] F. L. M. dos Santos, J. Anthonis, F. Naclerio, J. Gyselinck, H. Van der Auweraer, and L. C. S. Goes, *Multiphysics NVH modeling: Simulation of a switched reluctance motor for an electric vehicle*, *IEEE Transactions on Industrial Electronics*, vol. 61, no. 1, pp. 469–476, 2014, ISSN: 0278-0046. DOI: 10.1109/tie.2013.2247012.

[143] W. H. A. Schilders, *Introduction to model order reduction*, in *Model Order Reduction: Theory, Research Aspects and Applications*, ser. Mathematics in Industry, W. H. A. Schilders, H. A. van der Vorst, and J. Rommes, Eds., vol. 13, Springer, Berlin, Heidelberg, 2008, pp. 3–32. DOI: 10.1007/978-3-540-78841-6.

[144] J. Schöberl, *Numerical methods for Maxwell equations*, Institute for Analysis and Scientific Computing at Vienna University of Technology, Wien, lecturenotes, 2009.

[145] J. Schöberl and S. Zaglmayr, *High order nédélec elements with local complete sequence properties*, *COMPEL: The International Journal for Computation and Mathematics in Electrical and Electronic Engineering*, vol. 24, no. 2, pp. 374–384, 2005, ISSN: 0332-1649. DOI: 10.1108/03321640510586015.

[146] S. Schöps, H. De Gersem, and T. Weiland, *Winding functions in transient magnetoquasistatic field-circuit coupled simulations*, *COMPEL: The International Journal for Computation and Mathematics in Electrical and Electronic Engineering*, vol. 32, no. 6, pp. 2063–2083, 2022, ISSN: 0332-1649. DOI: 10.1108/COMPEL-01-2013-0004.

[147] V. Schulz and M. Siebenborn, *Computational comparison of surface metrics for pde constrained shape optimization*, *Computational Methods in Applied Mathematics*, vol. 16, no. 3, pp. 485–496, 01 Jul. 2016. DOI: https://doi.org/10.1515/cmam-2016-0009.

[148] L. R. Scott and S. Zhang, *Finite element interpolation of nonsmooth functions satisfying boundary conditions*, *Math. Comp.*, vol. 54, pp. 483–493, 1990.

[149] G. Y. Sizov, P. Zhang, D. M. Ionel, N. A. O. Demerdash, and M. Rosu, *Automated multi-objective design optimization of PM AC machines using computationally efficient FEA and differential evolution*, *IEEE Transactions on Industry Applications*, vol. 49, no. 5, pp. 2086–2096, 2013, ISSN: 0093-9994.

[150] D. Sun, J. Manges, X. Yuan, and Z. Cendes, *Spurious modes in finite-element methods*, *IEEE Antennas and Propagation Magazine*, vol. 37, no. 5, pp. 12–24, 1995. DOI: 10.1109/74.475860.

[151] N. Takorabet, B. Laporte, and G. Vinsard, *On the optimization of linear induction devices*, *Electrical Engineering (Archiv für Elektrotechnik)*, vol. 80, pp. 221–226, 1997, ISSN: 1432-0487.

[152] U.S. DRIVE, *Electrical and electronics technical team roadmap*, U.S. Department of Energy, Technical Report, 2017.

[153] U.S. Energy Information Administration, *May 2023*, U.S. Department of Energy, Washington, Monthly Energy Review, 2023.

[154] D. Vanoost, H. De Gersem, J. Peuteman, G. Gielen, and D. Pissoort, *Two-dimensional magnetostatic finite-element simulation for devices with a radial symmetry*, *IEEE Transactions on Magnetics*, vol. 50, no. 5, p. 7 400 204, 2014, ISSN: 0018-9464.

[155] R. Vázquez, *A new design for the implementation of isogeometric analysis in Octave and Matlab: GeoPDEs 3.0*, *Computers and Mathematics with Applications*, vol. 72, no. 3, pp. 523–554, 2016, ISSN: 0898-1221. DOI: 10.1016/j.camwa.2016.05.010.

[156] B. D. S. G. Vidanalage, M. S. Toulabi, and S. Filizadeh, *Multimodal design optimization of V-shaped magnet IPM synchronous machines*, *IEEE Transactions on Energy Conversion*, vol. 33, no. 3, pp. 1547–1556, 2018.

[157] G. J. Wallinger, *A method to couple non-conforming finite element meshes*, Dissertation, Technische Universität Graz, Graz, 2019.

[158] J. P. Webb and B. Forghani, *The low-frequency performance of $H-\phi$ and $T-\Omega$ methods using edge elements for 3d eddy current problems*, *IEEE Transactions on Magnetics*, vol. 29, no. 6, pp. 2461–2463, 1993, ISSN: 0018-9464. DOI: 10.1109/20.280983.

[159] K. Weeber and S. R. H. Hoole, *Geometric parametrization and constrained optimization techniques in the design of salient pole synchronous machines*, *IEEE Transactions on Magnetics*, vol. 28, no. 4, pp. 1948–1960, 1992, ISSN: 0018-9464.

[160] O. Weeger, S.-K. Yeung, and M. L. Dunn, *Isogeometric design and optimization of spatially varying, multi-material 3d printed rod structures*, in *Proceedings of the 3rd International Conference on Progress in Additive Manufacturing*, ser. Lect. Notes Comput. Sci. Eng. Nanyang Technological University, 2018, pp. 280–285. DOI: 10.25341/D4JG6V.

[161] D. Weidert, *Volumetric modelling and simulation of electric machines for additive manufacturing*, Bachelor's Thesis, Technische Universität Darmstadt, Darmstadt, 2021.

[162] M. Wiesheu, M. Merkel, T. Sittig, D. Benke, M. Fries, S. Schöps, O. Weeger, and I. Cortes Garcia, *How to build the optimal magnet assembly for magnetocaloric cooling: Structural optimization with isogeometric analysis*, *International Journal of Refrigeration*, 2023, ISSN: 0140-7007. DOI: 10.1016/j.ijrefrig.2023.04.014. arXiv: 2212.06580, accepted.

[163] T. Wildi, *Electrical machines, drives, and power systems*, 5th ed. Pearson Educacion, 2006.

[164] B. I. Wohlmuth, *A mortar finite element method using dual spaces for the Lagrange multiplier*, *SIAM Journal on Numerical Analysis*, vol. 38, no. 3, pp. 989–1012, 2000.

[165] S. Zaglmayr, *High order finite element methods for electromagnetic field computation*, Dissertation, Johannes Kepler Universität, Linz, Austria, 2006.

[166] A. Ziegler, M. Merkel, P. Gangl, and S. Schöps, *On the computation of analytic sensitivities of eigenpairs in isogeometric analysis*, *Computer Methods in Applied Mechanics and Engineering*, vol. 409, p. 115 961, 2023, ISSN: 0045-7825. DOI: 10.1016/j.cma.2023.115961. arXiv: 2212.10347.

Acknowledgments

Throughout the journey of completing this thesis, I had the privilege of being accompanied, supported and guided by many people who contributed to this work in various ways.

First of all, I would like to thank my supervisor Sebastian Schöps, for offering the opportunity to work on this thesis, for his unwavering support, patience, excellent mentorship and guidance throughout my time in Darmstadt and his encouragement which motivated me to go into the field of electrical engineering. I am also thankful for many scientific conversations and the friendly, open and welcoming work environment he created.

I am extremely grateful to to Bernard Kapidani, Rafael Vázquez, and Peter Gangl for their collaboration on various publications, enriching discussions, many enjoyable (virtual) meetings and their support during various phases in my research.

I am also thankful to my present and former colleagues at TEMF and GSC who have made my time there memorable and enjoyable: during work, conferences, lunch breaks, tea meetings, kicker breaks, cake and waffle meetings, GSC events, game nights, at our retreats and when hiking at Kleinwalsertal. I would especially like to thank Idoia Cortes Garcia for many scientific and non-scientific discussions, for her advice, fun at conferences and her friendship; Niklas Georg for being a great office mate, kicker partner and for being my GSC-mentor; Mona Fuhrländer for her support particularly during my writing phase and Anna Ziegler, Mané Harutyunyan, Mario Mally and Michael Wiesheu for their fruitful collarborations.

Furthermore, I want to express my gratitude to Herbert De Gersem, Jörg Ostrowski, Oliver Weeger, Herbert Egger, Innocent Niyonzima, Andreas Gschwentner, Klaus Roppert and Richard Löscher for their collaboration, discussions and support.

I extend my gratitude to Devin Balian, Denis Andric, and David Weidert (as well as Mario and Michael of course) for their contribution to this work through their theses.

My thanks also go to Carina Schuster, Heike Koch, and Achim Wagner for their consistent organizational support and to Christian Schmitt for his excellent IT assistance.

Finally, I am deeply thankful to Alex and my family for their their continuous support and encouragement.

This work is supported by the Graduate School and Centre for Computational Engineering at TU Darmstadt and the German Research Foundation (SCHO 1562/6-1, SFB TRR-361). For spell checking, grammar correction and translation purposes, Grammarly, ChatGPT and DeepL Translator were employed.